Chemical synthesis and electrical characterization of nickel oxide thin films for sensor applications

by

Tunde Shadrach Akinkuade

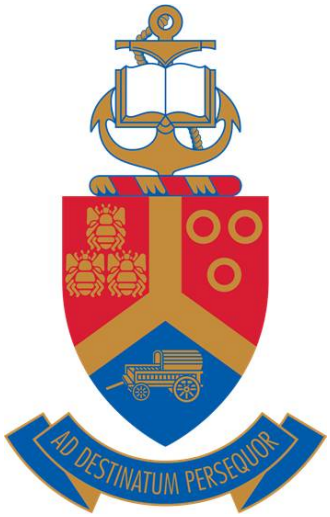

Submitted in partial fulfilment of the requirements for the degree of

DOCTOR OF PHILOSOPHY (PhD) IN PHYSICS

In the Faculty of Natural and Agricultural Sciences

University of Pretoria

PRETORIA

November 2019

Supervisor: Prof. Jacqueline M. Nel

Co-supervisor: Prof. Walter E. Meyer

Chemical synthesis and electrical characterization of nickel oxide thin films for sensor applications

By

Tunde Shadrach Akinkuade

Supervisor: Prof. Jacqueline M. Nel
Co-supervisor: Prof. Walter E. Meyer

Submitted in partial fulfilment of the requirements for the degree of **DOCTOR OF PHILOSOPHY (PhD) IN PHYSICS** in the faculty of Natural and Agricultural Sciences, University of Pretoria.

The semiconducting properties and wide bandgaps of some metal oxides have made them useful in sensing applications and printed electronics. Doping of common metal oxides to achieve p-type conductivity and the formation of p-n junctions with them is not feasible. However, nickel oxide (NiO) is known for p-type conductivity due to intrinsic defects. This research is aimed at synthesizing NiO thin films by means of chemical solution methods, and to characterize the films to determine the effects of processing methods and conditions of deposition on the properties of the films with the aim to use the films in light or gas sensors. NiO films were synthesized on glass substrates using chemical bath deposition (CBD), sol-gel spin-coating, and spray pyrolysis. Some conditions of deposition such as the concentration of precursors and the processing temperature of the films were varied and the effects of the variations on the properties of the films were studied using X-ray diffraction (XRD), scanning electron microscopy (SEM), scanning probe microscopy (SPM), ultraviolet-visible spectrophotometry, and Raman spectroscopy. Electrical characterization was carried out using a linear four-point probe and current–voltage measurement systems.

The XRD results confirmed that the as-deposited films grown by CBD were hydrated nickel hydroxide. Thermogravimetric analysis (TGA) showed that the transformation of this phase to NiO required annealing at a temperature above 350 ℃. The films were of porous morphology

and were made of nanowalls of varying thickness with an average of 77 nm. This shrank to 52 nm after annealing at 450 ℃.

NiO thin films grown by the sol-gel method were granular, and the crystallinity, grain size and electrical conductivity of the films depended on the temperature at which they were processed. Minimum electrical resistivity of 125 Ω.cm was measured for the film that was dried at 250 ℃ and annealed at 500 ℃.

For the films deposited through spray pyrolysis, the sheet resistance decreased with increasing concentration of precursor and decreased with annealing at 500 ℃ for one hour.

Generally, the films were polycrystalline, with the most prominent peak in their XRD spectrum due to diffraction in the (111) crystallographic plane in the films that were produced by the CBD and spray pyrolysis. However, the (200) peak was most prominent in films that were produced by the sol-gel spin-coating. In all the films, the presence of a Ni–O bond was confirmed by the observation of the Ni–O stretching mode in one-phonon first-order and two-phonon second-order Raman peaks. Spray pyrolysis was found to be the best method for producing transparent and conducting NiO thin films. The current–voltage characteristics of the junction between p-NiO and n-type silicon, showed rectification of two orders of magnitude both in the dark and under illumination. The device was weakly sensitive to solar radiation.

Dedication

To my wife Eniola and my sons Opeyemi, Blessing, and Abiodun for their patience, sacrifice, support and understanding throughout the period of this research.

Declaration

I, Tunde Shadrach Akinkuade declare that this thesis, which I hereby submit for the degree of Doctor of Phiolosophy (PhD) in Physics at the University of Pretoria, is my own work and has not previously been submitted by me for a degree at this or any other tertiary institution.

SIGNATURE: .....

DATE: 2020-04-27

Acknowledgements

This work would not have been accomplished without some supports from certain individuals. For this reason, I would like to express my appreciation to the following people who have contributed in one way or the other toward the success of this PhD study.

• Prof. J.M Nel, my supervisor and Prof. W.E. Meyer the Co-supervisor for their guidance and support throughout the period of carrying out the research and writing this thesis.

• My employer, The Federal Polytechnic, Ado-Ekiti, Nigeria, for allowing me to embark on the research while still working.

• The Tertiary Education Fund, Nigeria, for supporting me financially.

• Prof. M Diale for allowing me to use the solar simulator for the characterization of my samples.

• Messrs Johan Janse van Rensburg and Matshisa Legodi for helping to make pieces of equipment work in the laboratories.

• Members of electronic materials and thin-film research group, such as Ahmed Mustafa Abass, Ahmed Muhammed, and Abdulraoof Ali

• Dr. Madito, Dr. K.O Oyedotun and Dr. M. Mlambo for assisting me with the Raman spectrometric examination of samples.

• Prof. Chris Theron, The Head of Physics Department, University of Pretoria.

• Other members of staff of the Department of Physics, University of Pretoria.

• My wife, E. G. Akinkuade, and my children, Opeyemi Akinkuade, Blessing Akinkuade and Abiodun Akinkuade for their sacrifices, prayers and moral support.

Contents

1 Introduction **1**

1.1 Background and motivation 1

1.2 Aims and objectives 2

1.3 Delineation of the thesis 3

References 4

2 Semiconductor theory **5**

2.1 Introduction 5

2.2 Band structure of materials and electrical conductivity in conductors 5

2.3 Semiconductors 6

2.3.1 Intrinsic and extrinsic semiconductors 7

2.4 Transport mechanism in semiconductors 8

2.4.1 Drift of carriers 8

2.4.2 Resistivity and Hall effect 9

2.4.3 Diffusion 11

2.5 Junctions 12

2.5.1 p-n junction under forward and reverse bias . . . 13

2.5.2 Metal-semiconductor junctions . . . 15

2.5.3 Current transport mechanisms in Schottky diodes . . . 20

2.5.4 Thermionic-emission theory . . . 21

2.5.5 Heterojunctions . . . 22

References . . . 26

3 Literature review of device preparation, nickel oxide (NiO) and device applications 28

3.1 Introduction . . . 28

3.2 Thin-film deposition methods . . . 28

3.2.1 Chemical bath deposition . . . 29

3.2.2 Sol-gel deposition . . . 31

3.2.3 Spin coating . . . 32

3.2.4 Drying and thermal treatment . . . 32

3.2.5 Spray pyrolysis . . . 33

3.3 Nickel (II) oxide . . . 34

3.4 Sensors . . . 36

3.5 Photodetectors . . . 37

3.5.1 Quantum efficiency . . . 37

3.5.2 Responsivity . . . 38

3.5.3 Speed . . . 38

3.5.4 Wavelength sensitivity range . . . 38

3.6 Gas sensors . . . 39

3.6.1 Types of gas sensors . . . 39

3.6.2 Semiconductor metal oxide gas sensors . . . 40

3.6.3 Principle of operation of semiconductor metal oxide gas sensors . . . 40

3.6.4 Sensing mechanism in semiconductor metal oxides . . . 42

3.7 Principle of gas sensing . . . 43

3.7.1 Sensitivity . . . 44

3.7.2 Selectivity . . . 44

3.7.3 Speed of response . . . 44

3.7.4 Stability . . . 45

References . . . 45

4 Experimental and analytical techniques **53**

4.1 Introduction . . . 53

4.2 Experimental techniques . . . 53

4.2.1 Cleaning of substrates . . . 53

4.2.2 Preparation of standard solutions for deposition . . . 54

4.2.3 Growth of thin films using chemical bath deposition . . . 55

4.2.4 Growth of thin films using sol-gel spin coating . . . 56

4.2.5 Growth of thin films using spray pyrolysis method . . . 58

4.2.6 Deposition of NiO thin films on silicon substrate using spray pyrolysis . . 59

4.2.7 Synthesis of lithium-doped NiO thin films using spray pyrolysis 59

4.2.8 Fabrication of a p-NiO/n-ZnO heterojunction 60

4.2.9 Annealing of samples 60

4.2.10 Thermal evaporation of metals for contacts to samples 61

4.3 Analytical techniques 61

4.3.1 Scanning electron microscopy (SEM) 61

4.3.2 Scanning probe microscopy (SPM) 62

4.3.3 X-ray diffraction (XRD) 62

4.3.4 Spectrophotometry 63

4.3.5 Raman spectroscopy 64

4.3.6 Thermogravimetric analysis 65

4.3.7 Electrical characterisation 65

References 70

5 Results: Deposition of NiO thin films using chemical bath deposition 72

5.1 Introduction 72

5.2 Deposition of NiO in a chemical bath using ammonia as the complexing agent . 73

5.3 Deposition of NiO in a chemical bath using monoethanolamine (MEA) as the complexing agent 74

5.4 The effects of annealing temperature on the structural properties of the films . . 80

5.4.1 Summary and conclusions 81

References 82

6 Results: Deposition of NiO thin films using sol-gel spin coating 83

6.1 Introduction 83

6.2 Optimisation of the spin coating process 84

6.3 Effects of thermal treatment on properties of sol - gel fabricated NiO this films . 85

6.4 Fabrication of Al/p-NiO Shottky diodes on p-Si 92

6.5 Summary and conclusions 94

References 96

7 Results: Deposition of NiO thin films using spray pyrolysis 98

7.1 Introduction 98

7.2 Properties of NiO thin films synthesized using a custom-built spray pyrolysis system 98

7.2.1 Structural properties 99

7.2.2 Morphological properties 100

7.2.3 Optical properties 102

7.2.4 Electrical properties 103

7.3 Properties of Li-doped NiO thin films synthesized by spray pyrolysis 104

7.3.1 Structural properties 104

7.3.2 Morphological properties 106

7.3.3 Optical properties 108

7.3.4 Electrical properties . . . 110

7.3.5 Figure of merit . . . 111

7.4 Summary and conclusions . . . 113

References . . . 114

8 Applications of the synthesised NiO films 116

8.1 Introduction . . . 116

8.2 Properties of the p-NiO/n-ZnO heterojunction . . . 116

8.2.1 Structural properties . . . 117

8.2.2 Morphological properties . . . 117

8.2.3 Optical properties . . . 118

8.2.4 Electrical properties . . . 119

8.3 Application of the p-NiO/n-Si heterojunction in light sensing . . . 121

References . . . 124

9 Conclusions and recommendation 125

9.1 Introduction . . . 125

9.1.1 Conclusions . . . 125

9.1.2 Recommendations for future work . . . 127

List of Figures

2.1 Schematic illustration of the Hall effect in a conductor. 9

2.2 Variation in width of the depletion region, junction barrier and Fermi level in (a) unbiased, (b) forward biased, and (c) reversed biased pn junction. Redrawn from [2]. 14

2.3 Band diagram of metal and semiconductor forming a Schottky junction (a) before and (b) after joining. Redrawn from [2]. 16

2.4 Band diagram of metal and semiconductor forming an Ohmic junction (a) before and (b) after joining. Adapted from [2]. 17

2.5 Barrier height lowering due to image force in a Schottky junction. Adapted from [10]. 20

2.6 Transport mechanisms in metal-semiconductor junctions: (1) thermionic emission, (2) tunnelling, (3) recombination in the depletion region, (4) diffusion of electrons in the depletion region, (5) diffusion into the semiconductor. Redrawn from [10]. 21

2.7 Types of band alignment in a heterojunction: (a) straddling, (b) staggered, (c) broken-gap. Redrawn from [10]. 23

2.8 Energy band diagrams for an isolated small bandgap n-type and a wide bandgap p-type semiconductors. Redrawn from [15]. 24

2.9 Energy band diagram of an anisotype heterojunction at thermal equilibrium [15]. 24

3.1 Methods of deposition of thin films [1]. 29

3.2 Stages of spin coating [12]. 32

3.3 Crystal structure of cubic nickel oxide [18]. 34

3.4 Hopping mechanism in a non-stoichiometric NiO. 35

3.5 Structural and band models of a p-type semiconductor metal oxide showing a Schottky barrier between grains. Adapted from [66]. 41

3.6 A typical response of a p-type SMO to an oxidizing gas. Redrawn from [54] . . . 43

4.1 A schematic diagram showing the set-up for chemical bath deposition. 56

4.2 The set-up of the spray-pyrolysis system. 59

4.3 A typical configuration for measuring Hall voltage. 68

4.4 A typical configuration for determination of resistivity of a sample using Hall voltage measurement. 69

4.5 A graph of f versus Q adapted from [14]. 70

5.1 SEM images of NiO thin films deposited for (a) 20 min (b) 40 min (c) 60 min, and (d) 80 min, using ammonia as a complexing agent. 73

5.2 X-ray diffraction (XRD) patterns of the films; as-deposited and annealed at different temperatures. 80

6.1 SEM images of films made from (a) 0.1 M and (b) 0.2 M solutions. 84

6.2 XRD patterns of different number of layers of NiO films fabricated from 0.7 M solution of nickel acetate and annealed at 400 ℃. Recorded with Co Kα X-rays. 85

6.3 (a) XRD pattern of a NiO thin film deposited on glass, (b) FESEM image, (c) SPM image (2 μm $\times$ 2 μm), and (d) cross-sectional image of the film. 92

6.4 (a) I–V characteristics of the Al/NiO junction and (b) V–I plot from the resistivity measurement. 93

6.5 The band structure of Al/NiO junction based on the Anderson model [7]. 94

7.1 XRD pattern of NiO thin films (a) prepared from a 0.05 M solution using a different number of cycles, and (b) prepared from different concentrations at 20 cycles, after annealing at 500 °C. 99

7.2 XRD pattern of (a) as-deposited (As) and annealed (An) films from 0.075 M and 0.1 M solutions and (b) films prepared from 0.05 M solution at 15 and 20 cycles for stationary (S) and moving (M) nozzle modes of spraying. 100

7.3 SEM images of films deposited with the nozzle moving from 20 cycles of (a) 0.05 M (b) 0.075 M and (c) 0.1 M solutions after annealing at 500 °C. 101

7.4 SEM images of films deposited from 10 cycles of (a) 0.075 M (b) 0.1 M, with the nozzle moving, and (c) 20 cycles of 0.05 M solution with stationary nozzle. All films were annealed at 500 °C 101

7.5 Transmittance spectra of NiO films deposited using (a) 0.1 M (b) 0.05 M solutions. 102

7.6 Raman spectra of (a) as-deposited and (b) annealed films. 103

7.7 V–I plot measured by a linear four-point probe measurement. 103

7.8 (a) XRD patterns of the undoped and Li-doped NiO thin films on glass substrates, (b) dependence of the texture coefficient on concentration of Li^+ ions after annealing at 500 °C. 105

7.9 SEM images of (a) 5%, (b) 10%, (c) 15%, and (d) 20% Li-doped films. 107

7.10 3-D SPM images of (a) 5%, (b) 10%, (c) 15%, and (d) 20% Li-doped films. . . . 108

7.11 (a)Transmittance and (b) absorbance spectra of Li-doped NiO thin films. 109

7.12 Raman spectra of Li-doped NiO thin films. 110

7.13 (a) The plots of voltage versus current obtained for the films, and (b) graph showing the dependence of sheet resistance on the concentration of Li. 110

7.14 Relationship between the figure of merit of the films and the concentration of Li ions. 112

8.1 XRD pattern of ZnO thin film deposited on ITO glass and NiO/ZnO heterostructure on ITO. 117

8.2 SEM images of (a) ZnO thin film on ITO, (b) NiO thin film on ZnO. 118

8.3 The transmittance spectrum of the NiO/ZnO heterostructure. 118

8.4 (a) I–V relationship between two Au contacts on the NiO film and (b) dark current–voltage characteristics of the heterojunction 119

8.5 (a) Plot of $dV/d(\ln I)$ and $H(I)$ vs I and (b) dark $1/C^2$–V characteristics of the heterojunction. 119

8.6 Band alignment of p-NiO/n-ZnO (a) before and (b) after the formation of the heterojunction. 120

8.7 XRD pattern of NiO film deposited on silicon substrate. 121

8.8 Dark and light I–V characteristics of p-NiO/n-Si (a) linear scale and (b) semilog scale. 122

8.9 Band alignment of p-NiO/n-Si (a) before and (b) after the formation of a heterojunction. 122

List of Tables

5.1 Calculated inter-planar distance and lattice constant of NiO thin film after annealing at 500 ℃ 81

6.1 Speeds of spin-coater and duration for different concentrations of precursor. . . . 84

6.2 Table showing I_s, n, Φ_B, and r_s of the Al/NiO Schottky diodes on p-silicon. . . 93

7.1 Table showing the d-spacing and lattice constants of the NiO thin films compared to JCPDS 65-2901 100

7.2 Sheet resistance of the films. 104

7.3 d-spacing and lattice constants of the NiO thin films compared with JCPDS 65-2901 105

7.4 Texture coefficients of the films in (111), (200) and (220) planes 106

8.1 Table showing the values of the ideality factor, zero bias barrier height, series resistance and saturation current of the NiO/ZnO heterojunction. 120

Chapter 1

Introduction

1.1 Background and motivation

The conventional semiconductor materials are used mostly in the semiconductor industry for the fabrication of electronic devices such as diodes, transistors and integrated circuits. For instance, compound semiconductors such as III–V compounds are found in optoelectronic applications such as light emitting and laser diodes [1], while the II–IV materials are used in thin film solar cells and infrared detectors [2]. Devices made from these materials are used in various electronic equipment. The processes of synthesising conventional semiconductor materials and fabrication of devices from them are not cheap. Moreover, in order to meet certain demands, some electronic equipment needs to operate under harsh conditions such as high temperature and at high voltage under which most devices made from conventional semiconductors will fail. It is therefore necessary to develop new materials, which are cheap, chemically stable, and can withstand harsh working environment to serve as replacements for the conventional semiconductors in many applications.

Wide bandgap materials have bandgap in excess of 2.2 eV [3], this property makes them suitable for high power and high temperature applications [4]. When used as photodetectors, wide-bandgap materials are usually solar-blind, that is, they do not respond to solar radiation [5]. The materials are replacing conventional semiconductors in some applications. Metal oxides are

cheap to synthesize and are chemically stable, however only few of them posses semiconducting properties.

Oxides of magnesium and aluminium are insulators due to their very wide bandgaps and lack of free charge carriers [6], while common oxides such as zinc oxide, indium oxide, tin oxide and gallium oxide are intrinsic n-type materials. It is difficult to achieve p-type doping in them [7], therefore fabrication of a p-n homojunction in these oxides is not feasible. In order to overcome the challenge of p-doping in n-type metal oxides, fabrication of p-n heterojunctions between p-type and n-type metal oxides is being considered. The semiconducting properties of transition metal oxides are often explored so as to develop electronic devices based on the semiconducting oxides.

Nickel oxide (NiO) is one of the transition metal oxides that is known for exhibiting intrinsic p-type conductivity, it has a direct and wide bandgap. NiO in the thin film form has been used in some electronic and electrochemical applications. These films were usually fabricated using physical or physical-chemical vapour deposition methods such as thermal evaporation [8] and sputtering [9]. These methods often require high temperature and ultra-high vacuum. The chemical solution methods (of fabrication of thin films) such as chemical bath deposition (CBD), sol-gel spin coating and spray pyrolysis are simple and are economical when compared to the physical and chemical vapour deposition methods [10].

1.2 Aims and objectives

The research in this thesis is aimed at the fabrication of NiO thin films for sensing applications, by means of chemical solution methods and investigating the dependence of properties of the films on deposition conditions. In order to achieve this, the following objectives were set:

• Synthesize NiO thin films using chemical bath deposition, sol-gel spin-coating and spray pyrolysis.

• Vary some of the conditions of deposition (of each method) and characterise the films in order to study the effects of the variations on the properties of the films.

• Fabricate a heterojunction between NiO and other electronic materials such as metals, silicon and zinc oxide, using appropriate methods and investigate the properties of the junction.

• Apply the NiO thin films and the heterojunction in light and gas sensing applications.

1.3 Delineation of the thesis

This thesis is divided into nine chapters, these chapters are specifically written to provide a description of the research into synthesis of NiO thin films for sensing applications by chemical solution methods. The present chapter (Chapter 1) gives an introduction to the thesis. Chapter 2 provides the fundamentals of semiconductor physics. Chapter 3 ia the literature survey on chemical solution deposition, NiO, photodetectors and gas sensors. Details of experimental and analytical techniques that were employed in the research are described in Chapter 4. The discussion of results arising from a series of experiments that led to the fabrication of the device for sensing are discussed in the next four chapters.

Chapter 5 highlights the fabrication of thin films of NiO using the chemical bath method. Ammonia and monoethanolamine were used as complexing agents and the fabrication was done at different temperatures. The effects of annealing on the structural properties of the fabricated films are discussed in the chapter. In Chapter 6, thin films of NiO were deposited using the sol-gel spin-coating method. Effects of thermal treatment on the properties of the film were studied. The characterization of an aluminium Schottky diode on NiO fabricated on p-type silicon is also discussed in the chapter. Chapter 7 discuss the fabrication of NiO thin films using a custom-made spray pyrolysis system which was optimised by varying the concentration of the precursor solution.

Chapter 8 discusses the fabrication of a heterojunction between NiO and ZnO and the electrical characterization of the junction. The application of the heterojunction in light sensing was also discussed. Lastly, the summary of the findings in this work and recommendations for future work are given in Chapter 9.

References

[1] Stephen J. Sweeney and Jayanta Mukherjee. *Optoelectronic Devices and Materials*, pages 1–1. Springer International Publishing, Cham, 2017.

[2] Ian M. Baker. *II-VI Narrow Bandgap Semiconductors: Optoelectronics*, pages 1–1. Springer International Publishing, Cham, 2017.

[3] Max N Yoder. Wide bandgap semiconductor materials and devices. *IEEE Transactions on Electron Devices*, 43(10):1633–1636, 1996.

[4] José Millán, Philippe Godignon, Xavier Perpiñà, Amador Pérez-Tomás, and José Rebollo. A survey of wide bandgap power semiconductor devices. *IEEE transactions on Power Electronics*, 29(5):2155–2163, 2013.

[5] U Schühle and Jean-Francois Hochedez. Solar-blind UV detectors based on wide band gap semiconductors. *ISSI SR-009*, pages 429–439, 2010.

[6] Katharina Grossmann, Udo Weimar, and Nicolae Barsan. Semiconducting metal oxides based gas sensors. In *Semiconductors and Semimetals*, volume 88, pages 261–282. Elsevier, 2013.

[7] David C Look and Bruce Claflin. P-type doping and devices based on ZnO. *Physica Status Solidi (b)*, 241(3):624–630, 2004.

[8] Sónia Pereira, Alexandra Gonçalves, Nuno Correia, Joana Pinto, Luís Pereira, Rodrigo Martins, and Elvira Fortunato. Electrochromic behavior of NiO thin films deposited by e-beam evaporation at room temperature. *Solar Energy Materials and Solar Cells*, 120:109–115, 2014.

[9] H Sato, T Minami, S Takata, and T Yamada. Transparent conducting p-type NiO thin films prepared by magnetron sputtering. *Thin solid films*, 236(1-2):27–31, 1993.

[10] Robert W Schwartz, Theodor Schneller, and Rainer Waser. Chemical solution deposition of electronic oxide films. *Comptes Rendus Chimie*, 7(5):433–461, 2004.

Chapter 2

Semiconductor theory

2.1 Introduction

This chapter presents the basic theoretical background that is required for the understanding of the properties of semiconductor materials. Some topics such as transport mechanisms, p-n junction, and heterojunctions are highlighted.

2.2 Band structure of materials and electrical conductivity in conductors

The arrangement of bands, range of energies within the bands and occupation of electrons in the bands determine the electrical and optical properties of a material. The details of the description of the arrangement of these bands are given by [1]. Based on the energy bandgaps, materials are therefore classified as conductors, semiconductors (E_g ranges from 1 eV to 2 eV) and insulators ($E_g \approx 10$ eV) [2]. In conductors, the conduction and valence bands overlap each other; this makes it easy for the materials to conduct electricity. The Drude's theory of metals explained by [3], provides an explanation to the electronic conduction in conductors. The conduction is due to the flow or drift of electrons under the influence of an electric filed, $\vec{E}$ [4, 5].

According to Ashcroft [6], the current density, J, the current per unit area through the conductor, can be expressed as $J = nev$ where n is the number of electrons per unit volume (or carrier density) of the conductor, e is the electronic charge, and v is the drift velocity of electrons. And the relationship between the current density and the electrical conductivity σ is:

$$J = nev = ne\mu\vec{E} = \sigma\vec{E} \tag{2.1}$$

σ is given as: $\sigma = ne\mu$, and depends on the carrier concentration and the mobility, μ, of electron in the material.

2.3 Semiconductors

Semiconductors are a group of materials having electrical conductivities intermediate between metals and insulators. Conductivity of semiconductors depends mostly on temperature, optical excitation, and the concentration of impurities, also known as defects. Elements such as silicon and germanium in the group IV of the periodic table are called elemental semiconductors. Compound semiconductors are formed from the combination of elements, e.g. from group II and VI or group III and V elements. Two-element compound semiconductors, eg. II–VI and III–V compounds, are referred to as binary compounds, three-element and four-element semiconductors are called ternary and quaternary compounds respectively. The bandgap of semiconductors is a major characteristic that distinguishes them from metals and insulators. The bandgap is not greater than 3 eV for common semiconductors, e.g it is 0.67 eV for germanium, 1.12 eV for silicon, and 1.42 eV for gallium arsenide [1]. Some metal oxides are known for having semiconductor properties and they have wide bandgaps, eg. the bandgap of zinc oxide 3.37 eV [7], and the bandgap of nickel oxide varies between 3.6 and 4.0 eV [8]. Electrical conduction in a semiconductor depends on carriers (which are electrons and holes) and the mobility of these carriers [2].

2.3.1 Intrinsic and extrinsic semiconductors

At 0 K, an intrinsic or pure semiconductor has no electrons in the conduction band so it is an insulator. At room temperature, a number of electrons acquire enough energy to move across the bandgap into the conduction band. They occupy some of the available empty states at the bottom of the conduction band. In the valence band, a number of empty states are created as a result of the migrated electrons; these empty states are referred to as holes. In intrinsic semiconductors, the concentration of electrons n is always equal to the concentration of holes p, this is usually referred to as intrinsic carrier concentration n_i . Thus

$$n = p = n_i \tag{2.2}$$

When a foreign atom such as an atom of group III or group V elements, is introduced into the lattice structure of group IV elements, electrons in the valence shell of these atoms take part in covalent bond with neighbouring group IV atoms. This leads to having excess of holes or electrons in the structure. Foreign atoms that are intentionally introduced into the intrinsic semiconductor to modify its conductivity are called dopants, dopants from group III elements are called acceptors while dopants from group V elements are called donors. Acceptors produce excess holes in the semiconductor while donors produce excess electrons. Thus in an extrinsic semiconductor, the concentration of one type of carrier is more than the concentration of the other. The carriers which are in excess are called the majority carriers and other type of carriers are the minority carriers. In a semiconductor that is doped with acceptor atoms, holes are the majority carriers. This semiconductor has more positively charged carriers so it is referred to as a p-type semiconductor. N-type semiconductors have more negatively charged carriers (electrons).

The addition of pentavalent atoms into an intrinsic semiconductor, introduces an energy level just below the conduction band in the forbidden gap. At 0 K, this impurity level is completely filled with electrons. When the temperature of the semiconductor increases, electrons in the impurity level are easily donated into the conduction band, thus the level is referred to as donor level. However, the addition of trivalent atoms into the intrinsic semiconductor creates an energy level just above the valence band. This level is empty at 0 K, and as the temperature

of the semiconductor increases, electrons in the valence band require require only a small amount of energy to be excited into this impurity level thereby creating holes in the valence band. Since electrons are accepted into the impurity level; it is therefore called an acceptor level [2].

2.4 Transport mechanism in semiconductors

Movement of carriers in a semiconductor can be caused by an applied electric field $\vec{E}$ and concentration gradient of the carriers. Since holes and electrons are involved in the electrical conductivity of a semiconductor, it is necessary to account for the contribution of both carriers in the expression for the electrical conductivity of a semiconductor.

2.4.1 Drift of carriers

Under low field, the drift velocity of the carriers is proportional to the applied electric field, as shown in equation 2.1. The mobility depends on scattering with phonons in the semiconductor. Scattering of carriers can also occur in a number of processes such as ionized impurity scattering, deformation potential scattering, piezoelectric potential scattering and polar optical scattering, as explained by [4]. The combined mobility when two or more scattering processes are involved is given by the Mathiesen rule:

$$\frac{1}{\mu} = \sum_i \frac{1}{\mu_i} \tag{2.3}$$

When a semiconductor is in an electric field, both types of carriers drift in the field, the direction of drift is opposite to each other, but the net current due to drift of majority carriers is in the same direction. The total current density in the semiconductor is the sum of current density due to drift of electrons and current density due to drift of holes, thus equation 2.1 can be modified to take into account the contribution of both types of carrier into the conductivity of the semiconductor as [2]:

$$J = nq\mu_e E + pq\mu_p E \tag{2.4}$$

where q is the electronic charge, p is the hole carrier density, μ_e and μ_p are the mobility of electrons and holes respectively.

2.4.2 Resistivity and Hall effect

When an electric current flows through a conductor in a magnetic field, the magnetic field exerts a transverse force on the charges, thereby pushing them to one side of the conductor. This phenomenon is known as the Hall effect. It was discovered in 1879 by Edwin Hall [9] and it is often used to measure the carrier concentration and mobility of carriers in a semiconductor. Figure 2.1 shows a geometry of the Hall effect in a conductor in the form of a rectangular slab of width w and thickness t.

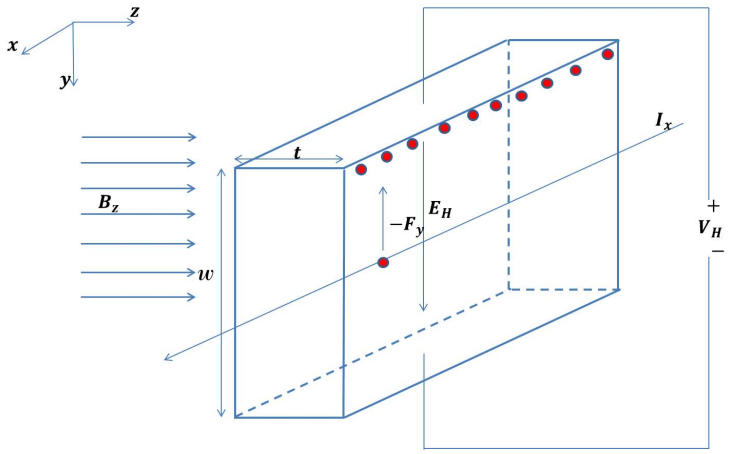

Figure 2.1: Schematic illustration of the Hall effect in a conductor.

In the figure, positive charges (holes) drift in the direction of conventional current along the positive x-axis with a velocity v_x, the magnetic field B_z is applied along the positive z-axis. Each hole experiences a Lorentz force given by:

$$\vec{F}_y = q(\vec{v}_x \times \vec{B}_z) \tag{2.5}$$

The force is in the direction of the negative y-axis, therefore holes accumulate under the top

surface (inside) the conductor. Since B_z is perpendicular to v_x, F_y is simply equal to qv_xB_z. The velocity of holes is related to the current density along x-axis according to equation 2.1 as:

$$J_x = pqv_x \tag{2.6}$$

p is the number of holes and q is the charge.

A potential difference is set up across the width of the conductor as a result of the accumulation of holes at the top surface of the conductor. This potential difference is called the Hall voltage V_H. The electric field that results from this voltage is the Hall field E_H, and is along the positive y-axis. The relationship between V_H and E_H is:

$$E_H = \frac{V_H}{w} \tag{2.7}$$

Since there is no net current along the y-axis, the Lorentz force on each hole must be balanced by the Hall field force, thus,

$$qE_H = qv_xB_z \tag{2.8}$$

Therefore,

$$E_H = v_xB_z = \frac{J_xB_z}{pq} = R_HJ_xB_z \tag{2.9}$$

where R_H, the Hall coefficient is given as:

$$R_H = \frac{1}{qp} \tag{2.10}$$

From equations 2.7 and 2.9, concentration of holes in the conductor can be expressed as:

$$p = \frac{J_xB_zw}{qV_H} = \frac{I_xB_z}{qtV_H} \tag{2.11}$$

The resistance R to the flow of current in the conductor is proportional to the length l of the

conductor and inversely proportional to the area of its cross-section A. The constant of the proportionality is the resistivity of the material, which is given as:

$$\rho = \frac{RA}{l} = \frac{Rwt}{l} \tag{2.12}$$

The electrical conductivity is proportional to mobility of carriers according to equation 2.1 and it is the inverse of resistivity. Mobility of holes in the conductor can then be expressed as:

$$\mu_p = \frac{1}{\rho pq} = \frac{R_H}{\rho} \tag{2.13}$$

Equation 2.13 shows that carrier mobility may be determined from the Hall coefficient and the resistivity of the material [10].

2.4.3 Diffusion

Diffusion occurs when there is a concentration gradient in a device, carriers will move from the region of higher concentration to the region of low concentration until they are uniformly distributed in the device. The flux of carriers during diffusion, which constitutes the diffusion current is given by Fick's first law of diffusion [2]:

$$\frac{dp}{dt} = -D_p \frac{dp}{dx} \tag{2.14}$$

and

$$\frac{dn}{dt} = -D_n \frac{dn}{dx} \tag{2.15}$$

for diffusion of holes and electrons respectively. In these equations, D_p and D_n are diffusion coefficients for holes and electrons respectively. The diffusion currents which arise from the flux of holes and electrons are given as:

$$J_p = -qD_p\frac{dp}{dx} \tag{2.16}$$

$$J_n = qD_n\frac{dn}{dx} \tag{2.17}$$

When diffusion and drift mechanisms occur simultaneously, the total current density due to a carrier is the sum of its drift and diffusion current components, thus current density due to holes and electrons are given as

$$J_p = q\mu_p pE - qD_p\frac{dp}{dx} \tag{2.18}$$

and

$$J_n = q\mu_e nE + qD_n\frac{dn}{dx} \tag{2.19}$$

respectively. The total current density at any point is the sum of current densities of holes and electrons [2].

$$J = J_n + J_p \tag{2.20}$$

2.5 Junctions

A junction is formed where two regions of different conductivities are in contact. Junctions are usually formed in a semiconductor between p- and n-type materials, or between a heavily doped ($p^+$and n^+) and lightly doped (p and n) materials of the same conductivity. These junctions can be described as pn, p^+ p and n^+ n. If the regions are in the same semiconductor material, the junction is referred to as a homojunction. A heterojunction is formed when the regions are in different materials, and these materials usually have different bandgaps [1]. A junction can also be found between a metal and a semiconductor.

2.5.1 p-n junction under forward and reverse bias

A pn junction is formed between a p-type semiconductor and an n-type semiconductor. When the junction is formed and it is unbiased, diffusion of majority carriers takes place across the junction; holes diffuse from p-type material and ionized acceptor atoms (N_a^-) are left behind. Similarly electrons diffuse from the n-type material, thereby leaving ionized donor atoms (N_d^+) in the n-type material. An electric field $\vec{E}$ builds up across the junction as a result of these immobile charged dopant atoms. The direction of $\vec{E}$ is from charged donor atoms in the n-type to the charge acceptor atoms in the p-type material. When the electric field is high enough, it opposes diffusion of majority carriers, and drift of minority carriers begins to take place across the junction. Diffusion and drift currents continue to flow until the net current across the junction is zero at equilibrium. At this point, the region around the junction is depleted of carriers and it is called depletion region (or transition or space charge region). The electric field appears over the depletion region and a built-in potential (V_{bi}) is developed internally across the depletion region. The built-in potential results from the difference between the potentials at the n- and p- regions,

$$V_n - V_p = V_{bi} \tag{2.21}$$

The built-in potential is also a measure of difference in energy between the quasi-Fermi levels in isolated n- and p-type materials before the junction is formed, i.e.

$$E_{fn} - E_{fp} = qV_{bi} \tag{2.22}$$

where q is the electronic charge. The built-in potential can be expressed in terms of doping concentration in each side of the junction as [2]:

$$V_{bi} = \frac{kT}{q} ln \frac{N_a N_d}{n_i^2} \tag{2.23}$$

When an external bias, V_a, is applied across a pn junction, and it makes the potential at the p-type semiconductor higher than that of the n-type semiconductor, the external bias is positive and the junction is said to be forward biased. The junction is reversed biased if the polarity

of the external bias is reversed. Under the condition of forward bias, the internal potential becomes:

$$V'_{bi} = V_{bi} - V_a \tag{2.24}$$

This implies that the built-in potential is reduced, the width of the depletion region is also reduced and diffusion current flows across the junction. Under reverse bias, V_a is negative, there is an increase in the built-in potential and the width of the depletion region. Consequently drift current flows across the junction, when all the minority carriers are involved in the drift current, the reverse current is constant and it is termed reverse saturation current. The current that flows across an ideal pn junction can be described by the ideal diode equation:

$$I = I_s[e^{\frac{qV_a}{kT}} - 1] \tag{2.25}$$

where V_a is the external bias and I_s is the saturation current. When the forward bias is greater than $3kT/q$, the exponential term is much greater than unity for all $V_a > 0$, so the forward current increases exponentially with V_a.

A sketch of the variation of the Fermi level along the material is shown in Figure 2.2(b) and (c).

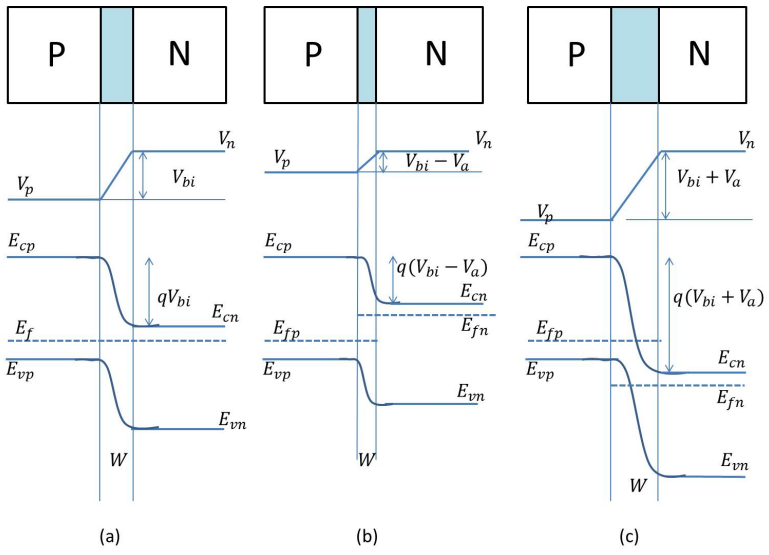

Figure 2.2: Variation in width of the depletion region, junction barrier and Fermi level in (a) unbiased, (b) forward biased, and (c) reversed biased pn junction. Redrawn from [2].

2.5.2 Metal-semiconductor junctions

A metal-semiconductor junction is formed when a metal is in contact with a semiconductor. A Schottky contact is a rectifying metal-semiconductor junction. Ohmic contacts are non-rectifying metal-semiconductor junctions, they are of importance in making electrical connection to electronic devices. A metal-semiconductor junction may be ohmic or Schottky depending on the properties of the metal and semiconductor. The major property of concern in a metal is the electronic work function Φ_m. This is defined as the minimum energy that is required to move an electron from the Fermi level of a metal to a point in the vacuum outside its surface [11]. In the semiconductor, the work function Φ_s as well as the electron affinity χ, the minimum energy required to move an electron from the bottom conduction band to a point in the vacuum outside the semiconductor, plays an important role in determining if a metal-semiconductor junction will be a Schottky or ohmic contact.

(a) Schottky junction with a p-type semiconductor

A Schottky junction is formed between a metal of work function Φ_m and a p-type semiconductor with a work function of Φ_s, if $\Phi_m < \Phi_s$. Initially the Fermi level in the semiconductor is lower than that of the metal. In order to align the two Fermi levels when the contact is made, the electrochemical potential of the semiconductor has to be lowered. The band diagram of a metal and a p-type semiconductor before and after forming the junction is shown in Figure 2.3. Diffusion of holes from the p-type semiconductor to the metal leaves ionized acceptor atoms in the semiconductor side of the junction, thereby making the p-side to be more negatively charged. A depletion region is formed in the semiconductor near the junction as the positive charge in the metal matched the uncompensated acceptor atoms, and an electric field is formed across the depletion region. At equilibrium, the potential barrier, qV_{bi} that prevents further diffusion of holes is developed, the potential barrier is equal to the difference between work functions of the semiconductor and the metal, i.e.

$$qV_{bi} = \Phi_s - \Phi_m \tag{2.26}$$

In terms of the Fermi level of the p-type semiconductor, $E_{F,p}$, the valence band edge, E_v, and the electron affinity, χ, and bandgap E_g, of the semiconductor, the potential barrier can be expressed as:

$$qV_{bi} = \chi_s + E_g - (E_{F,p} - E_v) - \Phi_m \tag{2.27}$$

The Schottky barrier height, Φ_B, of the p-type semiconductor is the difference between the Fermi level of the metal and the band edge where the majority carriers reside (the valence band in a p-type semiconductor). The Schottky barrier height is given as [10]:

$$\Phi_B = E_g + \chi - \Phi_m \tag{2.28}$$

From Equations 2.27 and 2.28, the Schottky barrier and the barrier height are related as:

$$\Phi_B - qV_{bi} = (E_{F,p} - E_v) \tag{2.29}$$

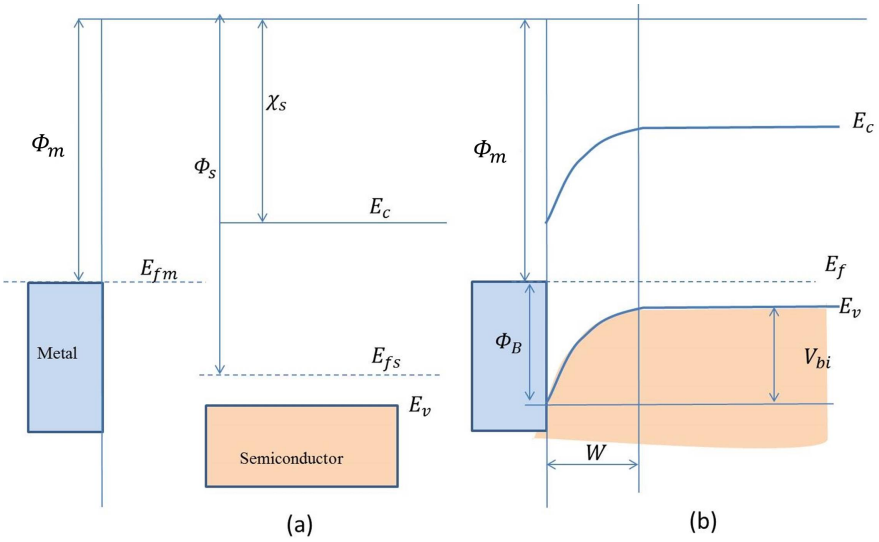

Figure 2.3: Band diagram of metal and semiconductor forming a Schottky junction (a) before and (b) after joining. Redrawn from [2].

The junction is said to be forward biased if the semiconductor is connected to a more positive potential than the metal. Under a forward bias, the applied voltage V_a is positive, the contact potential becomes $V_{bi} - V_a$, the width of the depletion region is reduced, consequently diffusion of holes from the semiconductor to the metal across the depletion region is favoured. A reverse bias, $-V_a$, increases the contact potential to $V_{bi} + V_a$. It increases the width of the depletion

region, thereby preventing the diffusion of holes from semiconductor to metal. The movement of holes from metal to semiconductor is hindered by Schottky barrier height, it is not affected by bias voltage [2].

(b) Ohmic contact with a p-type semiconductor

When the work function of a metal, Φ_m, is greater than work function of a p-type semiconductor, Φ_s, an ohmic contact is formed at the junction of the metal and semiconductor. The Fermi levels are aligned by the movement of holes from semiconductor to the metal. No depletion region is formed in the semiconductor and the electrostatic potential difference required to align the Fermi levels brings about accumulation of holes in the semiconductor. The barrier to the flow of holes across the junction in both directions is small. Figure 2.4 shows the band diagram of a metal-semiconductor junction that forms an ohmic contact.

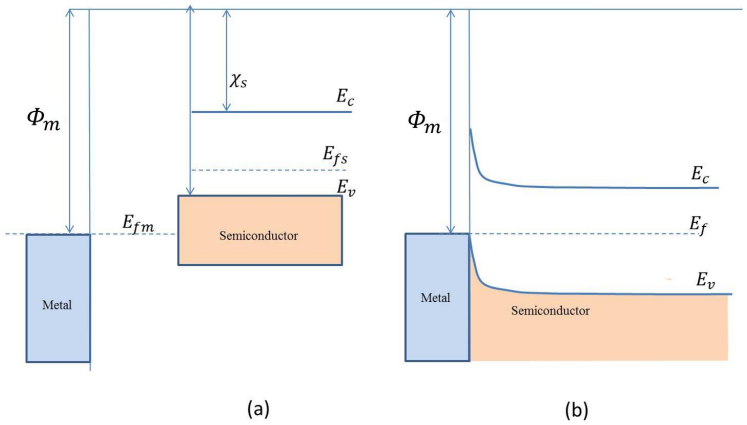

Figure 2.4: Band diagram of metal and semiconductor forming an Ohmic junction (a) before and (b) after joining. Adapted from [2].

(c) Depletion region in Schottky diode and junction capacitance

The width of depletion region in a Schottky diode can be estimated by solving the Poisson equation and using the depletion approximation that the depletion region only contains immobile ionized atoms. In a p-type semiconductor, the ionized atoms are acceptors. The Poisson equation can be written for the depletion region as:

$$\frac{d^2\phi}{dx^2} = \frac{-\rho}{\epsilon_s} = \frac{qN_a}{\epsilon_s} \tag{2.30}$$

where N_a is the acceptor concentration and ϵ_s is the permittivity of the semiconductor. Integration of equation 2.30 within x and the width of the depletion region W gives the potential gradient along the junction. Thus,

$$\frac{d\phi(x)}{dx} = \frac{qN_a}{\epsilon_s}(W - x). \tag{2.31}$$

The electric potential $\phi(x)$ and the electric field is zero in the bulk of the semiconductor, outside the depletion region. Integration of equation 2.31 gives the electric potential along the semiconductor as a function of x:

$$\phi(x) = \frac{qN_a}{2\epsilon_s}(W - x)^2 \tag{2.32}$$

At $x = 0$, the electric potential is the built-in potential under bias, therefore

$$\frac{qN_a}{2\epsilon_s}W^2 = (V_{bi} - V_a) \tag{2.33}$$

$$W = \sqrt{\frac{2\epsilon_s(V_{bi} - V_a)}{qN_a}} \tag{2.34}$$

The equation shows that the width of the depletion region depends on the external bias. The electric field at the surface of the metal $x = 0$ can be obtained from equation 2.31 as:

$$E(0) = \frac{qN_a}{\epsilon_s}W \tag{2.35}$$

The total space charge Q (per unit area) in the semiconductor is given as:

$$Q = qN_aW = \sqrt{2qN_a\epsilon_s(V_{bi} - V_a)} \tag{2.36}$$

The capacitance per unit area of the junction is given as [1]:

$$C = \mid \frac{dQ}{dV} \mid = \sqrt{\frac{qN_a\epsilon_s}{2(V_{bi} - V_a)}} \tag{2.37}$$

Barrier height reduction

When a charge is at a distance from the surface of a conductor which is grounded or at a constant potential, the field outside the metal is the same as if there were an opposite charge inside the metal, the same distance from the surface [12]. Consequently, an electron at a position x in a semiconductor that is in contact with a metal at the surface ($x = 0$), will induce an image charge e at $-x$. The force of attraction between the electron and the image charge is given as [4]:

$$\vec{F}(x) = -\frac{e^2}{16\pi\epsilon_0\epsilon_s x^2} \tag{2.38}$$

where ϵ_s is the relative dielectric constant of the semiconductor, ϵ_0 is the permittivity of free space. The potential energy at a given position x is:

$$U(x) = -\frac{e}{16\pi\epsilon_0\epsilon_s x} \tag{2.39}$$

In the presence of an electric field $\vec{E}$, the total energy of an electron is given as the sum of potential energy and the energy given the electron due to the external field [1]. The total energy according to [10] is:

$$U(tot) = -e\vec{E}x - \frac{e}{16\pi\epsilon_0\epsilon_s x} \tag{2.40}$$

The maximum value of $U(tot)$ occurs at a point where the first derivative of equation 2.40 is zero. Therefore the value of x at this point given as x_m can be obtained from:

$$x_m = \sqrt{\frac{e}{16\pi\epsilon_0\epsilon_s\vec{E}}} \tag{2.41}$$

The ideal barrier height, ϕ_{Bo}, is reduced to ϕ_{Bn} due to the image-charge force. The difference $\Delta\phi$ is given as:

$$\Delta\phi = 2Ux_m = \sqrt{\frac{e\vec{E}}{4\pi\epsilon_0\epsilon_s}} \tag{2.42}$$

A sketch of barrier lowering in a Schottky diode due to image-charge force is shown in Figure 2.5

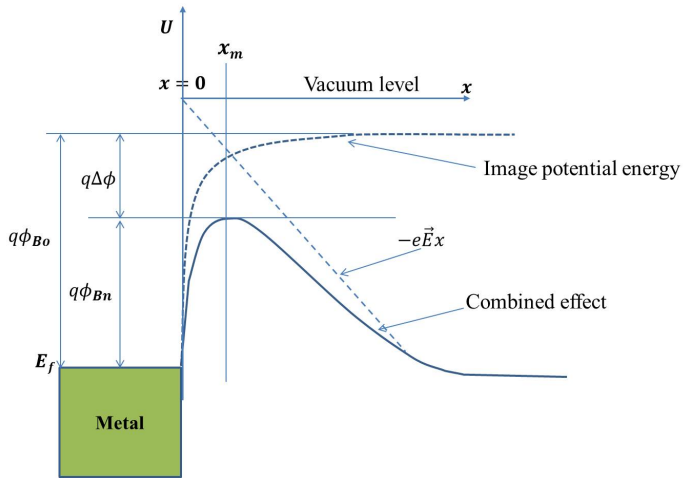

Figure 2.5: Barrier height lowering due to image force in a Schottky junction. Adapted from [10].

2.5.3 Current transport mechanisms in Schottky diodes

In metal-semiconductor contacts, current transport is only due to majority carriers. There are five basic transport mechanisms under forward bias:

(i) Emission of majority carriers from the semiconductor over the potential barrier into the metal, also known as thermionic emission.

(ii) Quantum mechanical tunnelling of majority carriers from semiconductor to metal through the barrier.

(iii) Recombination in the depletion region.

(iv) Diffusion of majority carriers in the depletion region.

(v) Injection of minority carriers from metal and diffusion into the semiconductor [10].

The above-mentioned mechanisms are illustrated in Figure 2.6 for an n-type semiconductor.

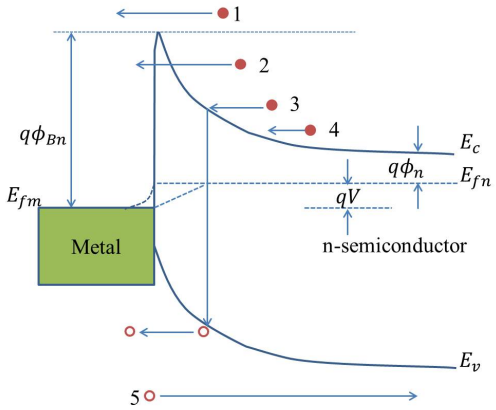

Figure 2.6: Transport mechanisms in metal-semiconductor junctions: (1) thermionic emission, (2) tunnelling, (3) recombination in the depletion region, (4) diffusion of electrons in the depletion region, (5) diffusion into the semiconductor. Redrawn from [10].

2.5.4 Thermionic-emission theory

The current density from semiconductor to metal $J_{s\to m}$ depends on the concentration of electrons having sufficient energy to overcome the potential barrier. Such electrons, called hot electrons, have a minimum energy which is equal to the sum of the Fermi level and the potential barrier $(E_{fn} + q\phi_{Bn})$. The current density is given as [10]:

$$J_{s\to m} = \int_{E_{fm}+q\phi_{Bn}}^{\infty} qv_x dn \tag{2.43}$$

where v_x is is the carrier velocity along x-axis and dn is the electron density in an incremental energy range dE. In terms of velocity v of carriers, dn is expressed as:

$$dn = 2(\frac{m^*}{h}) \exp(-\frac{q\phi_{Bn}}{kT}) \exp(-\frac{mv^2}{2kT}) 4\pi v^2 dv \tag{2.44}$$

All the energy of the hot electrons in the conduction band is taken to be kinetic. The minimum energy needed to overcome the barrier depends on the applied bias, V, and the built-in potential according to the relation:

$$\frac{1}{2}m^* v_x^2 = q(\phi_{bi} - V) \tag{2.45}$$

By using $4\pi v^2 dv = dv_x dv_y dv_z$ and integrating over all velocity in y and z directions and v_x from minimum velocity to overcome the barrier to infinity, the current density becomes:

$$J_{s\to m} = A^* T^2 exp(-\frac{q\phi_{Bn}}{kT}) exp(\frac{qV}{kT}) \tag{2.46}$$

where

$$A^* = \frac{4\pi m^* k^2}{h^3} \tag{2.47}$$

is the effective Richardson constant for thermionic emission.

For carriers moving from the metal to the semiconductor, the barrier height is independent of the applied voltage. At zero bias, there is no net current flowing across the barrier, therefore the current is equal to current flowing from semiconductor to metal. By making $V = 0$ in equation 2.46, the current density from metal to semiconductor $J_{m\to s}$ can be expressed as:

$$J_{m\to s} = -A^* T^2 exp\Big(-\frac{q\phi_{Bn}}{kT}\Big) \tag{2.48}$$

The total current density is the sum of equations 2.46 and 2.48, therefore

$$J = \Big[A^* T^2 exp\Big(-\frac{q\phi_{Bn}}{kT}\Big)\Big]\Big[exp\Big(\frac{qV}{kT}\Big) - 1\Big] \tag{2.49}$$

The first square bracket of the RHS of equation 2.49 is the saturation current density of thermionic emission.

2.5.5 Heterojunctions

A heterojunction is formed between two dissimilar semiconductors. The junction between two materials of different conductivities is described as an anisotype heterojunction. An isotype junction is formed between materials of the same type of conductivity. Heterojunctions can also be classified as graded and abrupt depending on the distances over which the transition from one material to the other takes place [13]. The difference in the bandgap and electron affinity

of semiconductors gives room for various combinations of different materials in order to achieve devices with specific properties for different applications. Some applications of heterojunctions include: room temperature injection lasers, light emitting diodes, photodetectors and solar cells [10]. In these devices, heterojunctions are either used to restrict the flow of carriers or to collect carriers where they are needed [14].

Different combinations of conduction and valence band alignments, which occur at the interface of materials forming a heterojunction, leads to three different types of heterojunctions, these are:

- Type–I or straddling heterojunction,
- Type–II or staggered heterojunction,
- Type III or broken-gap heterojunction.

The schematic drawing of the band alignments of these heterojunctions is shown in Figure 2.7.

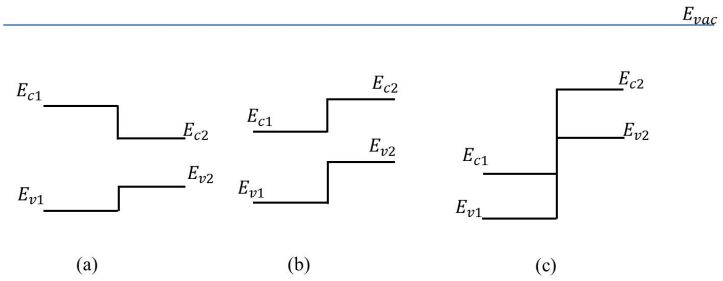

Figure 2.7: Types of band alignment in a heterojunction: (a) straddling, (b) staggered, (c) broken-gap. Redrawn from [10].

Band structures of heterojunctions are often characterized by discontinuities in band bending, which result in band offsets. Band offsets are the difference in the conduction band edge, ΔE_c, and in valence band edge, ΔE_v, of the materials. Using the energy-band model or electron affinity rule proposed by Anderson [15], the band diagram of anisotype heterojunctions between a small band-gap n-type material and a wide band-gap p-type material is shown in Figure 2.8. The band offsets in the conduction and valence bands can be calculated as:

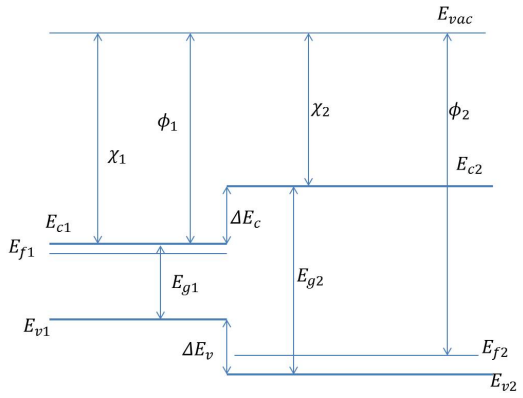

Figure 2.8: Energy band diagrams for an isolated small bandgap n-type and a wide bandgap p-type semiconductors. Redrawn from [15].

$$\Delta E_c = \chi_1 - \chi_2 \tag{2.50}$$

$$\Delta E_v = \Delta E_g - \Delta E_c \tag{2.51}$$

When the junction is formed and it is at equilibrium, the Fermi level is constant through both materials, the vacuum level is continuous and parallel to the band edges. The energy band diagram at equilibrium is shown in Figure 2.9. The band offsets do not change with doping. The built-in potential V_{bi} is a measure of the difference in Fermi levels of the materials before the junction is formed, i.e.

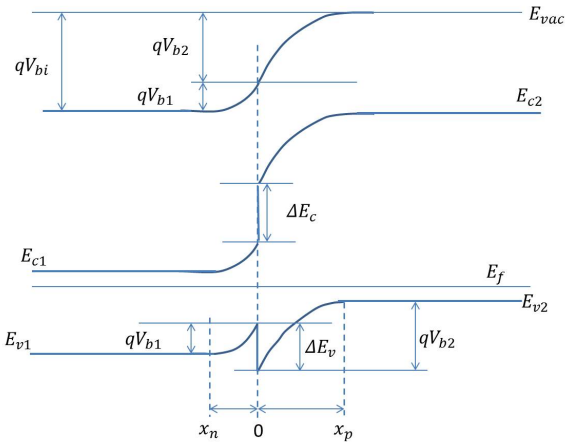

Figure 2.9: Energy band diagram of an anisotype heterojunction at thermal equilibrium [15].

$$qV_{bi} = E_{f2} - E_{f1} \tag{2.52}$$

When the Fermi levels are referenced to the vacuum level, the built-in potential is the difference between the workfunctions of the materials. The built-in potential can be expressed in terms of electrostatic potentials supported in semiconductors 1 and 2; V_{b1} and V_{b2} respectively as:

$$V_{bi} = V_{b1} + V_{b2} \tag{2.53}$$

The region around the junction is completely devoid of carriers over a distance x_n and x_p into n- and p-type materials respectively. In order to maintain charge neutrality in the depletion region,

$$\frac{x_n}{x_p} = \frac{N_A}{N_D} \tag{2.54}$$

By solving Poisson's equation for the step junction on either side of the interface, the width of the depletion region (x_n and x_p) in n-type and p-type materials are found to be [1]:

$$x_p = \sqrt{\frac{2\epsilon_1\epsilon_2 N_d \phi_{bi}}{qN_a(\epsilon_1 N_d + \epsilon_2 N_a)}} \tag{2.55}$$

$$x_n = \sqrt{\frac{2\epsilon_1\epsilon_2 N_a \phi_{bi}}{qN_d(\epsilon_1 N_d + \epsilon_2 N_a)}} \tag{2.56}$$

where ϵ_1 and ϵ_2 are the permittivity of the n-type and p-type materials respectively.

Reverse-biased heterojunction

When the heterojunction is biased such that the applied voltage V_a is negative. The built-in potential becomes $V_{bi} - V_a$ consequently, there is an increase in the width of the depletion region. The Fermi level in the n-type material is shifted below the equilibrium level by qV_a. There is a small negative current as a result of generation and recombination in the quasi-neutral regions. Concentration of electrons on the p-side and concentration of holes on the n-side are pulled down below the equilibrium concentrations because the drift component of electron and hole currents exceed diffusion components. The large electric field in the depletion region sweeps minority carriers across the depletion region into the quasi-neutral regions. This

causes minority carrier generation rate to exceed recombination rate in these regions.

Forward-biased heterojunction

Under forward bias, the applied voltage is positive, therefore, there is a reduction in the built-in potential and the width of the depletion region is smaller. The Fermi level in the n-type material is shifted above the equilibrium level by qV_a. Electrons and holes are injected into the p- and n-side respectively. The electron and hole current densities are given as:

$$J_n = \frac{qD_n n_{i1}^2}{N_a L_n}[e^{\frac{qV_a}{kT}} - 1] \tag{2.57}$$

$$J_p = \frac{qD_p n_{i1}^2}{N_d L_p}[e^{\frac{qV_a}{kT}} - 1] \tag{2.58}$$

where L_n and L_p are width of the depletion region in the n- and p-type materials respectively. The ratio of electron to hole current in the pn heterojunction is exponentially proportional to the difference of energy bandgaps between the two semiconductors.

References

[1] J-P Colinge and Cynthia A Colinge. *Physics of semiconductor devices*. Springer Science & Business Media, 2005.

[2] Ben G Streetman and Sanjay Kumar Banerjee. *Solid State Electronic Devices: Global Edition*. Pearson education, 2016.

[3] Neil W Ashcroft and N David Mermin. Solid state physics (saunders college, philadelphia, 1976). *Appendix N*, 2010.

[4] Marius Grundmann. *The physics of semiconductors: an introduction including nanophysics and applications*. Springer, 2015.

[5] Safa Kasap, Cyril Koughia, and Harry E Ruda. Electrical conduction in metals and semiconductors. In *Springer Handbook of Electronic and Photonic Materials*, pages 1–1. Springer, 2017.

[6] Neil W Ashcroft, N David Mermin, et al. Solid state physics, 1976.

[7] JM Nel, FD Auret, L Wu, MJ Legodi, WE Meyer, and M Hayes. Fabrication and characterisation of NiO/ZnO structures. *Sensors and Actuators B: Chemical*, 100(1-2):270–276, 2004.

[8] Mahendra Singh Yadav and SK Tripathi. Synthesis and characterization of nanocomposite NiO/activated charcoal electrodes for supercapacitor application. *Ionics*, 23(10):2919–2930, 2017.

[9] Edwin H Hall. On a new action of the magnet on electric currents. *American Journal of Mathematics*, 2(3):287–292, 1879.

[10] Simon M Sze and Kwok K Ng. *Physics of semiconductor devices*. John wiley & sons, 2006.

[11] Guomin Hua and Dongyang Li. Electron work function: a novel probe for toughness. *Physical Chemistry Chemical Physics*, 18(6):4753–4759, 2016.

[12] John David Jackson. *Classical electrodynamics*. John Wiley & Sons, 2012.

[13] BL Sharma and RK Purohit. *Semiconductor heterojunctions*, volume 5. Elsevier, 2015.

[14] Joachim Piprek. *Semiconductor optoelectronic devices: introduction to physics and simulation*. Elsevier, 2013.

[15] Richard L Anderson. Experiments on Ge-GaAs heterojunctions. In *Electronic Structure of Semiconductor Heterojunctions*, pages 35–48. Springer, 1988.

Chapter 3

Literature review of device preparation, nickel oxide (NiO) and device applications

3.1 Introduction

A review of the literature on methods of deposition of thin films is presented in this chapter. More emphasis is laid on chemical solution methods, being the methods of interest in this research. Reviews on gas sensing, semiconductor metal oxide gas sensors, and nickel oxide are also presented.

3.2 Thin-film deposition methods

Methods of deposition of thin films can be divided into two main categories: physical and chemical deposition methods. The physical methods include all evaporative processes, while chemical methods include gas- and liquid phase processes. A number of deposition methods such as sputtering involve both physical and chemical processes so they are classified as physical-chemical methods. Figure 3.1 shows the classification scheme based on the methods mentioned

above. Physical vapour deposition techniques are suitable for deposition of high-quality films with uniform morphology, thickness, and purity. The major limitation of the physical methods is the expensive vacuum techniques that they require [1]. Chemical vapour deposition (CVD) techniques require vacuum and high temperature, hence they are also expensive. Chemical depositions in the liquid phase (solution) are known as chemical solution methods, examples include chemical bath deposition (CBD), successive ion layer adsorption and reaction (SILAR), sol-gel, spin coating, dip coating and spray pyrolysis. These methods are cheaper and are invaluable in the deposition of thin films.

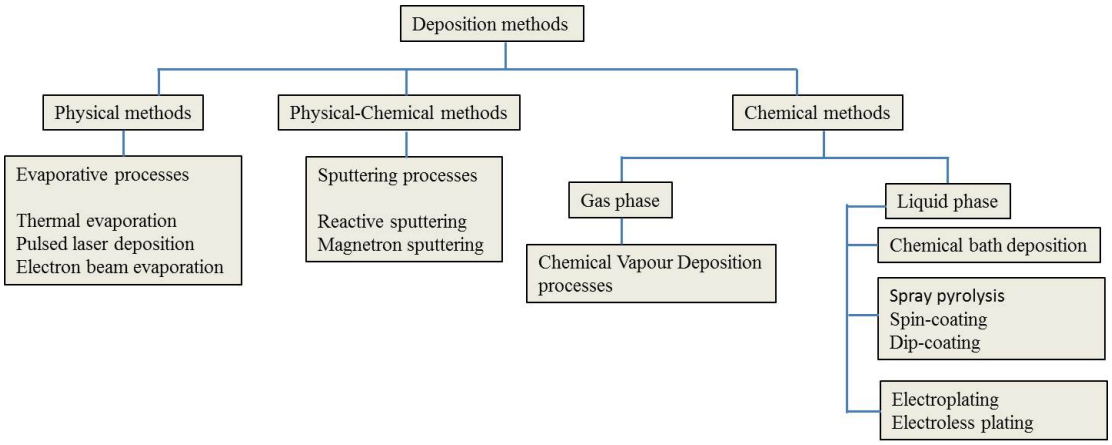

Figure 3.1: Methods of deposition of thin films [1].

3.2.1 Chemical bath deposition

The CBD method uses a controlled chemical reaction to cause the deposition of a thin film by precipitation. CBD was first described in 1884 when PbS was deposited by Emerson-Reynolds using thiourea and alkaline lead tartrate [2, 3, 4]. The method has since been used to deposit films of many binary and ternary compounds of sulphides, selenides, and oxides; the films were found to be of comparable quality as those deposited using sophisticated and expensive physical deposition processes. The CBD method does not require a vacuum and can be carried out with simple equipment like the hot plate, magnetic stirrer, and beakers. The precursors and complexing agents are relatively cheap; reaction in the chemical bath takes place at low temperatures (300 to 353 K), this favours deposition on materials that cannot withstand high temperature such as polymers. Similarly deposition can be made on metallic substrates which cannot be oxidized at such temperatures. CBD can be used to grow thin films on substrates

of different shapes and sizes and deposition can be made on a number of substrates in a single process [5]. Due to its relative simplicity, low cost, low temperature, scalability and good control over the deposition process, CBD is considered more advantageous than physical deposition methods [6]. The technique is mostly used for the preparation of metal chalcogenide thin films [7].

Deposition of thin films of metal chalcogenides using CBD

Chalcogenides are elements in group six of the periodic table. In a typical procedure for deposition of thin film of metal chalcogenides using CBD, substrates are immersed in a solution containing ions (usually metal and chalcogenide ions) that are required for the formation of the required compound, a base, and a complexing agent. In the solution, a number of ligand molecules (complexing agents) form a complex with the hydrated metal ions; this reduces the concentration of free metal ions in the solution. The stability of the complex depends on the temperature and pH of the reaction bath. An increase in temperature or a decrease in pH of the solution makes the complex less stable and causes it to dissociate, thereby releasing free metal ions into the solution. Formation of the film takes place as soon as enough metal and chalcogenide ions are present in the solution, at this point the product of concentrations of metal and chalcogenide ions (ionic product) exceeds or is equal to the solubility product of the required insoluble solid necessary for the formation of the metal chalcogenide [2]. Generally, deposition of metal chalcogenide occurs via the following steps [3].

i. The equilibrium between the complexing agent and water;

ii. Formation/dissociation of ionic metal-ligand complexes;

iii. Hydrolysis of the chalcogenide source; and

iv. Formation of the solid.

Kinetics of step iii, is highly sensitive to the pH, the temperature of the solution and to the catalytic effects of surfaces (including surfaces of substrates) that may be present in the solution. This determines the rate of formation of the thin film on the surfaces. When thin films of transition metal oxides are to be deposited using CBD, water is the source of hydroxide ions and the supply of this ion is unlimited in the bath. Hydroxides of the metals, which are usually insoluble in water, are formed as soon as enough metal ions are released into the solution, in

some cases; hydrated oxides are formed depending on the stability of the metal hydroxide. The hydroxides are either converted directly to metal oxides by dehydration or through thermal treatment.

3.2.2 Sol-gel deposition

A sol is a dispersion of the solid particles between 0.1 and 1 μm in a liquid, the particles are only suspended by Brownian motions. A gel is a state where both liquid and solid are dispersed in each other [8]. Deposition of thin films using the sol-gel method usually consists of the following steps:

i. Preparation of the desired colloidal suspension (sol) in a liquid.

ii. Deposition of sol solution as coatings on the substrates by spraying, dipping, spinning, printing, rolling, etc.

iii. Polymerization of the particles in the sol through the removal of its stabilizing components to form a gel.

iv. Heat treatment of the gel to form a crystalline film.

The sol is made by dissolving precursors in solvents (polar or non-polar). Precursors used for synthesizing the sol usually consists of a metal surrounded by various active ligands: salts, soluble hydroxides, and alkoxides are common precursors. Stabilizers in the form of bases are usually added to the sol [9] to increase its pH and protect it from premature hydrolysis and condensation. When the precursor is dissolved in water or other solvents, cations form chemical complexes with water or solvent molecules and stabilizing agents. The resulting metal cations undergo hydrolysis and condensation to form a metal oxide skeleton framework with a dense microstructure [10].

3.2.3 Spin coating

Spin coating is a method used to apply uniform thin films on flat substrates. In a typical process, a small quantity of a fluid is deposited at the centre of a substrate and the substrate is spun at high speed [11]. Centrifugal force causes the fluid to spread over and off the edge of the substrate thereby leaving a thin film of fluid on the surface of the substrate due to viscous force and surface tension, a combination of outward flow and evaporation causes the film to thin out. The final film thickness and other properties of the film depend on the nature of the fluid such as viscosity, drying rate, percent solids, etc. The whole process of spin coating is divided into four stages: deposition, spin-up, spin-off and evaporation of solvents. An illustration of these stages is shown in Figure 3.2. Details of these stages and mathematical modelling of the spin coating are provided by [12, 13].

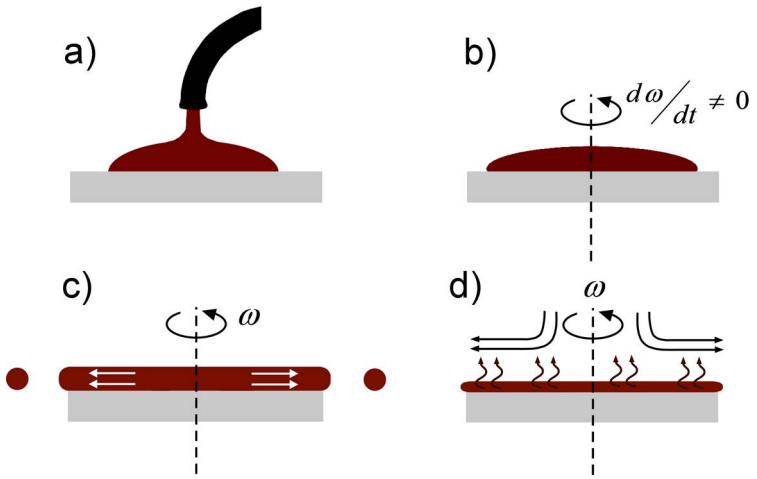

Figure 3.2: Stages of spin coating [12].

3.2.4 Drying and thermal treatment

Drying of films is necessary to remove solvents and other species that are produced during deposition. The temperature at which drying is done depends on the properties of the materials to be removed. Decomposition of some precursors into intermediate products usually takes place during drying [4]. Further heat treatment or annealing of films is necessary for phase transformation and to control the carrier concentration of conducting films [15]. For thin films that are produced from solvents made of metal acetates and heated in air, dehydration takes

place between 80 ℃ and 130 ℃, intermediates are formed between 105 ℃ and 230 ℃ and the intermediates are converted to final products at the decomposition temperature which lies between 100 ℃ and 400 ℃. Heat treatment of metal oxides generally requires temperatures between 350 ℃ and 600 ℃ and heat treatment may be performed in air or in controlled gas atmospheres, which can be provided in a tube furnace or in a rapid thermal processing (RTP) system. The highest temperature at which a film can be annealed is limited by the nature of substrates on which it is deposited.

3.2.5 Spray pyrolysis

The spray pyrolysis deposition of thin film involves the spraying of fine droplets of a precursor solution onto a substrate which is at a high temperature. The temperature is chosen such that the precursor decomposes or constituents of the precursor react to form a desired chemical compound on the substrate. All unwanted products of the reaction in the form of volatile compounds are removed. Properties of the film depend upon the concentration of precursor, spray rate, droplet size, substrate temperature, carrier gas, and the ambient atmosphere. Factors that affect the thickness of the films are: distance between the spray nozzle and substrate, temperature of the substrate, the concentration of the precursor solution and the quantity of the precursor solution that was sprayed. Formation of the film depends on the process of landing of droplets on the substrate and momentum of the droplets [14], the droplet will either flatten, skip along the surface or hover motionless [15]. In order to achieve a uniform deposition, a random motion of the spray head (nozzle), the substrate or both is required. Spraying in bursts or pulses is necessary to achieve constant surface temperature [15].

The atomization process is another important factor that affects film formation in spray pyrolysis. Spray atomization techniques that have been developed to obtain micrometer or submicron size droplets and controlled size distribution are ultrasonic nebulized atomization, spray pyrohydrolysis, corona spray pyrolysis, electrostatic spray pyrolysis, and microprocessor based spray pyrolysis. Details of these atomization techniques are provided by Patil [14]. The spray pyrolysis technique is useful in the deposition of various types and forms of films including ceramic powders [16].

3.3 Nickel (II) oxide

Nickel (II) oxide or nickel monoxide is a binary oxide; it occurs naturally as bunsenite. At high temperatures, above the Néel temperature, T_N, of 525 K (252 ℃), it has a stable cubic crystal structure as shown in Figure 3.3. On cooling the crystal below the Néel temperature, it changes to the rhombohedral structure [17]. NiO has a density of 6.67 g.cm^{-3}, molar mass of 74.6929 g.mol^{-1}, its melting point is 1957 ℃, and it has a dielectric constant of 10. The lattice constant of cubic NiO is 4.1769 Å, according to JCPDS, 47-1049.

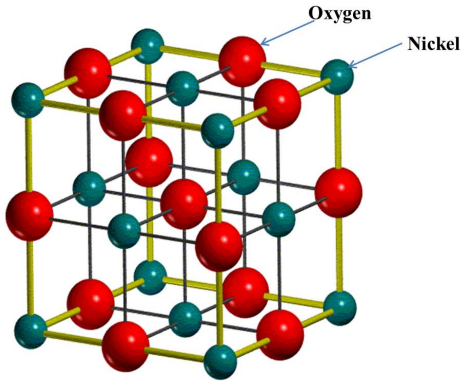

Figure 3.3: Crystal structure of cubic nickel oxide [18].

Stoichiometric NiO is an insulator with a resistivity of the order 10^{13} Ω.cm [19, 20]. The type of conductivity of NiO can be altered through electron doping and hole doping. Electron doping can be achieved by exposing the surface of NiO to a reducing atmosphere thereby depleting it of oxygen and creating Ni^0 like atoms. Hole doping involves removal of electrons from nickel or oxygen sites in NiO to produce nickel defects which lead to Ni^{3+} centres or O^{1-} ions known as oxygen holes. Annealing in air may also result in non-stoichiometric NiO_x, in which nickel cation vacancies V_{Ni} or interstitial oxygen are produced [21]. The non-stoichiometric NiO produced through these processes is said to be an intrinsic p-semiconductor.

Another process through which hole doping can be achieved is through the addition of monovalent atoms such as lithium atoms into the structure of NiO. Li^+ ions replace Ni^{2+} ions at some lattice points in the structure as a result of doping. In order to achieve charge neutrality, O^{1-} ions are created [17]. It is still a matter of debate whether the hole state is of Ni^{3+} or O^{1-}. Apart from doping with lithium [10, 22], copper has been used as a dopant in NiO [23, 24] and

aluminium [25]. Doped NiO is often described as an extrinsic semiconductor. NiO is one of the few metal oxides with p-type conductivity; it was the first known p-type transparent conducting oxide reported by [26]. The conductivity of NiO depends on the method of preparation, grain structure, and its thermal history [27].

Nickel oxide is one of the metal oxides whose charge transport mechanism involves hopping of charge carriers from one site to another. The mechanism is a form of an activated transfer process. Therefore, NiO is described as a charge or electron transfer material. In the hopping mechanism, at high temperature, a charge carrier acquires the activation energy necessary to jump from a cationic site to the adjacent site. It remains in this site until it regains the necessary activation energy to jump into another site. For the material to be conductive, the lattice of NiO must contain nickel ions with two valency states. These ions are obtained by deliberately making NiO non-stoichiometric through an annealing process or valence induction (doping). Annealing NiO in oxygen vapour results in a nickel deficiency or vacancy; two Ni^{3+} ions are formed as per Ni vacancy. Conduction in non-stoichiometric NiO is due to hopping of holes from Ni^{3+} to Ni^{2+}. This process is illustrated in Figure 3.4.

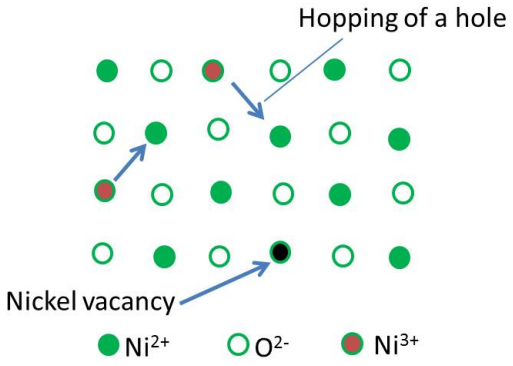

Figure 3.4: Hopping mechanism in a non-stoichiometric NiO.

The optical bandgap of bulk NiO is 4.0 eV [28]. For thin films of NiO, the optical bandgap falls within the range 3.6 eV to 4.0 eV [29, 30, 31]. Generally, NiO has a direct, wide bandgap and the largest excitonic binding energy of 110 meV [32]. The optical band gap of NiO films depends on the method and details of preparation [33]. The presence of nickel defect centres which are formed either by oxidation of nickel or incorporation of dopants gives NiO a black appearance, due to the increased absorption between 1.75 eV and 2.75 eV. Optical absorption

in NiO is due to either a p$\longrightarrow$ d transition on a single nickel atom [34] or a d$\longrightarrow$ d transition between two adjacent nickel atoms [35].

Despite its low conductivity, NiO and NiO-derived materials have been used in many applications such as fuel cells, secondary ion batteries, dielectric materials, solar thermal absorbers, heterojunction solar cells [36], hole transport layers (HTL) in organic solar cells [37], cathode material in water splitting, electrochromic devices in smart windows and displays [38, 39], gas and chemical sensors [40, 41], catalysts, light and ultra-violet (UV) sensors [42, 43], light emitting diodes [44], electrode material for supercapacitors [45], electronic devices such as thin film transistors (TFT) [46], resistive switching memory and transparent conducting oxide [47].

3.4 Sensors

A sensor is any device that responds to a physical quantity and converts it to an appropriate quantity suitable for processing and measurement. Different phenomena of biological, chemical, thermal, mechanical, electrical, optical and nuclear nature can stimulate a sensor to produce an output. Since it is easy to process and manipulate electrical signals, the output of a sensor is usually limited to electrical signals such as current, charge, and voltage. For this reason, a sensor is described as a device that receives a signal or stimulus and responds with an electrical signal [48]. Sensors may be classified based on function, structure, energy form and the output signal. On the basis of energy there are eight types of sensors: chemical, optical, mechanical, electrical, thermal, magnetic, acoustic and nuclear sensors [49].

Some sensors require external sources of power for their operation and are classified as active sensors. In such sensors, the quantity to be measured is made to modulate the input electrical signal in order to produce an appropriate output which is also electrical in nature, so active sensors are also known as modulating sensors. Passive sensors are capable of generating an electrical signal when stimulated, without being powered. They convert energy in any form into electrical energy, so they are basically referred to as transducers or self-generating sensors [50]. Sensors are of importance in many areas of human endeavour, such as agriculture, military and space, health and medicine, meteorology, security and scientific research.

3.5 Photodetectors

A photodetector is a transducer that is used for converting light energy into electrical energy. Some of the applications of photodetectors include optical fibre communications, optical receivers, and imaging systems. Semiconductor-based photodetectors can be of different types or structures such as: photoconductors, junction diodes, PIN diodes, metal-semiconductor (Schottky barrier) diodes, metal-semiconductor-metal photodiodes, and avalanche photodiodes [51, 52]. In a photovoltaic mode of operation, a photodiode is operated without a bias. Carriers are generated in the diode when it is illuminated and the internal electric field across the depletion region drives current through an external load. In the photoconductive mode, a reverse bias is applied to the diode. This increases the speed of operation because the electric field across the depletion region is increased. The reverse bias is usually less than the breakdown voltage except for the avalanche photodiodes. Important characteristics of a photodetector are quantum efficiency, responsivity, speed of response and noise equivalent power [52].

3.5.1 Quantum efficiency

The quantum efficiency, QE, also known as internal quantum efficiency, η_i is the ratio of the number of generated electron-hole pairs per incident photon that are collected at the contacts. The external quantum efficiency (EQE or η), compares the collected photocurrent to the number of incident photons. The external quantum efficiency varies with the wavelength (λ) of the incident light. The quantum efficiency is given by [53]:

$$\eta = \frac{I_{ph}/q}{P_i/(h\nu)} = \frac{I_{ph}}{P_i}\frac{hc}{q\lambda} = \frac{1.24}{\lambda} \tag{3.1}$$

where I_{ph} is the primary photocurrent, P_i is the incident power, $h\nu$ is the photon energy, h is the Plancks constant, ν is the frequency of the photon, c is the speed of light in vacuum and q is the electronic charge. The depletion region must be thick enough to allow incident radiation to be adequately absorbed in order to increase the quantum efficiency [51].

3.5.2 Responsivity

The responsivity, R, is defined as the ratio of the primary photocurrent (without internal gain) to the incident optical power, it is a function of wavelength. The relationship between R and η is [53]:

$$R_\lambda = \frac{I_{ph}}{P_i} = \frac{\eta\lambda(\mu m)}{1.24} \tag{3.2}$$

The unit of R is Ampere per Watt (A/W).

3.5.3 Speed

The speed of operation of a photodetector is related to its response time. The response time is the time taken for the photo-generated current to attain 63.2% of the steady state value when the photodetector is irradiated. The speed of a photodiode depends on the drift time in the depletion region, diffusion of carriers and capacitance of the depletion region. For a fast response, the depletion region needs to be close to the surface, to allow carriers generated in the quasi-neutral region to diffuse into the depletion region, and it must be thin to reduce the transit time of carriers [51].

3.5.4 Wavelength sensitivity range

This is the range of wavelengths over which the absorption layer of the photodetector is sensitive. The cut-off wavelength of the detector depends on the bandgap energy of the absorbing layer according to the relation:

$$\lambda_c = \frac{hc}{E_g} \tag{3.3}$$

where E_g is the bandgap of the material. For λ longer than λ_c, the absorbing material is transparent [53].

3.6 Gas sensors

A gas sensor is a chemical sensor which is sensitive to chemicals in the gas phase, unlike electrochemical sensors that work in solutions. A gas sensor detects the change in the concentration of an analyte and converts the change into an electronic or electrical signal. A gas sensor performs two important functions:

(i) it recognizes a particular gas and

(ii) it produces a measurable sensing signal.

The first function called the reception function is carried out through gas-solid interactions at the surface of the sensing material. Such interactions may be in the form of adsorption or chemical reactions. The output of most gas sensors is obtained by measuring the change of current, resistance or capacitance of the sensing material. The conversion of the molecular or chemical information to an appropriate measurable electronic signal is called the transduction function. Gas sensors are generally expected to conform to a certain set of requirements or specifications in order to operate satisfactorily. Some of these requirements are sensitivity, stability, selectivity, response time, recovery time, stability, accuracy and frequency response.

3.6.1 Types of gas sensors

Different types of gas sensors such as calorimetric gas sensors [54, 55], acoustic wave gas sensors [56, 57] , optical gas sensors [58], electrochemical gas sensors [59, 60, 61, 62] and chemoresistive gas sensors work on different principles. Details about the descriptions and principles of operations can be found in the cited references. In chemoresistive gas sensors, a chemical reaction between the target gas and a sensing material results in a concentration-dependent change in the resistance of the material. The change in resistance is transformed into an appropriate electrical signal for measurement. The sensing material might be in the form of bulk, thin film or nanostructures. Materials that are normally used in chemoresistive gas sensors are semiconductor metal oxides, carbon nanotubes and conducting polymers.

3.6.2 Semiconductor metal oxide gas sensors

Semiconductor metal oxides (SMO) are oxides of transition metals. Transition elements are found in periods 4 to 8 of the periodic table, that lie between group 2 and group 3. They are also called d-block elements because they have incomplete *d*-shells. The valence electrons of these elements are found in in different orbitals, which distinguishes them from non-transition metals. Therefore, transition metals have more than one valence states. It is difficult to add or remove an electron from the cation when non-transition metals are coordinated to O^{2-} ligands because of the high amount of energy that is required. Therefore oxidation states of these metals cannot be changed easily. In transition metals, the difference in energy between d^n and d^{n+1} or d^{n-1} levels is usually small [63]. Consequently, they exist in several oxidation states. This implies that electrons can easily be added or removed from oxides of transition metals. This property makes them to be useful as gas sensors.

The moderate carrier concentration in SMOs, their bandgaps which ensure that electrons are always present in the conduction band at operating temperatures, and the fact that the surface reaction they undergo is reversible make them good candidates for gas sensing [64]. Common SMOs that have been used in gas sensing include SnO_2, WO_3 and ZnO (n-type semiconductors), and NiO, CuO and Cr_2O_3 (p-type semiconductors). The concentration of carriers in elemental and compound semiconductors such as Si, Ge, and GaAs is moderate but they are not used in gas sensing. In these materials, a layer of insulating oxide is formed on their surfaces when they are exposed to oxygen at high temperatures. The surfaces are passivated by the insulating oxide.

3.6.3 Principle of operation of semiconductor metal oxide gas sensors

The sensing mechanism of semiconductor metal oxide gas sensors (SMOGS) depends on the chemisorption of atmospheric oxygen at operating temperatures between 100 ℃ and 500 ℃. Different oxygen species are formed at different temperatures. Below 150 ℃, the molecular species O_2^- is formed, the atomic species O^- and O^{2-} dominate [65]. An oxygen molecule is

adsorbed to the surface of the SMO and takes an electron which has sufficient energy to reach the surface from the SMO, thereby forming a particular species at the prevalent temperature. The ionosorbed species resides in an unoccupied chemisorption site on the surface of the SMO. The ionosorption of the oxygen species leads to the formation of a depletion layer at the surface of an n-type SMO and an accumulation layer in a p-type SMO.

Metal vacancies in the lattice of SMOs give rise to p-type conductivity. These defects provide acceptor levels in the band structure of the SMO. At the temperature of operation, all acceptors are ionized and the number of holes in the valence band is equal to the number of ionized acceptors. The ionosorbed oxygen species at the surface of the SMO remove electrons from the valence band thereby increasing the concentration of holes. This results in upward band bending and accumulation of holes near the surface of the material, as shown Figure 3.5.

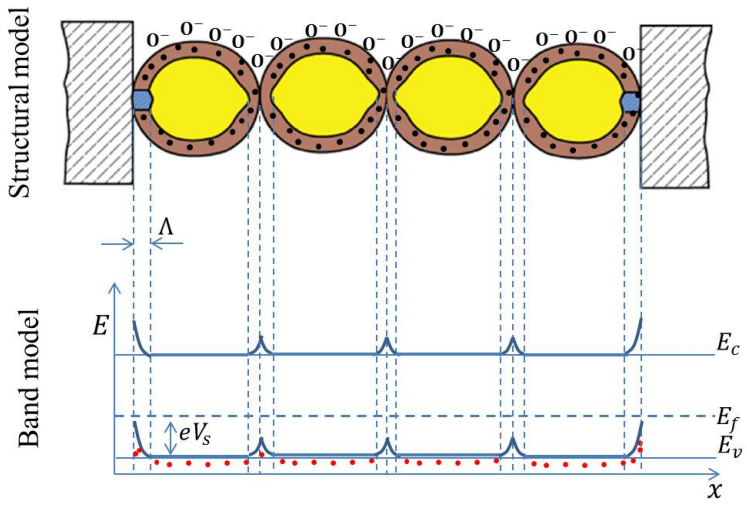

Figure 3.5: Structural and band models of a p-type semiconductor metal oxide showing a Schottky barrier between grains. Adapted from [66].

The region just below the surface of the p-type SMO is therefore richer in carriers (holes) than the bulk of the material. The average concentration of holes around the surface of the material is given as [67]:

$$p_s = p_b e^{(\frac{-qV_s}{2kT})} \tag{3.4}$$

where p_s and p_b are the concentration of holes in the surface and in the bulk of the material respectively, V_s is the surface potential of the SMO. The conductance of the material is proportional to the concentration of carriers in the accumulation region, and can be expressed as

[68, 67]:

$$G_p \propto e^{(\frac{qV_s}{2kT})} \tag{3.5}$$

3.6.4 Sensing mechanism in semiconductor metal oxides

The gas sensing mechanism in SMO is based on the change in the conductivity of the material when it is exposed to the target gas. The molecules of the target gas perform two functions during their interaction with the SMO. The molecules either donate or accept electrons from the bands in the material; this is the receptor function. The receptor function is basically a redox reaction between the ionosorbed oxygen species and the molecules of the target gas. The change in concentration of charge carriers translates to a change in the electrical property of the material. This is the transduction function. In air at the right temperature, oxygen accepts electrons from an SMO through a surface reaction shown below and it become ionized.

$$\mathrm{O_{2(g)} + e^-_{(surface)} \rightleftharpoons {O_{2(ad)}}^-} \tag{3.6}$$

$$\mathrm{O_{2(g)} + 2\,e^-_{(surface)} \rightleftharpoons 2\,{O_{(ad)}}^-} \tag{3.7}$$

or

$$\mathrm{O^-_{2(ad)} + e^-_{(surface)} \rightleftharpoons 2\,{O_{(ad)}}^-} \tag{3.8}$$

The ionic layer on the surface of the material interacts with the molecules of the target gas through the process of adsorption and desorption [69, 70].

In p-type materials, ionosorbed oxygen removes electrons from the valence band, this leads to the generation of holes in the band. The upward band bending results in the accumulation of holes in the surface region of the SMO. Molecules of reducing gases remove ionosorbed oxygen from the surface and add electrons into the valence band. This leads to a reduction in the

concentration of holes in the band as a result of recombination. Consequently, the conductivity of the material decreases. The reverse holds for the interaction of the surface of p-type SMO with molecules of oxidizing gases.

Adsorption and desorption of oxygen affect the band bending and the conductivity of the SMOs according to Equations 3.4, and 3.5. A number of factors can have an influence on the reversible interaction of the target gas with the surface of the metal oxide gas sensors. Some of these are properties of the sensing materials, such as: surface doping, the microstructure of the layer, temperature and humidity.

3.7 Principle of gas sensing

The basics of gas sensing involves the measurement of resistance, R_a, of the sensor in air or oxygen in a chamber. The target gas is introduced into the chamber and the variation in resistance of the sensor with time as the target gas is switched on and off is measured. The plot of resistance versus time is called the response curve of the sensor. The steady state resistance, R_g, of the sensor in the target gas can be determined from the curve. A typical response of a p-type SMOGS that is exposed to an oxidising gas is shown in Figure 3.6.

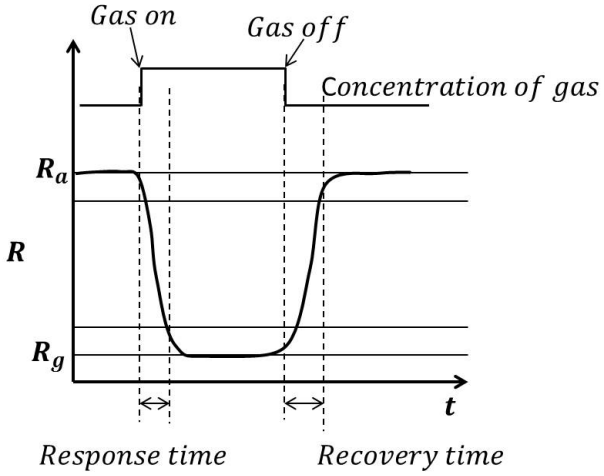

Figure 3.6: A typical response of a p-type SMO to an oxidizing gas. Redrawn from [54]

The following parameters can be obtained from the response curve: sensitivity, selectivity, speed of response and stability.

3.7.1 Sensitivity

Sensitivity is a parameter that states the ability of a sensor to detect a given concentration of the target gas. It is a measure of response of the sensor per unit change in concentration. In SMOs, sensitivity is defined in terms of resistance of the sensor in air R_a and in the target gas R_g. For the interaction of n-type (p-type) SMOs with reducing (oxidizing) gases, there is a reduction in resistance of the material. The sensitivity is expressed as:

$$S = \frac{R_a - R_g}{R_a} \tag{3.9}$$

Generally the sensitivity can be expressed as:

$$S = AP_g^{\beta} \tag{3.10}$$

where A is a factor, P_g is the partial pressure of the gas which depends on its concentration and β is a constant which is either 1 or 1/2 depending on the charge on the surface species.

3.7.2 Selectivity

Selectivity is the ability of the gas sensor to identify a specific gas in a mixture of gases. It is defined as the cross sensitivity to all other gases in the mixture and can be expressed as:

$$Q\% = \frac{100S'}{S} \tag{3.11}$$

i.e. the ratio of the sensitivity, S', of the sensor towards the target gas to the sensitivity, S, towards an interferent, expressed as a percentage.

3.7.3 Speed of response

This refers to how fast the sensor is, in its response to the change in concentration of the target gas. It is usually measured with two parameters; response time and recovery time.

Response time: This is the time required for the sensor to reach 90% of the total response (saturation value) after applying the gas in a step function.

Recovery time: Is the time the sensor requires to return to 90% of the original baseline when the gas is removed.

3.7.4 Stability

This term refers to the repeatability of the measurement results over a period of long-term testing. Factors that can affect the stability of the sensor are [71]:

(i) Contamination of the sensing surface,

(ii) Change in the sensor's properties

(iii) Change in morphology of the sensor especially thin films due to high operating temperature.

References

[1] Lambert Ben Freund and Subra Suresh. *Thin film materials: stress, defect formation and surface evolution*. Cambridge University Press, 2004.

[2] Gary Hodes. *Chemical solution deposition of semiconductor films*. CRC press, 2002.

[3] Thomas P Niesen and Mark R De Guire. Deposition of ceramic thin films at low temperatures from aqueous solutions. *Journal of Electroceramics*, 6(3):169–207, 2001.

[4] Theodor Schneller, Rainer Waser, Marija Kosec, and David Payne. *Chemical solution deposition of functional oxide thin films*. Springer, 2013.

[5] RS Mane and CD Lokhande. Chemical deposition method for metal chalcogenide thin films. *Materials Chemistry and physics*, 65(1):1–31, 2000.

[6] SR Nalage, MA Chougule, Shashwati Sen, PB Joshi, and VB Patil. Sol–gel synthesis of nickel oxide thin films and their characterization. *Thin Solid Films*, 520(15):4835–4840, 2012.

[7] Mark R De Guire, Luciana Pitta Bauermann, Harshil Parikh, and Joachim Bill. Chemical bath deposition. In *Chemical Solution Deposition of Functional Oxide Thin Films*, pages 319–339. Springer, 2013.

[8] C Jeffrey Brinker and George W Scherer. *Sol-gel science: the physics and chemistry of sol-gel processing*. Academic press, 2013.

[9] Hyun Sung Kim, Paul D Byrne, Antonio Facchetti, and Tobin J Marks. High performance solution-processed indium oxide thin-film transistors. *Journal of the American Chemical Society*, 130(38):12580–12581, 2008.

[10] Sunho Jeong and Jooho Moon. Low-temperature, solution-processed metal oxide thin film transistors. *Journal of Materials Chemistry*, 22(4):1243–1250, 2012.

[11] Masamichi Sato and Itsuo Fujii. Spin coating process, September 12 1978. US Patent 4,113,492.

[12] MD Tyona. A theoretical study on spin coating technique. *Advances in Materials Research*, 2(4):195–208, 2013.

[13] Niranjan Sahu, B Parija, and S Panigrahi. Fundamental understanding and modeling of spin coating process: A review. *Indian Journal of Physics*, 83(4):493–502, 2009.

[14] Pramod S Patil. Versatility of chemical spray pyrolysis technique. *Materials Chemistry and Physics*, 59(3):185–198, 1999.

[15] John B Mooney and Shirley B Radding. Spray pyrolysis processing. *Annual Review of Materials Science*, 12(1):81–101, 1982.

[16] Olusegun J Ilegbusi, SM Navid Khatami, and Leonid I Trakhtenberg. Spray pyrolysis deposition of single and mixed oxide thin films. *Materials Sciences and Applications*, 8(02):153, 2017.

[17] Peter Lunkenheimer, Alois Loidl, CR Ottermann, and K Bange. Correlated barrier hopping in NiO films. *Physical Review B*, 44(11):5927, 1991.

[18] Civalleri B. http://www.theochem.unito.it/crystal_tuto/mssc2008_-cd/tutorials/geometry/geom_tut.html, 2008. Accessed: 2019-08-02.

[19] A Merih Akyuzlu, Fethi Dagdelen, Ahmet Gultek, AA Hendi, and Fahrettin Yakuphanoglu. Electrical characterization of ZnO/NiO pn junction prepared by the sol-gel method. *The European Physical Journal Plus*, 132(4):178, 2017.

[20] Anas A Ahmed, Mutharasu Devarajan, and Naveed Afzal. Fabrication and characterization of high performance MSM UV photodetector based on NiO film. *Sensors and Actuators A: Physical*, 262:78–86, 2017.

[21] KK Purushothaman, S Joseph Antony, and G Muralidharan. Optical, structural and electrochromic properties of nickel oxide films produced by sol–gel technique. *Solar Energy*, 85(5):978–984, 2011.

[22] Titas Dutta, P Gupta, A Gupta, and J Narayan. Effect of Li doping in NiO thin films on its transparent and conducting properties and its application in heteroepitaxial pn junctions. *Journal of Applied Physics*, 108(8):083715, 2010.

[23] Ehssan Salah Hassan, Asrar Abdulmunem Saeed, and Abdulhussain K Elttayef. Doping and thickness variation influence on the structural and sensing properties of NiO film prepared by RF-magnetron sputtering. *Journal of Materials Science: Materials in Electronics*, 27(2):1270–1277, 2016.

[24] SC Chen, TY Kuo, SU Jen, HP Chiang, WY Liu, and CH Wang. Effect of copper content on the electrical stability of nickel oxide films. *Thin Solid Films*, 584:238–242, 2015.

[25] Suman Nandy, UN Maiti, CK Ghosh, and KK Chattopadhyay. Enhanced p-type conductivity and band gap narrowing in heavily Al doped NiO thin films deposited by RF magnetron sputtering. *Journal of Physics: Condensed Matter*, 21(11):115804, 2009.

[26] H Sato, T Minami, S Takata, and T Yamada. Transparent conducting p-type NiO thin films prepared by magnetron sputtering. *Thin solid films*, 236(1-2):27–31, 1993.

[27] Paul G Slade. *Electrical contacts: principles and applications*. CRC press, 2017.

[28] F Reinert, P Steiner, S Hüfner, H Schmitt, J Fink, M Knupfer, P Sandl, and E Bertel. Electron and hole doping in NiO. *Zeitschrift für Physik B Condensed Matter*, 97(1):83–93, 1995.

[29] Attieh A Al-Ghamdi, M Sh Abdel-wahab, AA Farghali, and PMZ Hasan. Structural, optical and photo-catalytic activity of nanocrystalline NiO thin films. *Materials Research Bulletin*, 75:71–77, 2016.

[30] Anas A Ahmed, Naveed Afzal, Mutharasu Devarajan, and Shanmugan Subramani. Structural, morphological, optical and electrical properties of NiO films prepared on Si (100) and glass substrates at different thicknesses. *Materials Research Express*, 3(11):116405, 2016.

[31] M Jlassi, I Sta, M Hajji, and H Ezzaouia. Optical and electrical properties of nickel oxide thin films synthesized by sol–gel spin coating. *Materials Science in Semiconductor Processing*, 21:7–13, 2014.

[32] Malkeshkumar Patel, Hong-Sik Kim, Joondong Kim, Ju-Hyung Yun, Sung Jin Kim, Eun Ha Choi, and Hyeong-Ho Park. Excitonic metal oxide heterojunction (NiO/ZnO) solar cells for all-transparent module integration. *Solar Energy Materials and Solar Cells*, 170:246–253, 2017.

[33] R Newman and RM Chrenko. Optical properties of nickel oxide. *Physical Review*, 114(6):1507, 1959.

[34] AR Williams, J Kübler, and K Terakura. Williams, kübler, and terakura respond. *Physical Review Letters*, 54(25):2728, 1985.

[35] R Merlin. Electronic structure of NiO. *Physical Review Letters*, 54(25):2727, 1985.

[36] Daisuke Kawade, Kazuma Moriyama, Fumika Nakamura, Shigefusa F Chichibu, and Mutsumi Sugiyama. Fabrication of visible-light transparent solar cells composed of $NiO/Ni_xZn_{1-x}O/ZnO$ heterostructures. *Physica Status Solidi (c)*, 12(6):785–788, 2015.

[37] Xiao Li Zhang, Hai Tao Dai, Jun Liang Zhao, Chen Li, Shu Guo Wang, and Xiao Wei Sun. Effects of the thickness of NiO hole transport layer on the performance of all-inorganic quantum dot light emitting diode. *Thin Solid Films*, 567:72–76, 2014.

[38] XH Xia, JP Tu, J Zhang, XH Huang, XL Wang, WK Zhang, and H Huang. Multicolor and fast electrochromism of nanoporous NiO/poly (3, 4-ethylenedioxythiophene) composite thin film. *Electrochemistry Communications*, 11(3):702–705, 2009.

[39] J Zhang, JP Tu, XH Xia, Y Qiao, and Y Lu. An all-solid-state electrochromic device based on NiO/WO_3 complementary structure and solid hybrid polyelectrolyte. *Solar Energy Materials and Solar Cells*, 93(10):1840–1845, 2009.

[40] Masahiko Matsumiya, Fabin Qiu, Woosuck Shin, Noriya Izu, Norimitsu Murayama, and Shuzo Kanzaki. Thin-film Li-doped NiO for thermoelectric hydrogen gas sensor. *Thin Solid Films*, 419(1-2):213–217, 2002.

[41] Abubakar A Khaleed, Abdulhakeem Bello, Julien K Dangbegnon, Damilola Y Momodu, MJ Madito, FU Ugbo, AA Akande, BP Dhonge, Farshad Barzegar, O Olaniyan, et al. Effect of activated carbon on the enhancement of CO sensing performance of NiO. *Journal of Alloys and Compounds*, 694:155–162, 2017.

[42] Hiromichi Ohta, Masao Kamiya, Toshio Kamiya, Masahiro Hirano, and Hideo Hosono. UV-detector based on pn-heterojunction diode composed of transparent oxide semiconductors, p-NiO/n-ZnO. *Thin Solid Films*, 445(2):317–321, 2003.

[43] Md Rezaul Hasan, Ting Xie, Sara C Barron, Guannan Liu, Nhan V Nguyen, Abhishek Motayed, Mulpuri V Rao, and Ratan Debnath. Self-powered p-NiO/n-ZnO heterojunction ultraviolet photodetectors fabricated on plastic substrates. *APL materials*, 3(10):106101, 2015.

[44] YY Xi, YF Hsu, AB Djurišić, AMC Ng, WK Chan, HL Tam, and KW Cheah. NiO/ ZnO light emitting diodes by solution-based growth. *Applied Physics Letters*, 92(11):113505, 2008.

[45] UM Patil, RR Salunkhe, KV Gurav, and CD Lokhande. Chemically deposited nanocrystalline NiO thin films for supercapacitor application. *Applied Surface Science*, 255(5):2603–2607, 2008.

[46] Ao Liu, Huihui Zhu, Zidong Guo, You Meng, Guoxia Liu, Elvira Fortunato, Rodrigo Martins, and Fukai Shan. Solution Combustion Synthesis: Low-Temperature Processing for p-Type Cu: NiO Thin Films for Transparent Electronics. *Advanced Materials*, 29(34):1701599, 2017.

[47] S Seo, MJ Lee, DH Seo, EJ Jeoung, D-S Suh, YS Joung, IK Yoo, IR Hwang, SH Kim, IS Byun, et al. Reproducible resistance switching in polycrystalline NiO films. *Applied Physics Letters*, 85(23):5655–5657, 2004.

[48] Jacob Fraden. Handbook of modern sensors: physics, designs, and applications, 2010.

[49] Joseph McGhee. Classification of Sensors. *Handbook of Measuring System Design*, 2005.

[50] Anton FP Van Putten. *Electronic measurement systems: theory and practice*. CRC Press, 1996.

[51] Simon M Sze and Kwok K Ng. *Physics of semiconductor devices*. John wiley & sons, 2006.

[52] Marius Grundmann. *The physics of semiconductors: an introduction including nanophysics and applications*. Springer, 2015.

[53] M Jamal Deen and Prasanta Kumar Basu. *Silicon photonics: fundamentals and devices*, volume 44. John Wiley & Sons, 2012.

[54] BBR John and BG Jeyaprakash. Nptel–electrical & electronics engineering–semiconductor nanodevices. *Joint Initiative of IITs and IISc*, 30, 2004.

[55] Yavuz Konak Ipek. https://www.mavili.com.tr/en/gas_sensors1/gas_sensors1/1264-gas_-sensors1.html, 2018. Accessed: 2019-08-01.

[56] Showko Shiokawa and Jun Kondoh. Surface acoustic wave sensors. *Japanese Journal of Applied Physics*, 43(5S):2799, 2004.

[57] Sarin Anakkat Koyilothu and Raju A Raghurama. SAW based CO_2 sensors using carbon nanotubes as the sensitive layer, September 11 2008. US Patent App. 11/716,215.

[58] Robert Bogue. Detecting gases with light: a review of optical gas sensor technologies. *Sensor Review*, 35(2):133–140, 2015.

[59] Matthew L Smith and Steven J Fondriest. Electrochemical gas sensor, June 8 1993. US Patent 5,217,595.

[60] William J Aston and Yat S Chan. Electrochemical gas sensor, March 7 1995. US Patent 5,395,507.

[61] Joseph R Stetter and Jing Li. Amperometric gas sensors a review. *Chemical reviews*, 108(2):352–366, 2008.

[62] Gabriel Man, Boris Stoeber, and Konrad Walus. *Detecting and Identifying Clandestine Drug Laboratories: Sensing Technology Assessment*. Canadian Police Research Centre (Centre Canadien de recherches policières), 2008.

[63] Victor E Henrich and Paul Anthony Cox. *The surface science of metal oxides*. Cambridge university press, 1996.

[64] Katharina Grossmann, Udo Weimar, and Nicolae Barsan. Semiconducting metal oxides based gas sensors. In *Semiconductors and Semimetals*, volume 88, pages 261–282. Elsevier, 2013.

[65] Nicolae Barsan, Markus Schweizer-Berberich, and Wolfgang Göpel. Fundamental and practical aspects in the design of nanoscaled SnO_2 gas sensors: a status report. *Fresenius' Journal of Analytical Chemistry*, 365(4):287–304, 1999.

[66] Hyo-Joong Kim and Jong-Heun Lee. Highly sensitive and selective gas sensors using p-type oxide semiconductors: Overview. *Sensors and Actuators B: Chemical*, 192:607–627, 2014.

[67] M Hübner, CE Simion, A Tomescu-Stănoiu, S Pokhrel, N Bârsan, and U Weimar. Influence of humidity on CO sensing with p-type CuO thick film gas sensors. *Sensors and Actuators B: Chemical*, 153(2):347–353, 2011.

[68] N Barsan, C Simion, T Heine, S Pokhrel, and U Weimar. Modeling of sensing and transduction for p-type semiconducting metal oxide based gas sensors. *Journal of electroceramics*, 25(1):11–19, 2010.

[69] George F Fine, Leon M Cavanagh, Ayo Afonja, and Russell Binions. Metal oxide semiconductor gas sensors in environmental monitoring. *Sensors*, 10(6):5469–5502, 2010.

[70] Prabakaran Shankar and John Bosco Balaguru Rayappan. Gas sensing mechanism of metal oxides: The role of ambient atmosphere, type of semiconductor and gases - A review. *Sci. Lett. J*, 4:126, 2015.

[71] Chong-Ook Park and SA Akbar. Ceramics for chemical sensing. *Journal of Materials Science*, 38(23):4611–4637, 2003.

Chapter 4

Experimental and analytical techniques

4.1 Introduction

In this chapter, all the experimental procedures that were used to produce NiO thin films and the methods of characterisation of the films are highlighted.

4.2 Experimental techniques

NiO thin films were formed using CBD, sol-gel spin coating and spray pyrolysis. The films were characterised to determine their properties. Details of experimental procedures that were followed in fabrication of the films are discussed in this section.

4.2.1 Cleaning of substrates

Substrates were cleaned before deposition to remove any oil, grease and other material on the surface that can prevent adhesion of films to them. The following cleaning procedures were followed to ensure grease-free surfaces before films were deposited on the substrates:

4.2.1.1 Glass substrates

Glass substrates, indium tin oxide (ITO) films on glass and fluorine tin oxide (FTO) films on glass, were first washed in a detergent solution to remove grease from their surfaces; they were then rinsed with de-ionized water and washed with acetone and ethanol at room temperature for 10 minutes each in an ultrasonic bath. The substrates were blown dry by nitrogen gas.

4.2.1.2 Silicon substrates

Silicon substrates were washed using trichloroethylene (TCE), isopropanol and methanol successively for five minutes in an ultrasonic bath, after which they were rinsed in deionized water and etched in a solution of 40% hydrofluoric acid for 20 seconds, and were blown dry in a stream of nitrogen gas.

4.2.2 Preparation of standard solutions for deposition

Solutions of known concentrations required for deposition of NiO films were prepared by dissolving a predetermined quantity of Ni^{2+} salts (solute) in appropriate solvents. The mass, m, of the solute to be dissolved in a given volume, vol, of the solvent to produce a solution of molarity, M, was calculated from:

$$m = \frac{M \times MM \times vol \times 100}{1000 \times pp} \tag{4.1}$$

where MM is the molar mass of the Ni^{2+} salt and pp is the percentage purity of the salt.

Doped NiO thin films were prepared by dissolving a given mass of the dopant salt in the solution of the precursor to produce certain molar percentage of the dopant in the solution. The molar percentage of the dopant in the solution was calculated as the ratio of number of moles of dopant to the total number of moles (dopant and Ni^{2+}) expressed as a percentage. The molar percentage was calculated as:

$$mol\% = \frac{[D^m] \times 100}{[D^m] + [\mathrm{Ni}^{2+}]} \tag{4.2}$$

where $[D^m]$ and $[\mathrm{Ni}^{2+}]$ are the concentrations of dopant and Ni^{2+} in mol/dm^3. The required mass of the dopant m_d was calculated from:

$$m_d = \frac{mol\%}{100} \times \frac{vol}{1000} \times M \times MM \tag{4.3}$$

where vol is the volume of precursor solution in ml, M is the molarity of the precursor solution, and MM is the molar mass of the precursor of the dopant.

4.2.3 Growth of thin films using chemical bath deposition

Chemicals that were used in the CBD method are:
Nickel sulphate ($NiSO_4.6H_2O$) as the precursor for Ni^{2+}, ammonia (NH_3) and monoethanolamine (MEA) as complexing agents and polyvinyl alcohol (PVA). A solution containing a known amount of the precursor was made in a 100 ml beaker and an appropriate quantity of the complexing agent was added to the solution and it was stirred. A water bath was made with a 500 ml beaker and the 100 ml beaker was placed in the water bath such that the level of water was higher than the level of chemical solution in the chemical bath.

One side of substrates (the non-conductive side in the case of ITO and FTO coated glass) was covered with a tape to avoid deposition of film on that side. A portion of the front side of the substrates was also covered. The substrates were held in a holder made of teflon (an inert material) and were suspended vertically and totally immersed in the chemical bath. The water in the bath was stirred gently and heated. The temperature of the water bath was monitored and controlled with a thermocouple which provided a feedback signal to the heater of the magnetic stirrer.

The temperature of the chemical bath was kept at a constant value for a given period of time during which deposition took place on the substrates. The substrates were removed, washed with de-ionized water and rinsed with ethanol. They were dried at 150 ℃ for 10 minutes and

annealed at various temperatures. A shematic diagram showing the setup for the deposition of NiO thin films using the CBD method is shown in Figure 4.1.

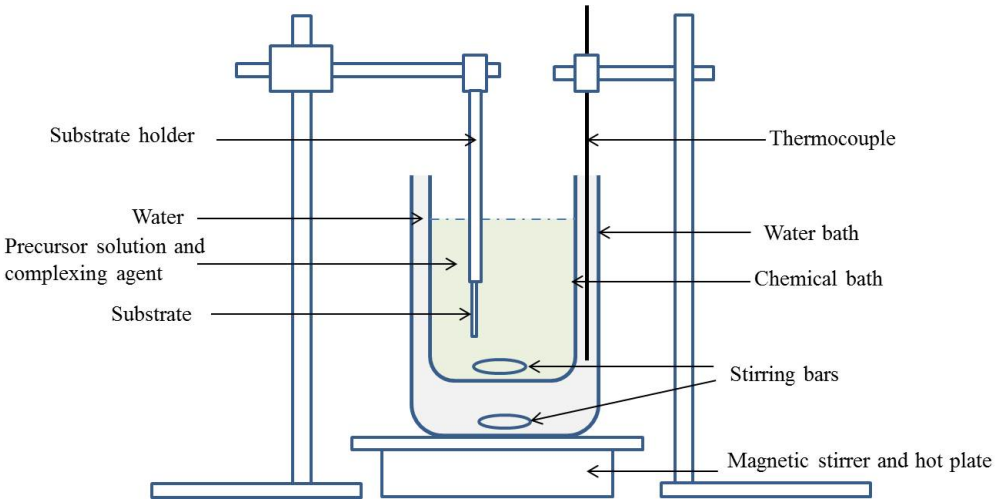

Figure 4.1: A schematic diagram showing the set-up for chemical bath deposition.

Using ammonia as the complexing agent, 5 ml of 25% ammonia was added to 0.5 M solution of $NiSO_4.6H_2O$. Deposition was carried out at temperatures of 60 ℃, 70 ℃, and 80 ℃. 70 ℃ was found to be the optimum temperature for deposition, and the time of deposition was varied from 20 minutes to 80 minutes. Annealing was done at 400 ℃ for 1 h in air.

The process was also carried out using monoethanolamine (MEA) as the complexing agent. The precursor was prepared in 1% polyvinyl alcohol (PVA) solution and 3 ml of MEA was added to the solution. Deposition was also done at 70 ℃. Films were washed, dried and annealed at 350 ℃, 400 ℃, 450 ℃, 500 ℃ and 600 ℃.

4.2.4 Growth of thin films using sol-gel spin coating

Nickel (II) acetate tetrahydrate ($Ni(CH_3COO)_2.4H_2O$) was used as the source of Ni^{2+}. The solvent was 2-methoxyethanol ($C_3H_8O_2$), and monoethanolamine (C_2H_7NO) served as the stabilizer. The precursor solution for spin coating was made by dissolving a given quantity of $Ni(CH_3COO)_2.4H_2O$ in 2-methoxyethanol ($C_3H_8O_2$) to give the required concentration of precursor (0.1 M, 0.2 M, 0.5 M, 0.7 M, and 0.75 M). MEA, (C_2H_7NO) was added to the solution as a stabilizer and the solution was stirred at 60 °C for 1 h. The molar ratio of MEA to nickel

acetate was maintained at 1:1. The solution was aged for 24 h at room temperature. The precursor solution was spin coated onto glass substrates after which the films were dried and annealed.

4.2.4.1 Optimisation of the spin coating method

Different parameters that can affect the properties of thin films in sol-gel process include: the concentration of precursor, the speed of spin coater, the number of coatings and the temperatures of drying and annealing. These parameters were varied, and morphology and structural properties of the films were observed until films of acceptable crystallinity and morphology were obtained. The concentration of the precursor was increased gradually from 0.1 M to 0.75 M. The speed of rotation of the substrate in the spin coater was changed from 1500 rpm to 3000 rpm as the concentration of solution increased because of the increase in the viscosity of the solution.

4.2.4.2 Investigation of the effects of processing temperature on the properties of sol-gel fabricated NiO thin films

The films were dried at different temperatures (160 ℃, 200 ℃, and 250 ℃) and annealed at temperatures of 300 ℃, 400 ℃, 500 ℃ and 600 ℃. Structural, microstructural, optical and electrical properties of the films were studied.

4.2.4.3 Characterisation of p-NiO Schottky diodes on p-silicon

In order to study the metal-semiconductor junction between aluminium and NiO, the precursor solution was spin coated onto p-type silicon substrates at 3500 rpm for 25 s. After each coating process, the substrates were dried at 250 °C. Spin coating and drying was repeated four times and was followed by annealing at 500 °C, for 1 h in air. Aluminium contacts (100 nm thick) were deposited by resistive evaporation on the films through a shadow mask with circular holes of 0.6 mm diameter, at a pressure of 2×10^{-6} mbar. Indium-gallium eutectic alloy was rubbed onto the silicon as an ohmic contact. The electrical properties of the diode were studied. More

details follow in section 4.3.7.

4.2.5 Growth of thin films using spray pyrolysis method

A custom-built spray pyrolysis system was used to produce thin films of nickel oxide on glass substrates. The system comprises a bottom-feed airbrush with a nozzle of diameter 0.8 mm, the precursor solution reservoir, a hot plate, a thermocouple and a bottle of high purity nitrogen gas. The spray pyrolysis system was set up in a fume chamber as shown in Figure 4.2. The precursor solution was made by dissolving nickel nitrate hexahydrate ($Ni(NO_3)_2.6H_2O$) in a mixture of ethanol and water (1:3). The room temperature solution was sprayed with the airbrush at the rate of 6 ml per minute, onto a heated glass microscope slide substrate for 5 s, from a vertical distance of 20 cm. The high purity nitrogen gas at a base pressure of 0.3 MPa served as the carrier gas.

Three different concentrations of the precursor; 0.05 M, 0.075 M and 0.1 M were used. The solution was sprayed by linearly moving the nozzle across the substrates during spraying. The temperature of the substrates changed from 300 °C to 250 °C during spraying and a period of 60 s was allowed for the substrates regain the original temperature. The spraying was repeated for 5, 10, 15 and 20 cycles with each solution. Using the 0.05 M solution, the deposition process was repeated 20 times, keeping the nozzle stationary. The films were allowed to cool to 150 °C after deposition before they were removed from the spraying chamber. They were later annealed at 500 °C for 1 h in air.

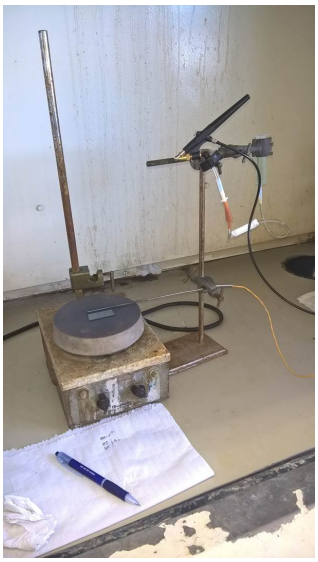

Figure 4.2: The set-up of the spray-pyrolysis system.

4.2.6 Deposition of NiO thin films on silicon substrate using spray pyrolysis

Using the spray pyrolysis method, nickel oxide thin films were deposited on silicon substrates. The parameters of deposition were varied until films were formed on the surface of the silicon wafers. For optimum quality, the temperature of the substrate was 300 °C, the rate of spraying was 2 ml/min and the pressure of the carrier gas (nitrogen) was 0.1 MPa. The distance between the nozzle and substrate was 10 cm. 0.1 M solution of the precursor was used. 75 nm thick gold was deposited on the NiO and 150 nm thick gold-antimony alloy was deposited on n-silicon, to form ohmic contacts to the device.

4.2.7 Synthesis of lithium-doped NiO thin films using spray pyrolysis

Lithium-doped NiO films were prepared by dissolving a given mass of lithium acetate in 0.1 M solution of $Ni(NO_3)_2.6H_2O$ to produce solutions with Li mole fraction of 5 mol%, 10 mol%, 15 mol% and 20 mol%. Each solution was atomized and sprayed from the nozzle onto the substrates using the conditions stated above. 30 cycles of spraying were made to fabricate each

film. The films were allowed to cool to 150 °C before they were removed from the spraying chamber. After deposition, they were annealed at 500 °C for 1 h in air and the properties of the films were examined.

4.2.8 Fabrication of a p-NiO/n-ZnO heterojunction

0.05 M zinc nitrate ($Zn(NO_3)_2.H_2O$) solution was sprayed from the nozzle onto indium tin oxide coated glass at a distance of 20 cm from the substrate. The solution was sprayed for 5 s at a rate of 6 ml/min, and the nozzle was moved across the substrate during the spraying. The temperature of the substrate varied between 180 °C and 200 °C during spraying. The spraying was done intermittently for thirty times and the film was annealed at 350 °C. Using the spraying parameters described above, 0.05 M nickel nitrate hexahydrate ($Ni(NO_3)_2.6H_2O$) solution was sprayed onto the annealed zinc oxide thin film. The temperature of the substrate varied between 250 °C and 300 °C during spraying. Hereafter, the film was annealed at 400 °C in air. Circular gold contacts, 120 nm thick, were deposited on the nickel oxide film through a shadow mask in a thermal evaporator. The diameter of circular holes in the shadow mask were 700 μm. The evaporation was done at a base pressure of 1.4×10^{-6} mbar.

The structural properties, surface morphology, and optical properties of the films were studied. The current–voltage characteristics of the devices were measured in the dark and in light. More details of the characterisation methods are given in section 4.3.

4.2.9 Annealing of samples

Annealing of samples was done in a tube furnace. Samples were placed on a piece of a silicon wafer, inside a sample holder. The holder was drawn to the centre of the tube furnace. The ends of the tube were left open when annealing was done in air. When annealing was done in a particular gas such as oxygen, nitrogen, and argon, the ends were closed and the gas was made to flow through the tube at a constant flow rate. The flow rate was controlled using a mass flow controller along the gas line and pressure valves on the gas cylinders. The annealing temperature (300 °C to 600 °C) and the ramp rate (5 °C/s to 20 °C/s) were set and the temperature inside

the furnace was monitored with a thermocouple placed under the substrate.

4.2.10 Thermal evaporation of metals for contacts to samples

Evaporation of metals for Schottky and ohmic contacts to the samples was done in an Edwards auto 306 thermal evaporator. The samples were mounted in the sample holder and they were positioned upside-down inside the evaporator. A crucible containing pellets or pieces of metal to be evaporated was positioned across power terminals in the system and a bell jar was used to cover the sample and the crucible, thereby forming the evaporating chamber. The evaporating chamber was pumped down to a pressure of about $1\times\ 10^{-6}$ mbar and a current was passed through the crucible. The metal melts and it evaporates. The deposition was done on the substrates which were mounted above the crucible. The rate of deposition (0.1 nm/s to 0.2 nm/s) was monitored with a crystal microbalance. When the desired thickness of the metal was deposited, the current was switched off and the bell jar was allowed to cool down. The system was vented, and then the samples were removed.

4.3 Analytical techniques

The following analytical techniques were used to study different properties of thin films of nickel oxide that were synthesized.

4.3.1 Scanning electron microscopy (SEM)

A scanning electron microscope (SEM) was used to examine the microscopic structures of samples. The SEM scans the surfaces of materials using a focused electron beam to provide images of the surfaces. In this work, a field emission scanning electron microscope (FESEM) ZEISS Crossbeam 540 was used to capture the micrographs of the films. Electrons were accelerated at 1 kV and the secondary electrons (SE) that were generated from the sample were detected by an in-lens detector.

4.3.2 Scanning probe microscopy (SPM)

In scanning probe microscopy (SPM), the near-field forces between atoms of the tip or apex of the probe and a surface of samples were used to study their surface topography. A Bruker Dimension Icon scanning probe microscope with ScanAsyst mode was used to examine the topography of the films. The instrument was operated in the ScanAsyst mode.

4.3.3 X-ray diffraction (XRD)

X-ray diffraction (XRD) is a non-destructive method for determining the crystal structure of materials. In this work, the structural properties of the films were studied with
(i) An XPERT-PRO diffractometer with Co Kα radiation (λ = 0.178897 nm) with an accelerating potential of 35 kV and 50 mA current (PANalytical BV, Netherlands).
(ii) A Rigaku Smartlab X-ray diffractometer (XRD) using Cu Kα radiation (λ = 0.15409 nm) with an accelerating potential of 45 kV and current of 200 mA.
(iii) A Bruker D2 PHASER X-ray diffractometer with a Cu Kα radiation (λ=0.15418 nm), with an accelerating potential of 30 kV and current of 10 mA.
The diffraction pattern was obtained in the range of 2θ from 5 ° to 89.9 °

In the diffractometers, a collimated beam of X-rays was incident on a the sample at an angle θ and the beam was diffracted by the crystallographic planes. According to Bragg's law [1]:

$$2d\sin\theta = n\lambda \tag{4.4}$$

where n is an integer indicating the order of diffraction, λ is the wavelength of the incident X-rays and d is the interplanar distance. The intensity of the diffracted beam as a function of the angle, 2θ, between the incident and diffracted beam were measured.

The diffraction pattern, a graph of intensity of diffracted beam versus 2θ, angle of diffraction, was obtained. Identification of the samples was done by comparing the diffraction pattern to a database of known patterns called the Joint Committee on Powder Diffraction Standards (JCPDS) file.

Since NiO has a simple cubic structure, the lattice constant, a, was calculated from:

$$a = d_{hkl}\sqrt{h^2 + k^2 + l^2} \tag{4.5}$$

where (hkl) refers to the Miller indices of a particular crystallographic plane. The crystallite size was calculated from the full-width at half-maximum (FWHM) of the diffraction peak using the Scherrer formula:

$$D = \frac{K\lambda}{\beta\cos\theta} \tag{4.6}$$

where β is the FWHM of the diffraction peak, K is a constant normally taken as 0.9 [2]. The preferred orientation of samples was determined from the texture coefficient (TC) as: [3]

$$TC = \frac{I_{hkl}/I_{0hkl}}{1/N\sum_1^N I_{hkl}/I_{0hkl}} \tag{4.7}$$

where I_{hkl} is the intensity of a peak in a particular (hkl) plane, I_{0hkl} is intensity of the corresponding peak in the standard and N is the number of diffraction peaks.

4.3.4 Spectrophotometry

Optical transmittance and absorbance spectra of the film were obtained in the ultraviolet (UV) and visible region in the wavelength range 200 - 800 nm using a CARY 100 BIO UV–vis spectrophotometer. According to the laws of absorption, 'the degradation in intensity of light at a particular distance of penetration in a sample is proportional to the remaining intensity at the point'[4]. If the intensity of the incident radiation is I_o and the intensity of the radiation at a depth, x, in a material is $I(x)$, the relationship between these intensities is:

$$I(x) = I_o e^{-\alpha x} \tag{4.8}$$

where α is the absorption coefficient of the material. The ratio of the radiant power of transmitted light $P_\lambda(x)$ to the incident power $P_\lambda(0)$ is the transmittance, T, of the material [5].

From equation 4.8,

$$\alpha = \frac{1}{x} \ln \frac{1}{T} \tag{4.9}$$

since intensity is proportional to the radiant power [6].

The optical bandgap E_g of the sample was determined from the Tauc plot, using the absorbance data according to Tauc *et al.* [7].

4.3.5 Raman spectroscopy

When a material is irradiated with a monochromatic light, most of the incident radiation is transmitted. A fraction of the radiation is scattered. The scattering is caused by molecules in the material that absorb energy from the incident radiation and were excited to a virtual higher energy states, they lose the acquired energy and emit radiations as they leave the excited state. In Rayleigh scattering, the frequency of the scattered radiation is equal to the frequency of the incident radiation, i.e. the molecules return to the same energy level from which they are excited. Raman scattering occurs when the frequency of the scattered radiation is different from that of the incident light. This is caused by molecules that return to an energy level that is different from the one from which they are excited. In Stokes scattering, the frequency of the scattered light is less than the incident frequency because the molecules return to a higher energy state than the ground state. In the anti-Stokes scattering, the frequency of the scattered light is higher than the frequency of the incident light[8].

The difference between the frequency of the Rayleigh scattered light and the weaker Raman scattered light, called the Raman shift, correspond to the vibrational frequencies of molecules in the material. In this work, Raman spectrum of NiO thin films were obtained using
(i) A Jobin Yvon, Horiba TX64000 and
(ii) A WITec alpha300 RAS+ confocal Raman microscope.

In these equipment, a monochromatic light from a laser source was used to irradiate the sample, the scattered laser energy was collected and a filter was used to remove the Rayleigh and anti-Stokes scattered light. The Stokes scattered light was sent to a spectrometer and a detector,

a charge-coupled device (CCD), was used to capture the light. The Raman spectrum was obtained as the graph of the intensity of the Stokes scattered light versus Raman shift.

4.3.6 Thermogravimetric analysis

Thermogravimetric analysis (TGA) is an analytical technique that measures a change in mass of a sample as a function of its temperature. It is used mainly to study decomposition and thermal stability of materials as temperature changes. The change in mass of the sample is measured as a function of temperature in the scanning mode. In the isothermal mode, the change in mass is measured as a function of time [9]. In this work, TGA was done using the SDT Q600 V20.9 Build 20 Thermal gravimetric and differential thermal analyzer (TGA-DTA) Universal V4.7A TA Instrument, in the scanning mode. The temperature was ramped from room temperature to 1000 ℃ at 10 ℃/min in nitrogen, the flow rate of nitrogen was 50 ml/min.

4.3.7 Electrical characterisation

The electrical properties of samples were measured using the linear four-point probe, current–voltage (I–V) and capacitance–voltage (C–V) measurement systems, and Hall voltage measurement system.

(a) Linear four-point probe measurement

The linear four-point probe system consists of four collinear and equally spaced electrodes, that make contact with the surface of the sample. An electric current was made to flow into and out of the sample through outer electrodes, and the voltage that developed across the inner electrodes was measured. The relationship between the electric field, E, current density, J, and resistivity, ρ, permits the derivation of the voltage, V, at a distance, r, from the electrode through which current flows into the sample as [10]:

$$V = \frac{I\rho}{2\pi r} \tag{4.10}$$

where I is the current flowing in the electrode. For a semi-infinite geometry, the potential difference across the two inner electrodes is:

$$V = \frac{I\rho}{2\pi}(\frac{1}{s}) \tag{4.11}$$

where s is the spacing between the electrodes.

The expression for the resistivity derived from Equation 4.11 has to be corrected for finite geometries, therefore, a correction factor F is inserted and the resistivity can be expressed as:

$$\rho = 2\pi s F \frac{V}{I} \tag{4.12}$$

F depends on the location of the probes relative to the edge of the sample, thickness and geometry of the sample. For thin samples in which the thickness is less than or equal to half of the electrode spacing ($t \leq \frac{s}{2}$),

$$\rho = \frac{\pi}{\ln(2)} t \frac{V}{I} = 4.532 t \frac{V}{I} \tag{4.13}$$

ρ is proportional to the thickness of the sample and the ratio of V to I. The average value of the ratio is obtained from the slope of the voltage–current graph [11]. The sheet resistance is given as the ratio of the resistivity to the thickness of the sample. The sheet resistance can therefore be expressed as:

$$R_s = \frac{\rho}{t} = \frac{\pi}{\ln(2)} \frac{V}{I} = 4.532 \frac{V}{I} \tag{4.14}$$

A Signatone Four-Point Resistivity System was used to measure the resistivity in this work. The system was used together with an HP 3245A universal source that generates an increasing stepwise current and an Agilent 34970A data acquisition/switch unit. The equipment is controlled with a Labview computer program.

(b) Current–voltage (I–V) and capacitance–voltage (C–V) characterization

The current–voltage measurements were done using an HP 4140 B pA meter/DC voltage source. It generates a stepwise voltage which was applied across the sample, the current flowing in the circuit was measured for each voltage. The system is capable of measuring current as low as 10^{-14} A. The capacitance–voltage characteristics were measured using an HP 4192A LF Impedance Analyzer. These instruments were controlled with a Labview computer program. The characteristics were also plotted during measurement for visual assessment. The I–V and C–V measurements were done in the dark inside a Faraday cage to prevent any unintentional influence on the devices.

The I–V characteristics were also measured both in light and in the dark for comparison using a solar simulator system that comprises an Oriel LCS-100^{TM} Model 94011A-ES, a Keysight B2912A precision source/measure unit and an Agilent 34972A LXI data aquisition unit. The solar simulator produces 1.0 W/cm^2 light from 100 W Xenon lamp and it has an AM1.5G spectral correction filter.

(c) Hall coefficient measurement

The measurement of Hall coefficient of a material is of importance because it allows the type of conductivity of the material to be determined. Information concerning the carrier density, and mobility of carriers can also be obtained from the measurement. The Hall voltage measurement system comprises the HP 3245A universal source, an Agilent 34970A data acquisition/switch unit, a cryostat with a Lakeshore 332 temperature controller. The magnetic field was provided by an electromagnet, the direction of the field was controlled electronically by reversing the direction of current flowing in the coils.

The method used to determine the Hall coefficient in the system is the Van der Pauw method [12]. With a positive magnetic field B, current is applied between opposite contacts (1 and 3) on the sample in the forward and reverse direction as shown in Figure 4.3, the voltages between the other contacts were measured as $V_{24,B+}$ and $V_{42,B+}$ respectively. Then the current is applied between contacts 2 and 4, voltage between terminals 1 and 3 are measured for current in both

directions as $V_{13,B+}$ and $V_{31,B+}$ respectively. The magnetic field is reversed and the whole measurement is repeated to obtain voltages $V_{24,B-}$, $V_{42,B-}$, $V_{13,B-}$ and $V_{31,B-}$.

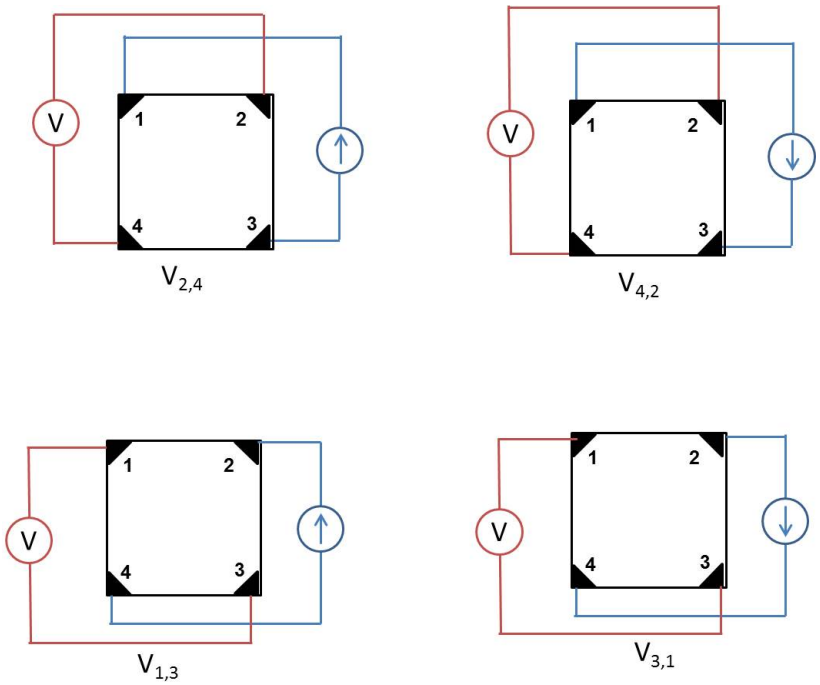

Figure 4.3: A typical configuration for measuring Hall voltage.

The Hall coefficients are calculated as:

$$R_{H1} = \frac{V_{42,B+} - V_{24,B+} + V_{24,B-} - V_{42,B-}}{4BI} \tag{4.15}$$

$$R_{H2} = \frac{V_{31,B+} - V_{13,B+} + V_{13,B-} - V_{31,B-}}{4BI} \tag{4.16}$$

where I in amperes, is the current that flows through the sample. The average Hall coefficient can be determined as [13]:

$$R_H = \frac{R_{H1} + R_{H2}}{2} \tag{4.17}$$

The system generates a predetermined current, I, and the corresponding voltage was measured. The Hall coefficient was calculated according to Equations 4.15, 4.16 and 4.17 [12].

The system also applied the electric current, I, across one edge of the sample and measuring the voltage drop across the other opposite edge as shown in Figure 4.4. Eight measurements were made by the system.

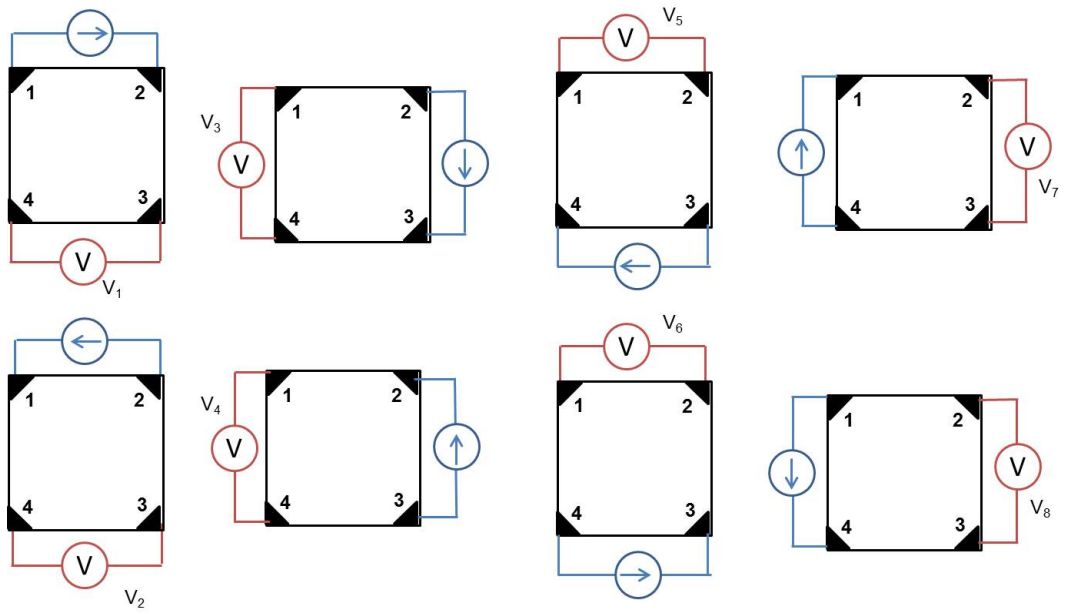

Figure 4.4: A typical configuration for determination of resistivity of a sample using Hall voltage measurement.

If the voltages were identified as $V_1, V_2 ... V_8$, the resistivity of the material can be calculated as:

$$\rho_A = \frac{\pi}{\ln 2} f_A t \frac{V_1 - V_2 + V_3 - V_4}{4I} \tag{4.18}$$

$$\rho_B = \frac{\pi}{\ln 2} f_B t \frac{V_5 - V_6 + V_7 - V_8}{4I} \tag{4.19}$$

where t is the thickness of the sample in centimetres, f_A and f_B are geometrical factors [13].

The resistance ratios can be calculated from the measured voltages as:

$$Q_A = \frac{V_1 - V_2}{V_3 - V_4} \tag{4.20}$$

$$Q_B = \frac{V_5 - V_6}{V_7 - V_8} \tag{4.21}$$

The resistance ratio and f are related as:

$$\frac{Q-1}{Q+1} = \frac{f}{0.693} \cosh^{-1}\left(\frac{e^{\frac{0.693}{f}}}{2}\right) \tag{4.22}$$

The value of f can be obtained from the plot of f versus Q as shown in Figure 4.5 [14]:

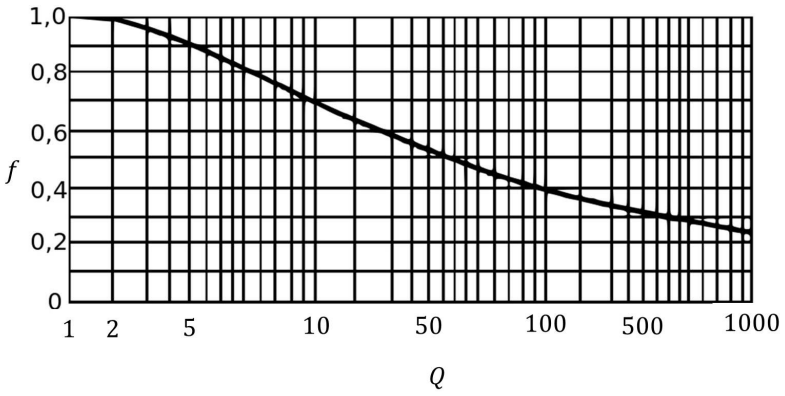

Figure 4.5: A graph of f versus Q adapted from [14].

The resistivity, ρ, of the films was determined and the mobility of carriers was calculated according to Equation 2.13.

References

[1] Lawrence Bragg. X-ray crystallography. *Scientific American*, 219(1):58–74, 1968.

[2] Ahmad Monshi, Mohammad Reza Foroughi, and Mohammad Reza Monshi. Modified Scherrer equation to estimate more accurately nano-crystallite size using XRD. *World Journal of Nano Science and Engineering*, 2(3):154–160, 2012.

[3] GG Valle, Peter Hammer, Sandra Helena Pulcinelli, and Celso Valentim Santilli. Transparent and conductive ZnO: Al thin films prepared by sol-gel dip-coating. *Journal of the European Ceramic Society*, 24(6):1009–1013, 2004.

[4] Ben G Streetman and Sanjay Kumar Banerjee. *Solid State Electronic Devices: Global Edition*. Pearson education, 2016.

[5] JW Verhoeven. Glossary of terms used in photochemistry (iupac recommendations 1996). *Pure and Applied Chemistry*, 68(12):2223–2286, 1996.

[6] Edward F Zalewski. Radiometry and photometry. *Handbook of Optics*, 2:24–1, 1995.

[7] J Tauc, Radu Grigorovici, and Anina Vancu. Optical properties and electronic structure of amorphous germanium. *physica status solidi (b)*, 15(2):627–637, 1966.

[8] Peter Larkin. *Infrared and Raman spectroscopy: principles and spectral interpretation*. Elsevier, 2017.

[9] R Bruce Prime, Harvey E Bair, Sergey Vyazovkin, Patrick K Gallagher, and Alan Riga. Thermogravimetric analysis (tga). *Thermal analysis of polymers: Fundamentals and applications*, pages 241–317, 2009.

[10] Andrew P Schuetze, Wayne Lewis, Chris Brown, and Wilhelmus J Geerts. A laboratory on the four-point probe technique. *American Journal of Physics*, 72(2):149–153, 2004.

[11] Dieter K Schroder. *Semiconductor material and device characterization*. John Wiley & Sons, 2006.

[12] O Philips'Gloeilampenfabrieken. A method of measuring specific resistivity and Hall effect of discs of arbitrary shape. *Philips Res. Rep*, 13(1):1–9, 1958.

[13] Mary A Tupta. van der Pauw and Hall voltage measurements with a parameter analyzer. https://electroiq.com/2016/10/van-der-pauw-and-hall-voltage-measurements-with-a-parameter-analyzer/, 2016.

[14] https://www.wikiwand.com/en/Van_der_Pauw_method, 2018. Accessed: 2019-09-25.

Chapter 5

Results: Deposition of NiO thin films using chemical bath deposition

5.1 Introduction

The chemical bath deposition (CBD) method is a low-cost, low-temperature method for making thin films of NiO on substrates. Nickel salts are normally used as precursors, a suitable base that can form a complex with Ni^{2+} is used as a complexing agent or ligand. When the complex dissociates, Ni^{2+} ions are released into the solution which usually contains excess OH^{-} ions. The reaction between these ions leads to the formation of a thin film on any surface that is in contact with the solution. The temperature of deposition affects the rate of dissociation of the complex and consequently, the rate of formation of the films is affected. Therefore, the choice of the temperature of deposition in CBD, depends largely on the precursor and other reagents that are used in the bath.

In this study the chemical bath deposition method was used to deposit thin films of NiO on glass substrates, using nickel (II) sulphate hexahydrate as a precursor of Ni^{2+} ions. Ammonia was initially used as a complexing agent, some parameters of deposition such time of deposition and temperature were varied. The effect of these parameters on the morphology of the films were investigated. Later monoethanolamine (MEA) was used as the complexing agent. The

effect of substrate orientation in the bath and annealing on the properties of the films were investigated.

5.2 Deposition of NiO in a chemical bath using ammonia as the complexing agent

The morphologies of the films that were produced at 60 ℃ for different time of deposition are shown in Figure 5.1. The films have porous morphology and consisted of interlocking nanowalls. Time of deposition had no effect on the morphologies. At temperatures of 70 ℃ and 80 ℃, the rate of decomposition of the complex (ammonia) was high and there was rapid precipitation in the bath. This led to formation of films with poor adhesion to the substrates. Since the films lifted off the substrates, no further analysis was done on them.

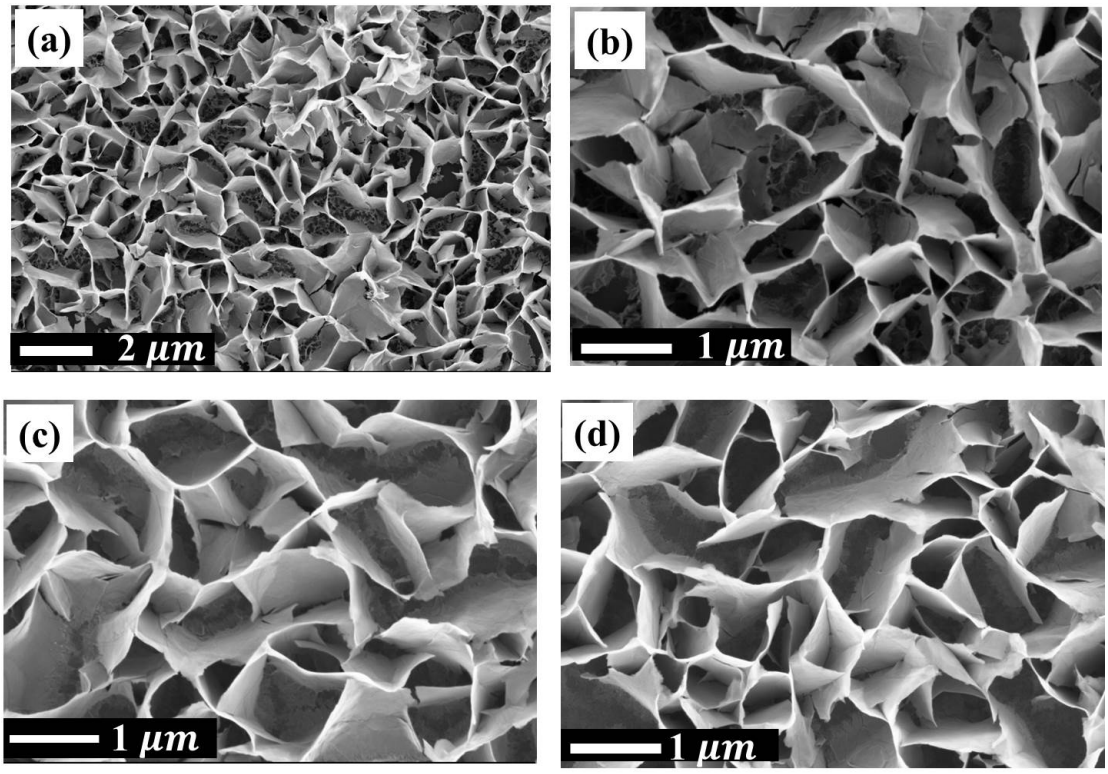

Figure 5.1: SEM images of NiO thin films deposited for (a) 20 min (b) 40 min (c) 60 min, and (d) 80 min, using ammonia as a complexing agent.

5.3 Deposition of NiO in a chemical bath using monoethanolamine (MEA) as the complexing agent

In the chemical bath, MEA formed a complex with Ni^{2+} ions, causing the blue colour of the solution. The pH of the bath immediately after composition was 11.5, this was an indication that virtually all Ni^{2+} ions were captured by the ligand. As the solution was heated, the complex released Ni^{2+} into the solution. In the presence of numerous OH^- ions from water, at 70 ℃, the nickel ions reacted with hydroxyl ions to form hydrated nickel hydroxide on the surface of the substrate. The precipitates of the hydroxide were also formed in the solution. The pH of the solution after deposition was found to be 11.32. Since the deposition of a metal oxide was expected to take place in an alkaline medium, the pH of the solution after deposition was an indication that monoethanolamine provided the ideal pH for deposition to take place in the bath. Nickel oxide thin films may be formed according to the following chemical equations:

$$NiSO_4 \cdot 6\,H_2O + 3\,MEA \rightleftharpoons [Ni(MEA)_3]SO_4 + 6\,H_2O \tag{5.1}$$

$$[Ni(MEA)_3]^{2+} + 6\,H_2O \xrightarrow[70\,^\circ C]{\Delta} Ni(OH)_2 \cdot 4\,H_2O\downarrow + 3\,MEA + 2\,H^+ \tag{5.2}$$

$$Ni(OH)_2 \cdot 4\,H_2O \xrightarrow[450\,^\circ C]{\Delta} NiO + 5\,H_2O \tag{5.3}$$

The structural, optical and electrical properties of the films deposited using the chemical bath deposition method are presented in the paper titled: Structural, optical and electrical characteristics of nickel oxide thin films synthesised through chemical processing method.

Physica B 535 (2018) 24–28

Contents lists available at ScienceDirect

Physica B

journal homepage: www.elsevier.com/locate/physb

Structural, optical and electrical characteristics of nickel oxide thin films synthesised through chemical processing method

Shadrach Akinkuade*, Benanrd Mwankemwa, Jacqueline Nel, Walter Meyer

Physics Department, University of Pretoria, Pretoria 0002, South Africa

ARTICLE INFO

Keywords:
Chemical deposition
NiO
Thin film
Polycrystalline
Optical band gap
Electrical resistivity

ABSTRACT

A simple and cheap chemical deposition method was used to produce a nickel oxide (NiO) thin film on glass substrates from a solution that contained Ni^{2+} and monoethanolamine. Thermal treatment of the film at temperatures above 350 °C for 1 h caused decomposition of the nickel hydroxide into nickel oxide. Structural, optical and electrical properties of the film were studied using X-ray diffraction (XRD), spectrophotometry, current-voltage measurements and scanning electron microscopy (SEM). The film was found to be polycrystalline with interplanar spacing of 0.241 nm, 0.208 nm and 0.148 nm for (111), (200) and (220) planes respectively, the lattice constant a was found to be 0.417 nm. The film had a porous surface morphology, formed from a network of nanowalls of average thickness of 66.67 nm and 52.00 nm for as-deposited and annealed films respectively. Transmittance of visible light by the as-deposited film was higher and the absorption edge of the film blue-shifted after annealing. The optical band gap of the annealed film was 3.8 eV. Electrical resistivity of the film was 378 Ωm.

1. Introduction

Transparent conductive oxides (TCO) such as indium tin oxide (ITO) and zinc oxide are wide bandgap semiconductors; and have been used in many applications such as transparent electrodes, solar cells and touch panels [1]. Nanostructures of various metal oxides have been investigated for hydrogen production [2] and gas sensing. Many of these TCOs which have been studied extensively are n-type semiconductors [3]. In some applications where n-type semiconductors are used, p-type semiconductors are also required to produce complementary devices or for the fabrication of p-n junctions, which are essential for the study of electrical properties and defects in n-type materials like zinc oxide [4], and to enhance the gas sensing properties of metal oxide sensors. Since it is difficult to achieve p-type conductivity by doping in n-type metal oxide semiconductors, research efforts are focused on p-type materials such as nickel oxide. Nickel oxide (NiO) is one of the few metal oxides with p-type properties; it has a stable, wide bandgap of 3.5–4.0 eV [5,6], it has been used in electrochromic [7], photoelectrochemical water splitting [8], gas sensing [9] and energy storage [10] applications. It has been reported as having an excellent chemical stability, high optical transparency and electrical conductivity. Different deposition methods such as pulsed laser deposition, dip coating, spin coating, sputtering, spray pyrolysis and chemical bath deposition (CBD) have been used to deposit thin films of nickel oxide. All these methods offer different advantages depending on the specific application of interest [11]. Among the methods, chemical bath deposition has been adjudged to be advantageous due to its relative simplicity, low cost, low temperature, scalability and good control over the deposition process [12]. According to our knowledge, there is no report on electrical characterisation of porous thin films of nickel oxide. In this work, thin films of NiO were produced by the simple and economical chemical bath deposition method. The films were characterized by scanning electron microscopy (SEM), atomic force microscopy, X-ray diffraction (XRD), UV–vis spectrophotometry and I-V/C-V measurements.

2. Experimental

2.1. Preparation of NiO thin film

All chemicals were of analytical reagent grade and used without further purification. The substrates were microscope slides cut into 25 mm by 10 mm and ITO coated glass. Prior to deposition, substrates were first soaked in warm detergent solution for 5 min, rubbed to remove any grease and rinsed in de-ionized water. They were later washed in an ultrasonic bath at 30 °C for 10 min each in de-ionized water, acetone and ethanol and then blow-dried using nitrogen gas. One side of each substrate was covered with tape to avoid deposition on

* Corresponding author.
E-mail address: u14302552@tuks.co.za (S. Akinkuade).

http://dx.doi.org/10.1016/j.physb.2017.06.021
Received 21 April 2017; Received in revised form 5 June 2017; Accepted 6 June 2017
Available online 07 June 2017
0921-4526/

both sides. The chemical bath was formed by adding 0.4g of polyvinyl alcohol (PVA) into 40 ml of de-ionized water; the solution was stirred at 250 rpm and heated gently to 90 °C. The temperature of the solution was allowed to fall to 30 °C and 0.5257g of nickel sulphate hexahydrate ($NiSO_4{\cdot}6H_2O$) was added to the solution and stirred until it dissolved completely, whereafter 3 ml of monoethanolamine (MEA) was added to form a deep blue solution. The pH of the bath taken before deposition was found to be 11.50. Substrates were vertically immersed in the bath which was heated gently. Formation of green precipitates commenced at 60 °C. The bath was maintained at 70 °C for 1 h while deposition occurred. After 1 h the solution became green and turbid. Substrates were removed, washed with de-ionized water and dried in an oven at 150 °C for 10 min. The pH of the bath after deposition was 11.32. Precipitates formed in the chemical bath were filtered, washed four times in de-ionized water and dried in an oven at 100 °C for 10 min and subjected to thermogravimetric analysis (TGA) which was carried out from 17 °C to 1000 °C in Nitrogen at a flow rate of 50.0 ml/min. Films were annealed at different temperatures, between 350 °C, and 500 °C for one hour in air. Aluminium contacts of diameter 0.6 mm and thickness 300 nm were resistively evaporated on the film that was deposited on ITO/glass substrates, after annealing.

2.2. Analysis and characterisation of the film

Microstructures of the nickel oxide film were investigated using XRD with Co Kα radiation. For the morphological analysis, field emission scanning electron microscopy (FESEM) in a ZEISS Crossbeam 540 at 1 kV acceleration voltage was used. A Jobin Yvon, Horiba© TX64000 was used for Raman studies. Optical transmittance and absorbance spectra of the film were obtained in the ultraviolet (UV) and visible region in the wavelength range 200–800 nm using a CARY 100 BIO UV–vis spectrophotometer. The electrical properties of the film between −2 V and 2 V at room temperature and in the dark were measured using I-V measurements with a HP 4140 B pA meter/DC voltage source.

3. Results and discussion

Formation of nickel oxide thin film may be described by the following chemical equations:

$$NiSO_4.\ 6H_2O + 3MEA \leftrightarrow NiSO_4.3MEA + 6H_2O \quad (1)$$

$$[Ni(MEA)_3]^{2+} + 6H_2O \xrightarrow[\Delta at 70°C]{} Ni(OH)_2.\ 4H_2O\downarrow + 3MEA + 2H^+ \quad (2)$$

$$Ni(OH)_2.\ 4H_2O \xrightarrow[\Delta at 450°C]{} NiO + 5H_2O \quad (3)$$

The first equation involves the formation of a deep blue complex of nickel and monoethanolamine, which had a pH of 11.50. When heated, the complex releases Ni^{2+} which in the presence of water at 70 °C, forms hydrated nickel hydroxide on the substrate according to Eq. (2). The pH of the solution after deposition was found to be 11.32, thus monoethanolamine provides the ideal pH for deposition of NiO in CBD. According to the TGA results shown in Fig. 1, weight loss in the precipitates occurred in three steps: The first weight loss of 5.67% took place from 50 °C to 200 °C, this can be attributed to evaporation of water of crystallization. The second and major weight loss (16.36%) in the range 200 °C to 600 °C, centred on 350 °C is due to thermal decomposition of nickel hydroxide to form nickel oxide according to Eq. (3). Weight loss at temperatures above 600 °C (5.07%) was insignificant. Colour of the film changed from green to grey after thermal treatment as shown in the inset of Fig. 1.

The XRD pattern of the film, indexed to JCPDS file No. 04–0835 [13,14], is shown in Fig. 2. Three peaks at 43.57°, 50.99° and 74.61° which were assigned to (111), (200) and (220) peaks of cubic NiO can be seen in the films annealed at 350 °C and 500 °C. The interplanar spacing d_{hkl} can be calculated from Bragg's law as:

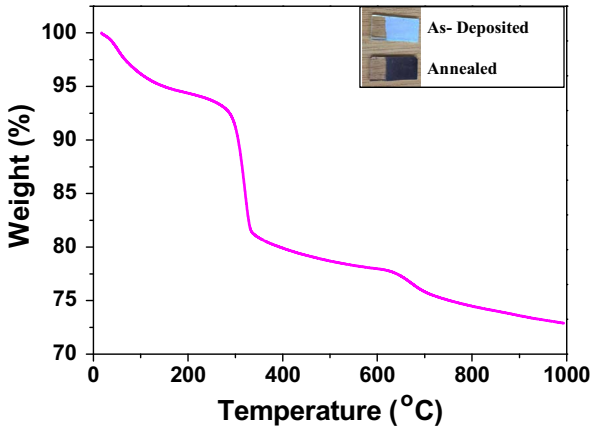

Fig. 1. Thermogravimetric curve of the NiO thin film. The inset is the photograph of the as-deposited and annealed film.

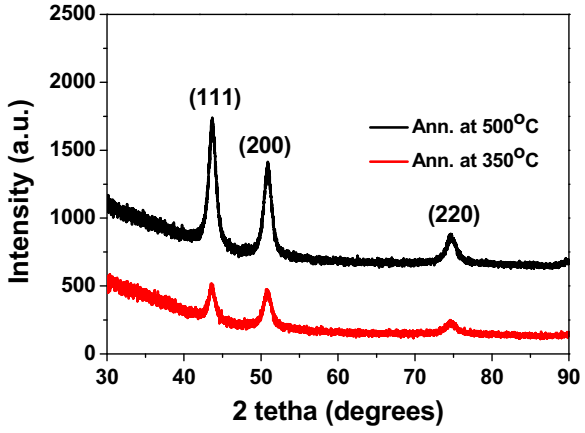

Fig. 2. X-ray diffraction (XRD) patterns of the annealed film.

$$d_{hkl} = \frac{\lambda}{2\sin\theta} \quad (4)$$

where λ, the wavelength of Co Kα radiation is 1.788965 nm and θ is the incident angle at which maximum diffraction occurs. The lattice constant a was calculated from [14]:

$$a = d_{hkl}\sqrt{(h^2 + k^2 + l^2)} \quad (5)$$

Calculated interplanar spacing and lattice constants are shown in Table 1. The d-spacing and lattice constants were very close to values obtained by [3,8,13–15].

Morphologies of the as-deposited and annealed films are shown in Fig. 3; there was no remarkable difference between these morphologies. The morphology which is porous with many interconnected nanowalls that grow vertically on the substrate forming a honeycomb like structure does not agree with the cubic structure of NiO. However, they are similar to what have been reported by [11,16]. The thickness of the nanowalls as measured at indicated points in Fig. 3a and b varied between 66.67 nm and 116 nm in the as-deposited film, with an average of 76.67 nm. After annealing the films at 450 °C, the thickness

Table 1
Information from XRD of the annealed film.

(*hkl*)	JCPDS no. 04-0835 [14]	Calculated for the NiO thin film	
	d (nm)	*d* (nm)	lattice constant *a* (nm)
111	0.2410	0.2410	0.4175
200	0.2088	0.2078	0.4156
220	0.1476	0.1477	0.4177

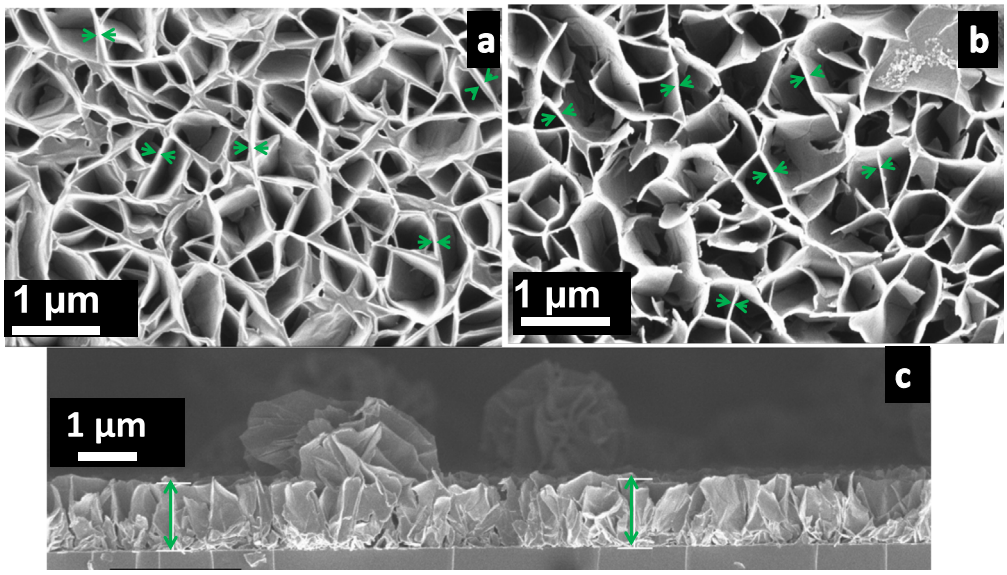

Fig. 3. SEM micrographs of NiO thin film (a) as-deposited (b) annealed and (c) cross-sectional image of annealed film.

varied between 33.33 nm and 58.33 nm with an average of 52.00 nm. Average thickness of the film on glass, as shown in Fig. 3c was 1 μm.

Raman spectra of the as-deposited and annealed films between 200 and 2000 cm^{-1} are shown in Fig. 4. Raman shifts at 560 cm^{-1} and 1100 cm^{-1} corresponding to one-phonon (1P) LO and two-phonon (2P) LO of vibrational origin similar to what was reported by [17] are seen in the spectra of the annealed film.

Fig. 5 shows the optical transmittance spectra of the annealed film. Transmittance in the visible range (380–750 nm) varied from 8.54% to 54.28% for the as-deposited film and 6.67–49.76% for the annealed film. In the ultraviolet range transmittance decreased; at 325 nm it was 2.27% and 1.21% for the as-deposited and the annealed film respectively. This corresponds with an absorption peak of NiO thin film at 320 nm reported in [18]. The recorded low value of transmittance in the visible range may be due to scattering of light from the interconnected walls in the morphology.

The relation between the absorption coefficient (α) and incident photon energy ($h\nu$) can be expressed as [19]:

$$(\alpha h\nu) = A(h\nu - E_g)^n \quad (6)$$

where A is a constant, E_g is the optical band gap of the material and n is a number which depends on the type of transition involved. For a transition of an electron from the valence to the conduction band of the material, a direct allowed, an indirect allowed, a direct forbidden and an indirect forbidden, n has values of $\frac{1}{2}$,2,$\frac{3}{2}$and3 respectively. For NiO,

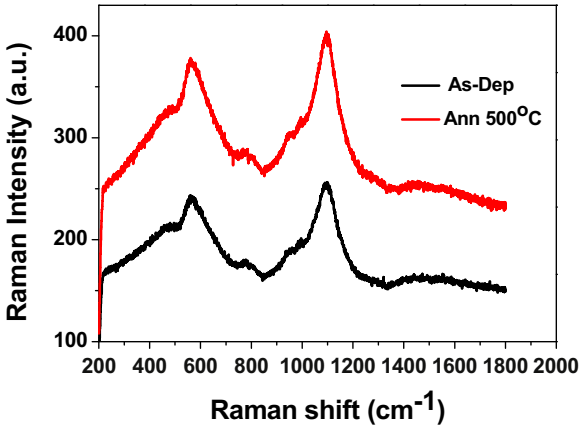

Fig. 4. Raman spectra of NiO thin film.

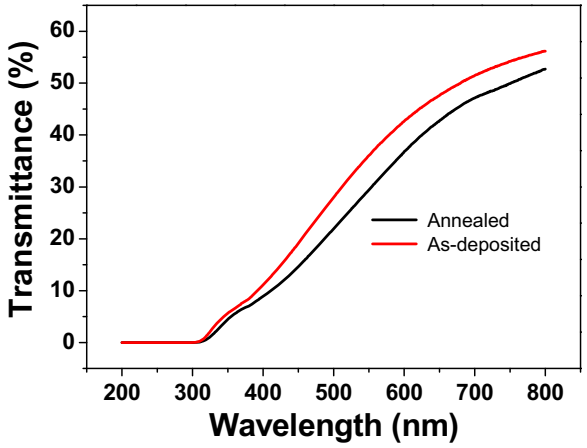

Fig. 5. Transmittance spectra of NiO thin film.

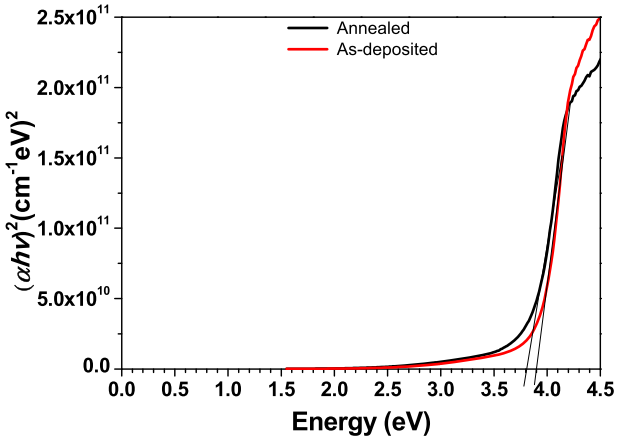

Fig. 6. Tauc Plot of NiO thin film annealed at 450°C for 1 h.

the value of n is $\frac{1}{2}$. A plot of $(\alpha h\nu)^2$ versus $h\nu$ was plotted as shown in Fig. 6, and the optical band gap of the films, found by extrapolating linear part of the curve to the $h\nu$ axis, was 3.9 eV and 3.8 eV for the as-deposited and annealed films respectively; this is within the range reported in literature [5,6].

An aluminium/nickel oxide/ITO structure that was formed by

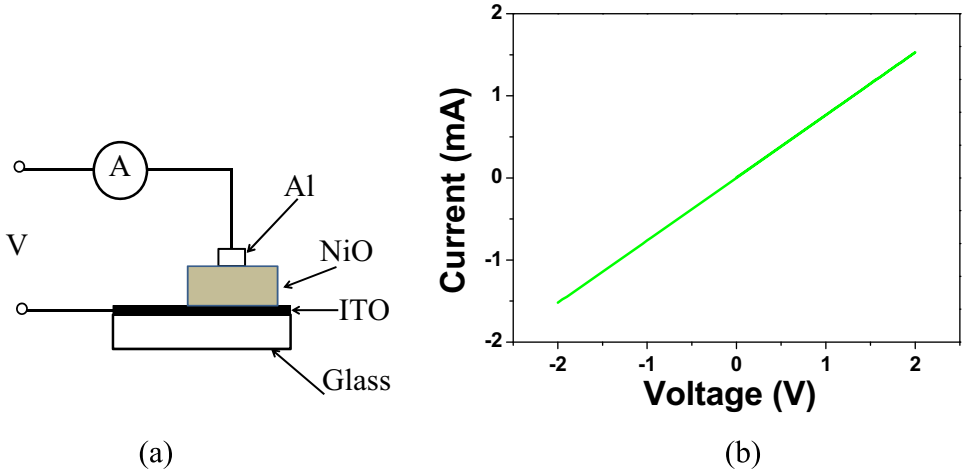

Fig. 7. (a) Schematic of Al/NiO/ITO structure used for electrical characterisation (b) I-V characteristics of Al/NiO/ITO structure.

Table 2
Properties of the nickel oxide thin films.

Properties			References
Resistivity (Ω cm)	Optical bandgap (eV)	Nature	
1×10^4–9×10^4	3.40 – 3.58	Non-porous	[20]
50×10^3–900×10^3	3.52 – 3.76	Non-porous	[21]
40×-160	3.49 – 3.75	Non-porous	[21]
3.78×10^4	3.80	Porous	This work

evaporation of aluminium contacts on the film is shown in Fig. 7a, the I-V characteristics of the film are shown in Fig. 7b. Resistance of the film as calculated from the slope of the graph was 1.313 kΩ; the electrical resistivity ρ was obtained from:

$$\rho = \frac{RA}{t}, \tag{7}$$

where R is the resistance of the film, A is the area of the aluminium contact and t is the film's thickness.

Considering the morphology of the annealed film, a contact is more likely to cover many nanowalls and pores, more so, during electrical measurement, the exact position of probes on the film cannot be ascertained. Therefore, the resistivity of the film which was found to be 3.78×10^4 Ωcm by making use the thickness of the film as shown in Fig. 3c, may be greater than its actual value. Comparison between the properties of the nickel oxide film and others found in literature is shown in Table 2.

4. Conclusions

A nickel oxide thin film was deposited by means of chemical bath deposition. It had a porous morphology and consisted of nanowalls; there was a decrease in the size of the nanowalls from an average of 76.67 nm to 52.00 nm after the film was subjected to thermal treatment. The film was polycrystalline with lattice constant of 0.417 nm. Optical properties of the film indicate that it was transparent in the visible and near infrared region with maximum transmittance of 49.76% for the annealed film. However, in the ultraviolet region, transmittance was very low and absorption was high. The absorption edge was blue-shifted with thermal treatment of the film. The optical bandgap of the annealed film was 3.8 eV. The electrical resistivity 378 Ωm in combination with the optical properties, show that these films are not suitable for use as a TCO. However, due to their porosity, they can be used in sensing applications.

Acknowledgements

This work was financially supported by the University of Pretoria and the National Research Foundation (NRF), South Africa Grant no: 91550. The authors also acknowledge the following: Isbé van der Westhuizen (Institute of Applied Materials), Wiebke Grote (Department of Geology) and Shankara Radhakrishnan (Department of Chemistry); all in University of Pretoria, for the assistance they rendered in carrying out Thermgravimetric, X-ray diffraction and UV–vis spectrophotometry analyses respectively, of the films.

References

[1] W. Chia-Ching, Y. Cheng-Fu, Investigation of the properties of nanostructured Li-doped NiO films using the modified spray pyrolysis method, Nanoscale Res. Lett. 8 (2013) 33. http://dx.doi.org/10.1186/1556-276X-8-33.
[2] A. Qurashi, Z. Zhang, M. Asif, T. Yamazaki, Synthesis NiO nanoflowers and their photoelectrochemical hydrogen production, Int. J. Hydrog. Energy 40 (2015) 15801–15805. http://dx.doi.org/10.1016/j.ijhydene.2015.07.114.
[3] L. Cattin, B.A. Reguig, A. Khelil, M. Morsli, K. Benchouk, J.C. Bern??de, Properties of NiO thin films deposited by chemical spray pyrolysis using different precursor solutions, Appl. Surf. Sci. 254 (2008) 5814–5821. http://dx.doi.org/10.1016/j.apsusc.2008.03.071.
[4] F.D. Auret, L. Wu, W.E. Meyer, J.M. Nel, M.J. Legodi, M. Hayes, Electrical characterisation of NiO/ZnO structures, Phys. Status Solidi 677 (2004) 674–677. http://dx.doi.org/10.1002/pssc.200304191.
[5] L. Berkat, L. Cattin, A. Reguig, M. Regragui, J.C. Bernede, Comparison of the physico-chemical properties of NiO thin films deposited by chemical bath deposition and by spray pyrolysis, Mater. Chem. Phys. 89 (2005) 11–20. http://dx.doi.org/10.1016/j.matchemphys.2004.07.005.
[6] B.A. Reguig, M. Regragui, M. Morsli, A. Khelil, M. Addou, J.C. Bern??de, Effect of the precursor solution concentration on the NiO thin film properties deposited by spray pyrolysis, Sol. Energy Mater. Sol. Cells 90 (2006) 1381–1392. http://dx.doi.org/10.1016/j.solmat.2005.10.003.
[7] X.H. Xia, J.P. Tu, J. Zhang, X.L. Wang, W.K. Zhang, H. Huang, Electrochromic properties of porous NiO thin films prepared by a chemical bath deposition, Sol. Energy Mater. Sol. Cells 92 (2008) 628–633. http://dx.doi.org/10.1016/j.solmat.2008.01.009.
[8] C. Hu, K. Chu, Y. Zhao, W.Y. Teoh, Efficient photoelectrochemical water splitting over anodized p type NiO porous films, ACS Appl. Mater. Interfaces 6 (2014) 18558–18568. http://dx.doi.org/10.1021/am507138b.
[9] A.A. Khaleed, A. Bello, J.K. Dangbegnon, D.Y. Momodu, M.J. Madito, F.U. Ugbo, et al., Effect of activated carbon on the enhancement of CO sensing performance of NiO, J. Alloy. Compd. 694 (2017) 155–162. http://dx.doi.org/10.1016/j.jallcom.2016.09.310.
[10] U.M. Patil, R.R. Salunkhe, K.V. Gurav, C.D. Lokhande, Chemically deposited nanocrystalline NiO thin films for supercapacitor application, Appl. Surf. Sci. 255 (2008) 2603–2607. http://dx.doi.org/10.1016/j.apsusc.2008.07.192.
[11] M.A. Vidales-Hurtado, A. Mendoza-Galván, Optical and structural characterization of nickel oxide-based thin films obtained by chemical bath deposition, Mater. Chem. Phys. 107 (2008) 33–38. http://dx.doi.org/10.1016/j.matchemphys.2007.06.036.
[12] A.M.F. Benial, Studies on chemical bath deposited CuO thin films for solar cells application, J. Mater. Sci. Mater. Electron. 26 (2015) 8489–8496. http://dx.doi.org/10.1007/s10854-015-3520-3.
[13] K.H. Kim, C. Takahashi, Y. Abe, M. Kawamura, Optik Effects of Cu doping on nickel oxide thin film prepared by sol–gel solution process, Opt. – Int. J. Light Electron

Opt. 125 (2014) 2899–2901. http://dx.doi.org/10.1016/j.ijleo.2013.11.074.
[14] M.S. Yadav, S.K. Tripathi, Synthesis and characterization of nanocomposite NiO/activated charcoal electrodes for supercapacitor application, Ionics (2017). http://dx.doi.org/10.1007/s11581-017-2026-9.
[15] S.-Y. Han, D.-H. Lee, Y.-J. Chang, S.-O. Ryu, T.-J. Lee, C.-H. Chang, The growth mechanism of nickel oxide thin films by room-temperature chemical bath deposition, J. Electrochem. Soc. 153 (2006) C382. http://dx.doi.org/10.1149/1.2186767.
[16] J.L. Gunjakar, A.M. More, C.D. Lokhande, Chemical deposition of nanocrystalline nickel oxide from urea containing bath and its use in liquefied petroleum gas sensor, Sens. Actuators B Chem. 131 (2008) 356–361. http://dx.doi.org/10.1016/j.snb.2007.11.042.
[17] N. Mironova-Ulmane, A. Kuzmin, I. Steins, J. Grabis, I. Sildos, M. Pars, Raman scattering in nanosized nickel oxide NiO, in: Funct. Mater. Nanotechnologies, IOP Publishing Ltd, 2007, pp. 1–5. ⟨http://doi.org/10.1088/1742-6596/93/1/012039⟩.
[18] A.A. Al-Ghamdi, W.E. Mahmoud, S.J. Yaghmour, F.M. Al-Marzouki, Structure and optical properties of nanocrystalline NiO thin film synthesized by sol-gel spin-coating method, J. Alloy. Compd. 486 (2009) 9–13. http://dx.doi.org/10.1016/j.jallcom.2009.06.139.
[19] K.K. Purushothaman, S.J. Antony, G. Muralidharan, Optical, structural and electrochromic properties of nickel oxide films produced by sol–gel technique, Sol. Energy 85 (2011) 978–984. http://dx.doi.org/10.1016/j.solener.2011.02.012.
[20] P.S.P, L.D. Kadam, Preparation and characterization of spray pyrolyzed nickel oxide (NiO) thin films, Appl. Surf. Sci. 199 (2002) 211–221. http://dx.doi.org/10.1016/S0169-4332(02)00839-5.
[21] M. Jlassi, I. Sta, M. Hajji, H. Ezzaouia, Optical and electrical properties of nickel oxide thin films synthesized by sol-gel spin coating, Mater. Sci. Semicond. Process. 21 (2014) 7–13. http://dx.doi.org/10.1016/j.mssp.2014.01.018.

5.4 The effects of annealing temperature on the structural properties of the films

The effects of other annealing temperatures, different from the ones in the paper, on the structural properties of the deposited film is presented in this section. The XRD data were obtained in the same acquisition time and the XRD pattern of the films is shown in Figure 5.2. There are two diffraction peaks at 38.70 ° and 69.98 ° in the as-deposited film. These correspond to (100) and (110) diffraction peaks of the hexagonal nickel hydroxide $a = 3.126$ nm, $c = 4.605$ nm according to JCPDS file number 14-0117) [1]. However, in the annealed films, three peaks at 43.57°, 50.99° and 74.61° can be seen in the Figure. These peaks were assigned to (111), (200) and (220) diffraction planes of cubic NiO as indexed to JCPDS file No. 04-0835 [2]. The XRD patterns confirmed the structural difference between the as-deposited and annealed films and the transformation of phase that took place during annealing.

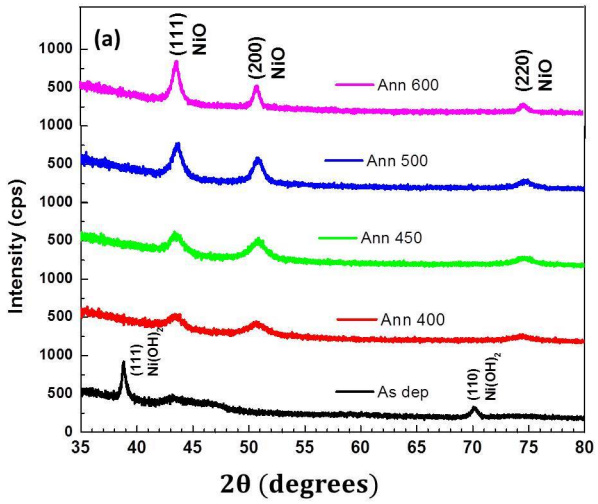

Figure 5.2: X-ray diffraction (XRD) patterns of the films; as-deposited and annealed at different temperatures.

In the films that were annealed at 400 ℃ and 450 ℃, the intensities of the (111) and the (200) peaks were almost equal. The intensity of the (111) peak became more prominent as the annealing temperature increased. The intensities of other peaks were also enhanced by annealing. This was an indication that the crystallinity of the NiO improved with increasing temperature of annealing. There was no evidence of the hydrated $Ni(OH)_2$ phase after annealing at 400 ℃ and 450 ℃. For adequate comparison of intensity of diffraction peaks, the XRD

patterns of the film annealed at 350 ℃ and 500 ℃ are shown in Figure 2 in the paper. The inter-planar spacing was calculated using Equation 4.4; the wavelength of the X-rays, for Co K_α radiation is 0.1789 nm. The lattice constant was calculated using Equation 4.5. There was no change in the position of the peaks as a result of annealing, however, the full-width-half-maximum (FWHM) of the peaks was reduced as the annealing temperature was increased. This implies that the crystallite size of the films was increasing.

Values of the inter-planar spacing and lattice constants calculated for the film annealed at 500 ℃, using Equation 4.5 are shown in Table 5.1. A comparison between the inter-planar spacing and lattice constant of the film and the JCPDS file was made and shown in the table. The *d*-spacing and lattice constants of the film were very close to values reported by [2]. Similar structural properties were reported by [3, 4]

Table 5.1: Calculated inter-planar distance and lattice constant of NiO thin film after annealing at 500 ℃

	JCPDS 04-0835		This work		Ref[2]	
(*hkl*)	*d* (nm)	*a* (nm)	*d* (nm)	*a*(mm)	*d* (nm)	*a* (nm)
111	0.2410	0.4176	0.2410	0.4175	0.2411	0.4176
200	0.2088	0.4176	0.2078	0.4156	0.2088	0.4176
220	0.1476	0.4176	0.1477	0.4177	–	–

5.4.1 Summary and conclusions

A nickel oxide thin film was deposited using the chemical bath deposition method, the precursor was Nickel (II) sulphate hexahydrate. The complex formed with ammonia was found to dissociate easily, and led to films that did not adhere to the substrates. NiO films that were deposited using ammonia were found to be porous nanowall structures.

With monoethanolamine as the complexing agent, the deposition was carried out in an alkaline medium at a temperature of 70 ℃. The film was found to have a porous morphology that was made of nanowalls in a honey-comb like structure; there was a decrease in the size of the nanowalls from an average of 76.67 nm to 52.00 nm after annealing the film at 450 ℃ for 1 h. The film was polycrystalline with an average lattice constant of 0.417 nm. The optical properties of the film indicated that it was transparent in the visible and near infrared

region with a maximum transmittance of 50% for the annealed film. In the ultraviolet region, the transmittance was low. The absorption edge was blue-shifted after thermal treatment of the film. The optical bandgap of the annealed film was found to be 3.8 eV. The electrical resistivity was calculated to be 3.8×10^4 Ω.cm. Considering the morphology of the annealed film, a metal contact will cover many nanowalls and pores, thus increasing the surface area of the contact, more so, the exact position of probes on the film cannot be ascertained during electrical measurement. Therefore, the experimentally determined bulk resistivity of the film might be greater or lower than its actual value. The observed properties of these films show that they are not suitable for use as a transparent conducting oxide. However, due to their porosity, the films might be useful in chemical or biochemical sensing applications.

References

[1] Guan Xiao-yan and Deng Jian-Cheng. Preparation and electrochemical performance of nano-scale nickel hydroxide with different shapes. *Materials Letters*, 61(3):621–625, 2007.

[2] Kyung Ho Kim, Chiaki Takahashi, Yoshio Abe, and Midori Kawamura. Effects of Cu doping on nickel oxide thin film prepared by sol–gel solution process. *Optik-International Journal for Light and Electron Optics*, 125(12):2899–2901, 2014.

[3] L Cattin, BA Reguig, A Khelil, M Morsli, K Benchouk, and JC Bernede. Properties of NiO thin films deposited by chemical spray pyrolysis using different precursor solutions. *Applied Surface Science*, 254(18):5814–5821, 2008.

[4] Chenyan Hu, Kenneth Chu, Yihua Zhao, and Wey Yang Teoh. Efficient photoelectrochemical water splitting over anodized p-type NiO porous films. *ACS Applied Materials & Interfaces*, 6(21):18558–18568, 2014.

Chapter 6

Results: Deposition of NiO thin films using sol-gel spin coating

6.1 Introduction

In spin coating, a small quantity of a fluid is deposited on a substrate and the substrate is spun at high speed [1]. A thin film of the fluid is left on the substrate as the centrifugal force causes the fluid to spread over and off the edge of the substrate. The outward flow is combined with evaporation thereby causing the film to thin out. It is necessary to dry the thin film in order to remove solvents and other species that are produced during deposition. The drying temperature to be applied depends on the properties of the materials to be eliminated from the film. Apart from this, the decomposition of some precursors into intermediate products usually takes place during drying. [2]. The precursors that are normally used to produce thin films of metal oxides in the sol-gel method include organic or inorganic salts of the metals, and metal acetates which are commonly used due to their stability and environmental friendliness. The metal acetates are dissolved in suitable polar or non-polar solvents.

Thin films of nickel oxide were fabricated using the sol-gel method and the effect of temperatures of drying and annealing on the properties of the films were studied. The condition that was found to be optimum for making films of good electrical properties was used to deposit NiO films on a p-silicon substrate and aluminium contacts were deposited to make Schottky contacts to the film. The behaviour of the metal-semiconductor junction was investigated. Results of the investigations are

presented in this chapter.

6.2 Optimisation of the spin coating process

The morphologies of the films that were produced from 0.1 M and 0.2 M solutions of nickel acetate tetrahydrate are shown in Figure 6.1. The speed of the spin coater was 1500 rpm and it was operated for 30 s, the films were annealed at 400 ℃. The SEM results show that the films are granular but the XRD results (not shown) indicated that the films were amorphous.

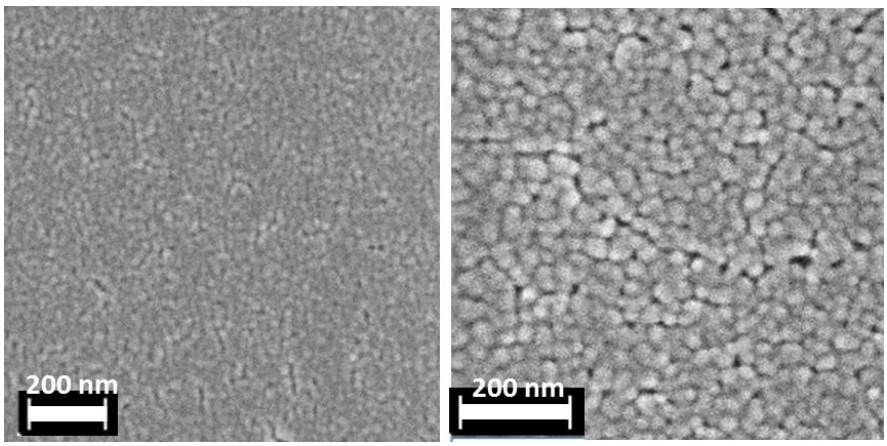

Figure 6.1: SEM images of films made from (a) 0.1 M and (b) 0.2 M solutions.

The concentration of the precursor was increased gradually until it reached 0.7 M. The precursor solution became denser with increasing concentration, therefore the speed of the spin coater was also increased. The various speeds of the spin coater that were used and the time of deposition are shown in Table 6.1. When the concentration of 0.75 M was attained, the XRD results of the films after they have been annealed at 400 ℃ is shown in Figure 6.2. The XRD patterns showed that the films were polycrystalline due to the presence of diffraction peaks from different crystallographic planes.

Table 6.1: Speeds of spin-coater and duration for different concentrations of precursor.

Concentration (M)	Speed (rpm)	Time (s)
0.1	1500	30
0.2	1500	30
0.5	2000	25
0.7	3000	25

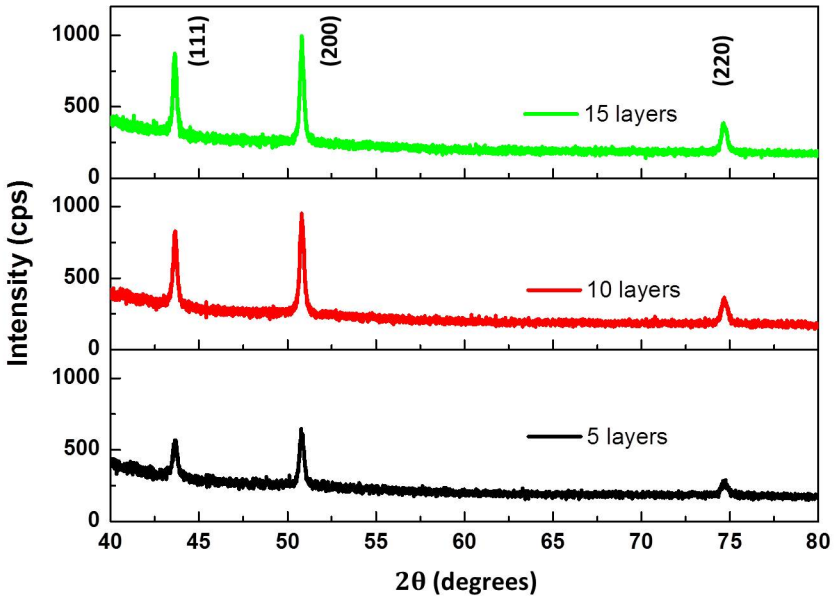

Figure 6.2: XRD patterns of different number of layers of NiO films fabricated from 0.7 M solution of nickel acetate and annealed at 400 ℃. Recorded with Co Kα X-rays.

With increasing number of layers, there was an increase in the intensity of the diffraction peaks this was an indication that the number of particles causing the diffraction increases as the number of layers increases.

6.3 Effects of thermal treatment on properties of sol - gel fabricated NiO this films

The results of the investigation of the effects of temperatures of drying and annealing on the structural, optical and electrical properties of the sol-gel fabricated NiO thin films are presented in Paper 2, titled: Effects of thermal treatment on structural, optical and electrical properties of NiO thin films.

Physica B 575 (2019) 411694

Contents lists available at ScienceDirect

Physica B: Physics of Condensed Matter

journal homepage: http://www.elsevier.com/locate/physb

Effects of thermal treatment on structural, optical and electrical properties of NiO thin films

Shadrach T. Akinkuade [a,b,*], Walter E. Meyer [a], Jacqueline M. Nel [a]

[a] Physics Department, University of Pretoria, Pretoria, 0002, South Africa
[b] Physics Unit, Science Technology Department, Federal Polytechnic, Ado-Ekiti, Nigeria

ARTICLE INFO

Keywords:
Nickel oxide
Annealing
Sol-gel
Spin coating
Resistivity

ABSTRACT

The spin-coating technique was utilized to produce thin films of nickel oxide on glass substrates. Three drying temperatures, 160 °C, and 200 °C, and 250 °C were used. Annealing temperatures ranged from 300 °C to 600 °C. The effects of drying and annealing temperatures on the films were examined with X-ray diffraction, scanning electron microscopy, Raman spectroscopy, UV–vis spectrophotometry and linear four-point probe measurements. The crystallinity of the films was found to improve as the annealing temperature increased. The average crystallite size varied from 14 nm to 28 nm for films that were dried at 200 °C and 14 nm–32 nm for films that were dried at 250 °C as the annealing temperature was increased. Optical transmittance of the films from 800 nm to 350 nm, varied from 64% to 96%. Two peaks at 558 cm^{-1} and 1100 cm^{-1} in the Raman spectra of the films confirmed the presence of NiO on the films.

1. Introduction

Nickel oxide (NiO) is a transition metal oxide, it has a wide optical band gap from 3.6 to 4.0 eV [1] that crystallizes in the cubic rock-salt structure [2]. In stoichiometric form, NiO is an insulator, with a resistivity of about $10^{13}\,\Omega$ cm [3,4] and can not be used as a semiconductor. P-type conductivity in NiO has been attributed to nickel vacancies or oxygen interstitials [5]. Due to interesting properties of nickel oxide such as chemical stability, wide and tunable optical band gap, and p-type conductivity, it has been found useful in many applications such as electrochromic displays [6], p-type conducting oxide [1], active layer in chemical sensors [7], solar cells [8–10], ultra violet detectors [11,12], light emitting diodes [13] and photoelectrolysis [14].

Many techniques have been employed to produce NiO thin films including electron beam evaporation [15], sputtering [16], thermal evaporation [17], pulsed laser deposition [18], spin-coating [19], dip-coating [20,21], chemical bath deposition [22], and spray pyrolysis [23]. The properties of these films that make them suitable for specific applications depend on conditions and techniques of deposition [24]. Simplicity, low cost, and ease of control of the microstructure of the deposited film are some of the gains of the sol-gel technique [25].

In the production of thin films of nickel oxide, hydrated nickel acetate is a common precursor, 2-methoxy ethanol is used as a solvent while monoethanolamine serves as the stabilizer. The films are usually subjected to two thermal processes during fabrication; drying to evaporate organic solvents and annealing for the transformation of precursor or any intermediate product formed during drying into NiO. Thermal decomposition of hydrated metal acetates takes place in three steps in different temperature regions [26,27], reports on the effects of different processing temperatures on the electrical properties of sol-gel fabricated NiO films is scarce in literature. For instance, Al-Ghamdi et al. [19] studied the structural and optical properties of NiO films (excluding resistivity) dried at 200 °C and annealed at 600 °C. Jlassi et al. [20] dried NiO films at 275 °C and annealed the films at temperatures from 300 °C to 600 °C, 600 °C was found to be the optimum temperature of annealing and the study was focused on the effects of number of layers and annealing atmosphere on the properties of the films annealed at this temperature. The effects of lithium doping on the properties of NiO films dried at 300 °C and annealed at 600 °C was studied by Sta et al. [28]. In this work, the effects of different temperatures of drying and annealing on some properties of NiO thin films were investigated.

2. Experimental

Microscope slides made of soda lime glass were used as substrates. Before deposition, they were cut into 25 mm × 10 mm × 1 mm and

* Corresponding author. Physics Department, University of Pretoria, Pretoria, 0002, South Africa.
E-mail address: u14302552@tuks.co.za (S.T. Akinkuade).

https://doi.org/10.1016/j.physb.2019.411694
Received 8 June 2019; Received in revised form 29 August 2019; Accepted 10 September 2019
Available online 14 September 2019

washed as described elsewhere [29]. 0.75 M solution of nickel (II) acetate tetrahydrate ($Ni(CH_3COO)_2.4H_2O$) was prepared in 2-methoxy ethanol ($C_3H_8O_2$). Monoethanolamine (C_2H_7NO) (MEA) was used as the stabilizer. The molar ratio of nickel acetate to MEA was 1.0. Stirring of the solution was done for 60 min at 65 °C, the solution was allowed to age for 24 h at the room temperature. The prepared solution was spin coated onto the washed substrates at 3000 rpm for 25 s. Drying of the films was done for 10 min at 160 °C, 200 °C and 250 °C. The process was repeated four times. The films were annealed for 1 h in air inside a tube furnace between 300 °C and 600 °C.

Structural properties of the films were studied with a Rigaku Smartlab X-ray diffractometer (XRD) using Cu Kα radiation ($\lambda = 0.15409$ nm) in the range of 2θ from 5° to 89.9°. The morphology of the films was studied with field emission scanning electron microscope (FESEM ZEISS Crossbeam 540) at an acceleration voltage of 1 kV while a Bruker Dimension Icon scanning probe microscope (SPM) in ScanAsyst mode was used to examine the topography of the films. The transmittance spectra were recorded with a CARY 100 BIO UV–vis spectrophotometer in the wavelength range 200 nm–800 nm. Raman spectra were recorded between 300 and 1500 cm^{-1} using WITec alpha 300 RAS + confocal Raman microscope, with 532 nm excitation laser at 50 mW laser power. The resistivity of the samples was obtained using the linear four-point probe measurement system.

3. Results and discussion

3.1. Structural properties

3.1.1. X-ray diffraction

The XRD patterns of the films are presented in Fig. 1. The peaks at 37.24°, 43.23° and 62.85° originating from diffraction planes (111), (200) and (220) were indexed to NiO (JCPDS card number 47-1049) [30]. The XRD results showed the polycrystalline nature of the face-centred NiO films with no preferred orientation. The interplanar distance and lattice parameter for each plane of diffraction was calculated, the average lattice constant of the film was found to be 0.4180 nm which was very close to 0.4178 nm of JCPDS 47-1049. The film that was dried at 160 °C, annealed at 300 °C (the XRD pattern not shown) was amorphous. The intensities of XRD peaks for other films dried at this temperature were generally low when compared to XRD peaks of other films dried at higher temperatures. The intensities did not show a remarkable increase with an increase in annealing temperatures, this might be due to the fact that the stabilizer (MEA) has a boiling point of 170.8 °C. Therefore, it does not vaporize at 160 °C and phase transformation from precursor to NiO did not take place.

The intensity of diffraction peaks of films that were dried at 200 °C and 250 °C increased with annealing temperature. This shows that high annealing temperatures favor the transformation from precursor to NiO. The maximum intensity of peaks was observed in the film dried at 200 °C. Above this drying temperature, there might be rapid vaporization of solvent and stabilizer during the drying process which could hinder crystallization of NiO. The full-width-half-maximum (FWHM) of the films were perceived to decrease with annealing temperature. Crystallite size of the films that were dried at 200 °C and 250 °C were calculated based on the FWHM of the peaks (111), (200) and (220) using the Scherrer formula [31], the result is shown in Table 1. The crystallite size was found to increase as the temperature of annealing increased. The drying temperature was found to have less of influence on the crystallite size.

3.1.2. Microstructural properties

The scanning electron micrographs of the thin films are presented in Fig. 2. The images revealed that the films were granular, with grains of uniform size, there was an increase in grain size as the annealing temperature is raised. This is in agreement with the XRD results. Details of the grains can be observed more distinctly in the SEM images of films that were annealed at 500 °C and 600 °C. The SPM micrographs

Table 1
Summary of some features of the films.

Drying temperature (°C)	Annealing temperature (°C)	Average crystallite size (mm)	Optical Band gap (eV)	Resistivity (Ω.cm)
160	400	–	3.94	210
	500	–	3.92	135
	600	–	3.87	820
200	400	13.64	3.71	186
	500	16.31	3.64	125
	600	28.39	3.55	770
250	400	13.40	3.79	170
	500	24.56	3.76	105
	600	31.70	3.74	670

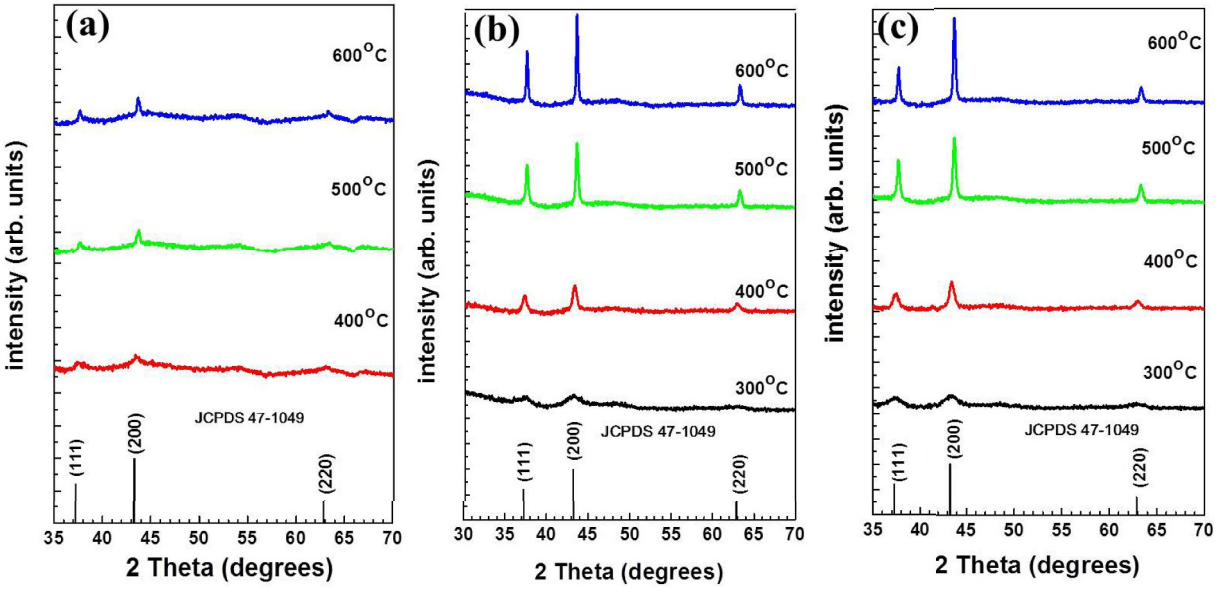

Fig. 1. XRD patterns of films dried at (a) 160 °C (b) 200 °C and (c) 250 °C.

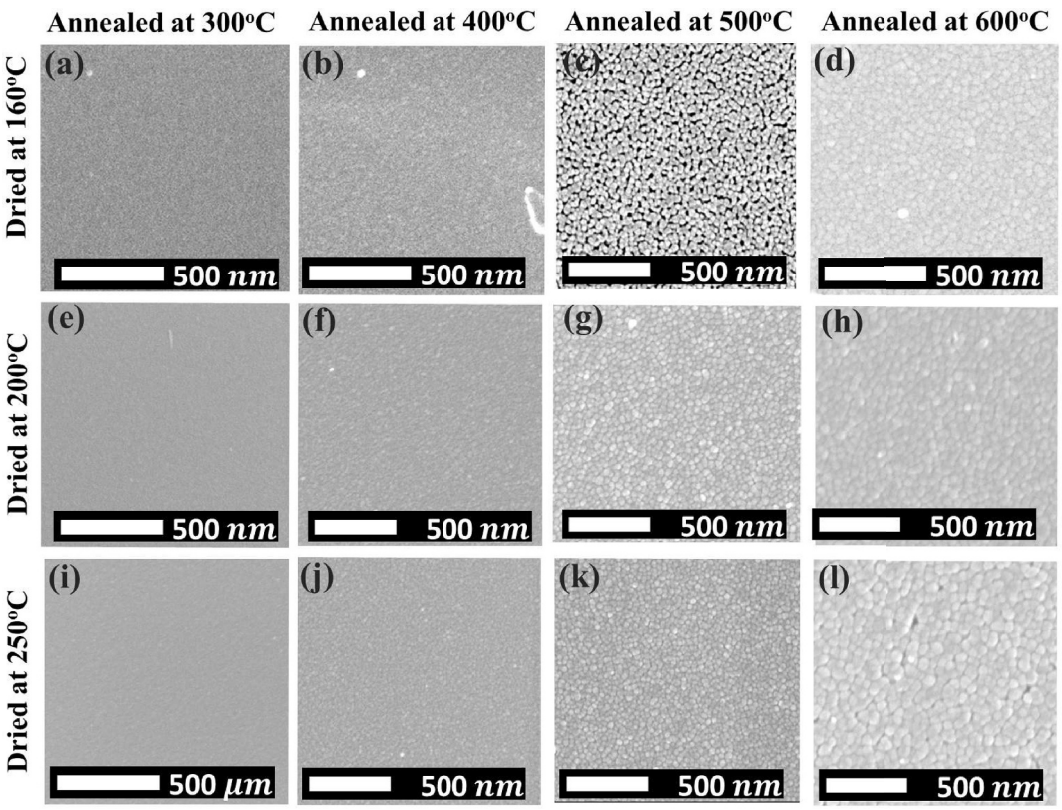

Fig. 2. FESEM images of films dried at 160 °C, 200 °C, 250 °C annealed at 300 °C, 400 °C, 500 °C and 600 °C.

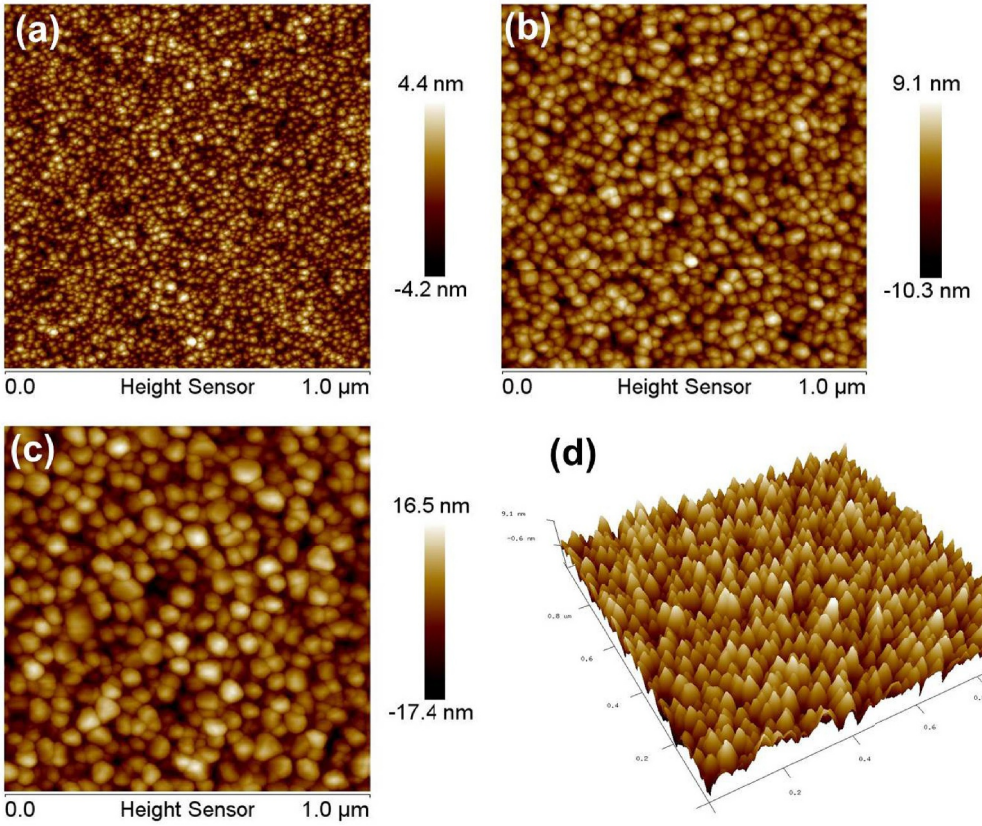

Fig. 3. SPM image of films dried at 250 °C, annealed at (a) 400 °C, (b) 500 °C, (c) 600 °C and (d) 3-D image (1 μm × 1 μm) of film annealed at 500 °C.

(1 μm × 1 μm) of the films that were dried at 250 °C and annealed at different temperatures are shown in Fig. 3. The root-mean-square values of the surface roughness of these films were obtained as 1.58 nm, 2.77 nm and 4.93 nm respectively.

3.2. Optical properties

3.2.1. Raman spectroscopic analysis

Fig. 4 shows the Raman spectra of the films recorded from 300 cm^{-1}–1500 cm^{-1}. The spectra have two bands, these were among the five bands of vibrational origin in NiO as stated by Ref. [32]. There were two prominent peaks around 560 cm^{-1} and 1100 cm^{-1}, in the spectra of the films that were dried at 160 °C. These were one-phonon first-order longitudinal-optical (1P) LO mode and two-phonon second-order longitudinal-optical mode (2P) 2LO respectively. For films that were dried at 200 °C and 250 °C, the intensity of the (2P) 2LO peak (1100 cm^{-1}) varies with annealing temperature. The increase in the intensity of (1P) LO peak in NiO was due to parity-breaking defects such as nickel vacancies [32], thus the increase in the peak at 557 cm^{-1} in the spectra of films dried at 200 °C, annealed at 400 °C and films dried at 250 °C and annealed at 400 °C and 500 °C, suggest that these films could have nickel vacancies as defects.

3.2.2. UV–vis spectrophotometric analysis

The transmittance spectra as measured from 300 to 800 nm are given in Fig. 5. From 800 nm to 350 nm, the transmittance of films that were dried at 160 °C varied from 96% to 78%. For films that were dried at 200 °C, transmittance varied from 87% to 64% while transmittance in films that were dried at 250 °C varied from 92% to 72%. The lower transmittance observed in the films that were dried 200 °C, might be ascribed to increase in the scattering of photons in the films due to increasing grain size compared to films dried at 160 °C. There were ripples in the transmittance spectra of films dried at 200 °C and 250 °C, this was due to interference between light and nanoparticles in the films [33] or interference among multiple reflected waves [34].

The coefficient of absorption was calculated from $\alpha = \frac{1}{d} ln \frac{1}{T}$ [15], where T is the transmittance and d is the film's thickness. The optical band gap E_g of the film was obtained from the plot of $(\alpha h\nu)^2$ versus photon energy ($h\nu$), as explained by Ref. [15], where h is the Plank's constant. The calculated optical band gaps are stated in Table 1. The decrease in the optical band gaps of these films due to the rise in annealing temperatures might be caused by quantum confinement. According to Sing et al. [35], the band gap of a nanomaterial varies inversely to the diameter of its nanoparticles. The increase in the annealing temperature results in an increase in the size of particles, consequently, the optical band gap of the films decreases.

3.3. Electrical properties

Results of the measurement obtained from the linear four-point probe are shown in Table 1. Resistivity is a function of the concentration of carriers and mobility of carriers both of which may be influenced by the presence of defects. In the thin films, the contribution of each of these factors to the resistivity, depends on the temperatures at which they were processed. From Table 1, the resistivity of the films were observed to decrease as the drying temperature was increased. An increase in the annealing temperature from 400 °C to 500 °C, caused the resistivity to decrease. Further increase in the temperature of annealing from 500 °C to 600 °C caused the resistivity to increase. The initial reduction in resistivity due to an increase in the annealing temperature could be ascribed to increase in the size of grains in the films which leads to a reduction in grain boundaries, thereby enhancing the mobility of carriers. Despite the further increase in the grain size while the temperature of annealing increases, the resistivity increases. This might be prompted by the reduction in the concentration of defects in the films as explained by Mooney et al. [36] leading to a reduction in the number of charge carriers. Generally, the resistivity of the films varies with both drying and annealing temperatures. At a low temperature of annealing, the resistivity depends on the mobility of carriers, at a higher temperature, resistivity is determined by the concentration of defects.

4. Conclusions

There was an improvement in the crystallinity of NiO films as annealing temperature increased. Films that were dried at 160 °C were not as crystalline as other films that were dried at higher temperatures. Films that were annealed at 300 °C, irrespective of the drying temperatures, showed poor crystallinity. Morphology of the films revealed that they were homogeneous and consisting of grains of uniform size, the grain size increase from about 14 nm to 28 nm for films that were dried

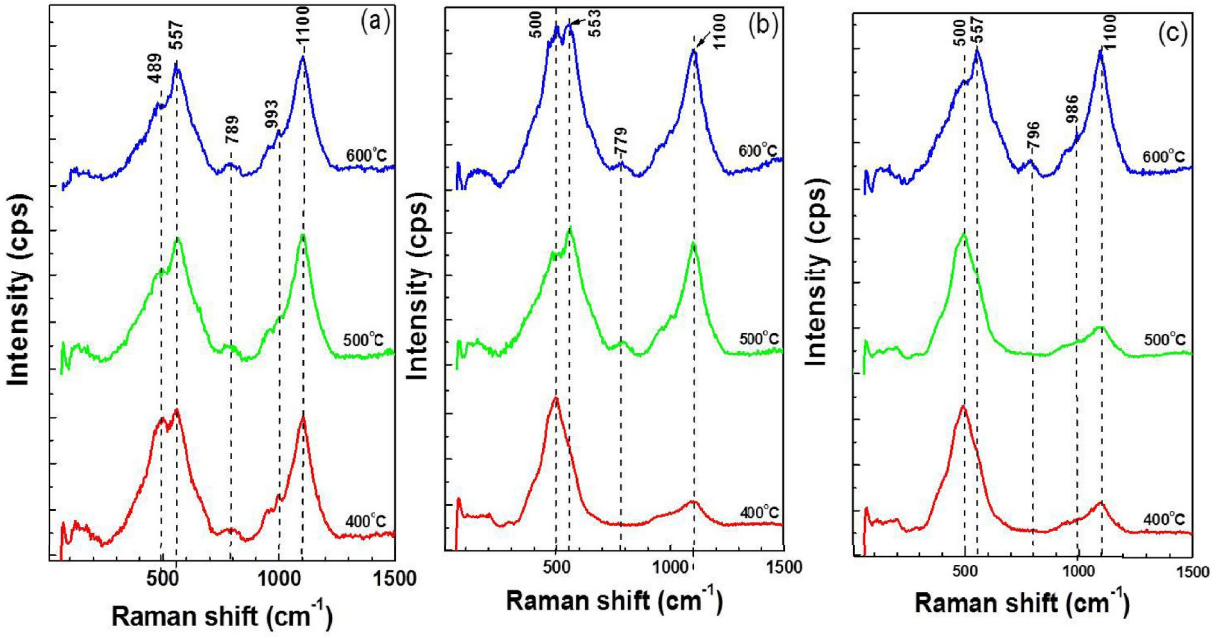

Fig. 4. Raman spectrum of films (a) dried at 160 °C (b) dried at 200 °C (c) dried at 250 °C and annealed between 400 °C and 600 °C.

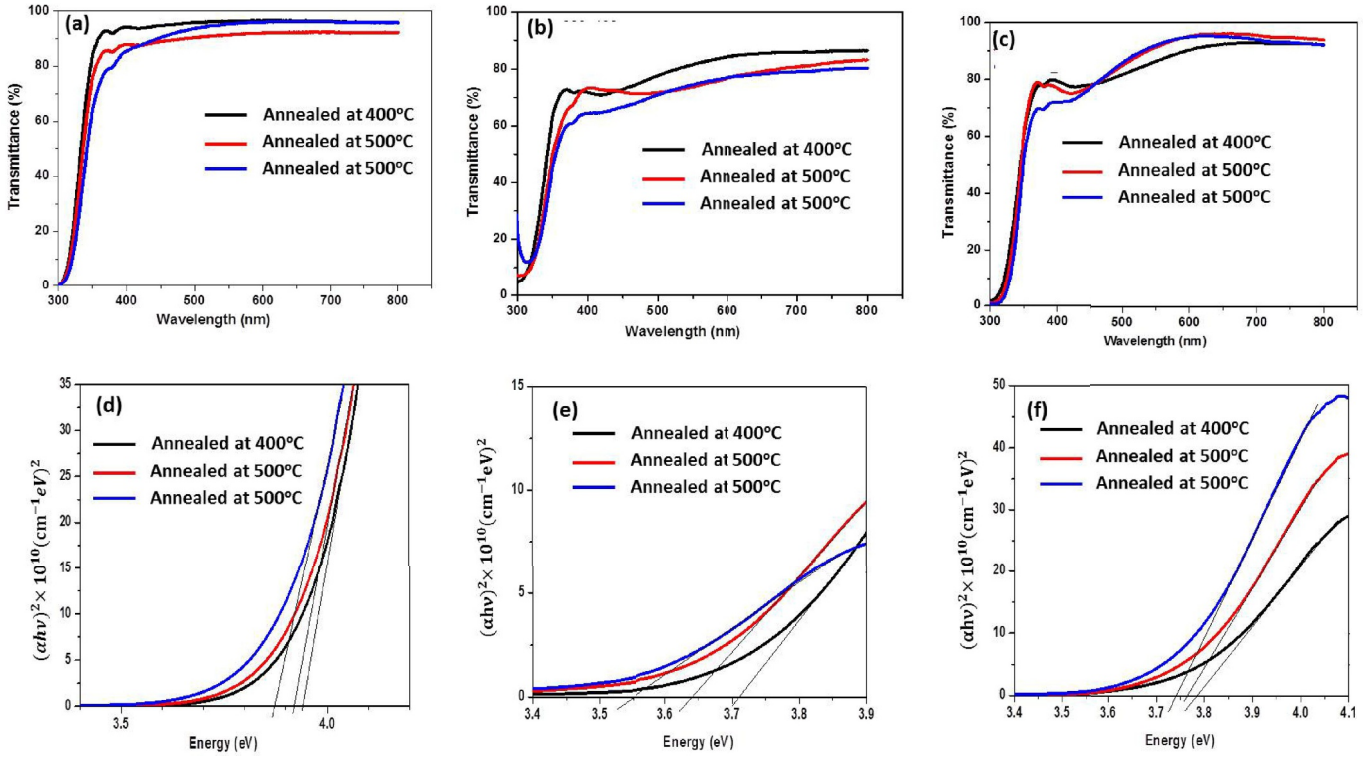

Fig. 5. Transmittance spectra of the films dried at (a) 160 °C (b) 200 °C and (c) 250 °C; (d), (e), and (f) are Tauc's plot for the films respectively.

at 200 °C and 14 nm–32 nm for films dried at 250 °C as the temperature of annealing was increased from 400 °C to 600 °C. The transmittance of the films varied from 78% to 96%, from 64% to 87%, and from 72% to 92% as the wavelengths varied from 350 to 800 nm, for drying temperatures of 160 °C, 200 °C, and 300 °C respectively. Raman spectra of the films showed that two prominent Raman peaks at 558 cm^{-1} and 1100 cm^{-1} for one-phonon first-order longitudinal-optical (1P) LO mode and two-phonon second-order longitudinal-optical mode (2P) 2LO respectively were found in all the films. For films that were dried at 250 °C and annealed at 400 °C and 500 °C, the enhancement of (1P) LO peak over that of (2P) 2LO was an indication that these films were richer in defects than those annealed at 600 °C. The electrical resistivity of the films as measured using the linear four-point probe system showed that the resistivity decreased with increasing drying temperature, the minimum resistivity was obtained in all the films at an annealing temperature of 500 °C. The resistivity of the films was found to depend on the grain size as well as the presence of defects. Annealing the films above 500 °C reduced the concentration of defects and thus an increase in the resistivity was observed. This work revealed the dependence of resistivity of sol-gel fabricated NiO thin films on temperature of processing, both drying and annealing.

Acknowledgment

This work was financially supported by the University of Pretoria and the National Research Foundation (NRF) South Africa, Grant number 111744. The opinions, findings, conclusions or recommendations are that of the authors, and the NRF accepts no liability in this regard.

References

[1] H. Sato, T. Minami, S. Takata, T. Yamada, Transparent conducting p-type NiO thin films prepared by magnetron sputtering, Thin Solid Films 236 (1–2) (1993) 27–31, https://doi.org/10.1016/0040-6090(93)90636-4.

[2] A.A. Al-Ghamdi, M.S. Abdel-wahab, A. Farghali, P. Hasan, Structural, optical and photo-catalytic activity of nanocrystalline NiO thin films, Mater. Res. Bull. 75 (2016) 71–77, https://doi.org/10.1016/j.materresbull.2015.11.027.

[3] D. Adler, J. Feinleib, Electrical and optical properties of narrow-band materials, Phys. Rev. B 2 (8) (1970) 3112, https://doi.org/10.1103/PhysRevB.2.3112.

[4] W.-L. Jang, Y.-M. Lu, W.-S. Hwang, W.-C. Chen, Electrical properties of Li-doped NiO films, J. Eur. Ceram. Soc. 30 (2) (2010) 503–508, https://doi.org/10.1016/j.jeurceramsoc.2009.05.041.

[5] S. Nandy, B. Saha, M.K. Mitra, K. Chattopadhyay, Effect of oxygen partial pressure on the electrical and optical properties of highly (200) oriented p-type $Ni_{1-x}O$ films by DC sputtering, J. Mater. Sci. 42 (14) (2007) 5766–5772, https://doi.org/10.1007/s10853-006-1153-x.

[6] M. Kitao, K. Izawa, K. Urabe, T. Komatsu, S. Kuwano, S. Yamada, Preparation and electrochromic properties of RF-sputtered NiOx films prepared in $Ar/O_2/H_2$ atmosphere, Jpn. J. Appl. Phys. 33 (12R) (1994) 6656, https://doi.org/10.1143/JJAP.33.6656.

[7] C.-Y. Lee, C.-M. Chiang, Y.-H. Wang, R.-H. Ma, A self-heating gas sensor with integrated NiO thin-film for formaldehyde detection, Sens. Actuators B Chem. 122 (2) (2007) 503–510, https://doi.org/10.1016/j.snb.2006.06.018.

[8] K.X. Steirer, J.P. Chesin, N.E. Widjonarko, J.J. Berry, A. Miedaner, D.S. Ginley, D. C. Olson, Solution deposited NiO thin-films as hole transport layers in organic photovoltaics, Org. Electron. 11 (8) (2010) 1414–1418, https://doi.org/10.1016/j.orgel.2010.05.008.

[9] J.R. Manders, S.-W. Tsang, M.J. Hartel, T.-H. Lai, S. Chen, C.M. Amb, J. R. Reynolds, F. So, Solution-processed nickel oxide hole transport layers in high efficiency polymer photovoltaic cells, Adv. Funct. Mater. 23 (23) (2013) 2993–3001, https://doi.org/10.1002/adfm.201202269.

[10] J.H. Kim, P.-W. Liang, S.T. Williams, N. Cho, C.-C. Chueh, M.S. Glaz, D.S. Ginger, A.K.-Y. Jen, High-performance and environmentally stable planar heterojunction perovskite solar cells based on a solution-processed copper-doped nickel oxide hole-transporting layer, Adv. Mater. 27 (4) (2015) 695–701, https://doi.org/10.1002/adma.201404189.

[11] J.-M. Choi, S. Im, Ultraviolet enhanced Si-photodetector using p-NiO films, Appl. Surf. Sci. 244 (1–4) (2005) 435–438, https://doi.org/10.1016/j.apsusc.2004.09.152.

[12] S.-Y. Tsai, M.-H. Hon, Y.-M. Lu, Fabrication of transparent p-NiO/n-ZnO heterojunction devices for ultraviolet photodetectors, Solid State Electron. 63 (1) (2011) 37–41, https://doi.org/10.1016/j.sse.2011.04.019.

[13] S.-W. Park, J.-M. Choi, E. Kim, S. Im, Inverted top-emitting organic light-emitting diodes using transparent conductive NiO electrode, Appl. Surf. Sci. 244 (1–4) (2005) 439–443, https://doi.org/10.1016/j.apsusc.2004.10.099.

[14] S. Wahyuningsih, C. Purnawan, T.E. Saraswati, E. Pramono, A.H. Ramelan, S. Pramono, A. Wisnugroho, Visible light photoelectrocatalytic degradation of rhodamine B using Ti/TiO_2-NiO photoanode, J. Environ. Prot. 5 (17) (2014) 1630, https://doi.org/10.4236/jep.2014.517154.

[15] K. Patel, M. Desai, C. Panchal, B. Rehani, p-type transparent NiO thin films by e-beam evaporation techniques, Journal of Nano-and Electronic Physics 3 (1) (2011) 376.
[16] H.-L. Chen, Y.-M. Lu, W.-S. Hwang, Characterization of sputtered NiO thin films, Surf. Coat. Technol. 198 (1–3) (2005) 138–142, https://doi.org/10.1016/j.surfcoat.2004.10.032.
[17] I. Porqueras, E. Bertran, Electrochromic behaviour of nickel oxide thin films deposited by thermal evaporation, Thin Solid Films 398 (2001) 41–44, https://doi.org/10.1016/S0040-6090(01)01301-3.
[18] D. Franta, B. Negulescu, L. Thomas, P.R. Dahoo, M. Guyot, I. Ohlídal, J. Mistrík, T. Yamaguchi, Optical properties of NiO thin films prepared by pulsed laser deposition technique, Appl. Surf. Sci. 244 (1–4) (2005) 426–430, https://doi.org/10.1016/j.apsusc.2004.09.150.
[19] A. Al-Ghamdi, W.E. Mahmoud, S. Yaghmour, F. Al-Marzouki, Structure and optical properties of nanocrystalline NiO thin film synthesized by sol–gel spin-coating method, J. Alloy. Comp. 486 (1–2) (2009) 9–13, https://doi.org/10.1016/j.jallcom.2009.06.139.
[20] M. Jlassi, I. Sta, M. Hajji, H. Ezzaouia, Optical and electrical properties of nickel oxide thin films synthesized by sol–gel spin coating, Mater. Sci. Semicond. Process. 21 (2014) 7–13, https://doi.org/10.1016/j.mssp.2014.01.018.
[21] M. Martini, G. Brito, M. Fantini, A. Craievich, A. Gorenstein, Electrochromic properties of NiO-based thin films prepared by sol–gel and dip coating, Electrochim. Acta 46 (13–14) (2001) 2275–2279, https://doi.org/10.1016/S0013-4686(01)00396-6.
[22] M. Ristova, J. Velevska, M. Ristov, Chemical bath deposition and electrochromic properties of NiO_x films, Sol. Energy Mater. Sol. Cells 71 (2) (2002) 219–230, https://doi.org/10.1016/S0927-0248(01)00061-7.
[23] R.A. Ismail, S. Ghafori, G.A. Kadhim, Preparation and characterization of nanostructured nickel oxide thin films by spray pyrolysis, Appl. Nanosci. 3 (6) (2013) 509–514, https://doi.org/10.1007/s13204-012-0152-2.
[24] P. Shankar, J.B.B. Rayappan, Gas sensing mechanism of metal oxides: the role of ambient atmosphere, type of semiconductor and gases - a review, Sci. Lett. J 4 (2015) 126.
[25] C. Garzella, E. Comini, E. Tempesti, C. Frigeri, G. Sberveglieri, mathtotext>TiO_2 thin films by a novel sol–gel processing for gas sensor applications, Sens. Actuators B Chem. 68 (1–3) (2000) 189–196, https://doi.org/10.1016/S0925-4005(00)00428-7.
[26] T. Schneller, R. Waser, M. Kosec, D. Payne, Chemical Solution Deposition of Functional Oxide Thin Films, Springer, 2013, https://doi.org/10.1007/978-3-211-99311-8.
[27] P. Baraldi, Thermal behavior of metal carboxylates: III-metal acetates, Spectrochim. Acta A Mol. Spectrosc 38 (1) (1982) 51–55, https://doi.org/10.1016/0584-8539(82)80176-1.
[28] I. Sta, M. Jlassi, M. Hajji, H. Ezzaouia, Structural, optical and electrical properties of undoped and Li-doped NiO thin films prepared by sol–gel spin coating method, Thin Solid Films 555 (2014) 131–137, https://doi.org/10.1016/j.tsf.2013.10.137.
[29] S. Akinkuade, B. Mwankemwa, J. Nel, W. Meyer, Structural, optical and electrical characteristics of nickel oxide thin films synthesised through chemical processing method, Phys. B Condens. Matter 535 (2018) 24–28, https://doi.org/10.1016/j.physb.2017.06.021.
[30] G. Zhang, L. Yu, H.E. Hoster, X.W.D. Lou, Synthesis of one-dimensional hierarchical NiO hollow nanostructures with enhanced supercapacitive performance, Nanoscale 5 (3) (2013) 877–881, https://doi.org/10.1039/c2nr33326k.
[31] S. Shariffudin, M. Mamat, S. Herman, M. Rusop, Influence of drying temperature on the structural, optical, and electrical properties of layer-by-layer ZnO nanoparticles seeded catalyst, J. Nanomater. 2012 (2012) 122, https://doi.org/10.1155/2012/359103.
[32] E. Cazzanelli, A. Kuzmin, G. Mariotto, N. Mironova-Ulmane, Study of vibrational and magnetic excitations in $Ni_cMg_{1-c}O$ solid solutions by Raman spectroscopy, J. Phys. Condens. Matter 15 (12) (2003) 2045, https://doi.org/10.1088/0953-8984/15/12/321.
[33] D. Raoufi, A. Taherniya, The effect of substrate temperature on the microstructural, electrical and optical properties of Sn-doped indium oxide thin films, Eur. Phys. J. Appl. Phys. 70 (3) (2015) 30302, https://doi.org/10.1051/epjap/2015150004.
[34] M. Sultan, N. Sultana, Analysis of reflectance and transmittance characteristics of optical thin film for various film materials, thicknesses and substrates, J. Electr. Electron. 4 (3) (2015) 1, https://doi.org/10.4172/2332-0796.1000160.
[35] M. Singh, M. Goyal, K. Devlal, Size and shape effects on the band gap of semiconductor compound nanomaterials, Journal of Taibah University for Science 12 (4) (2018) 470–475, https://doi.org/10.1080/16583655.2018.1473946.
[36] J.B. Mooney, S.B. Radding, Spray pyrolysis processing, Annu. Rev. Mater. Sci. 12 (1) (1982) 81–101, https://doi.org/10.1146/annurev.ms.12.080182.000501.

6.4 Fabrication of Al/p-NiO Shottky diodes on p-Si

The electrical properties of Al/p-NiO Shottky diodes formed on p-Si are presented in this section. The experimental procedures were as discussed in section 4.2.3

Figure 6.3, shows the structural and microstructural properties of the film. Figure 6.3(b) reveals that the films were granular. The scanning probe micrograph of a 2 μm $\times$ 2 μm area, Figure 6.3(c), shows the topography of the film. The root-mean-square value of the surface roughness of the film was found to be 2.79 nm. The cross-sectional FESEM image of the film (Figure 6.3(d)) indicates that the film was uniform in thickness with an average thickness of 308 nm $\pm$ 8 nm as measured on the micrograph, taking an average of six measurements.

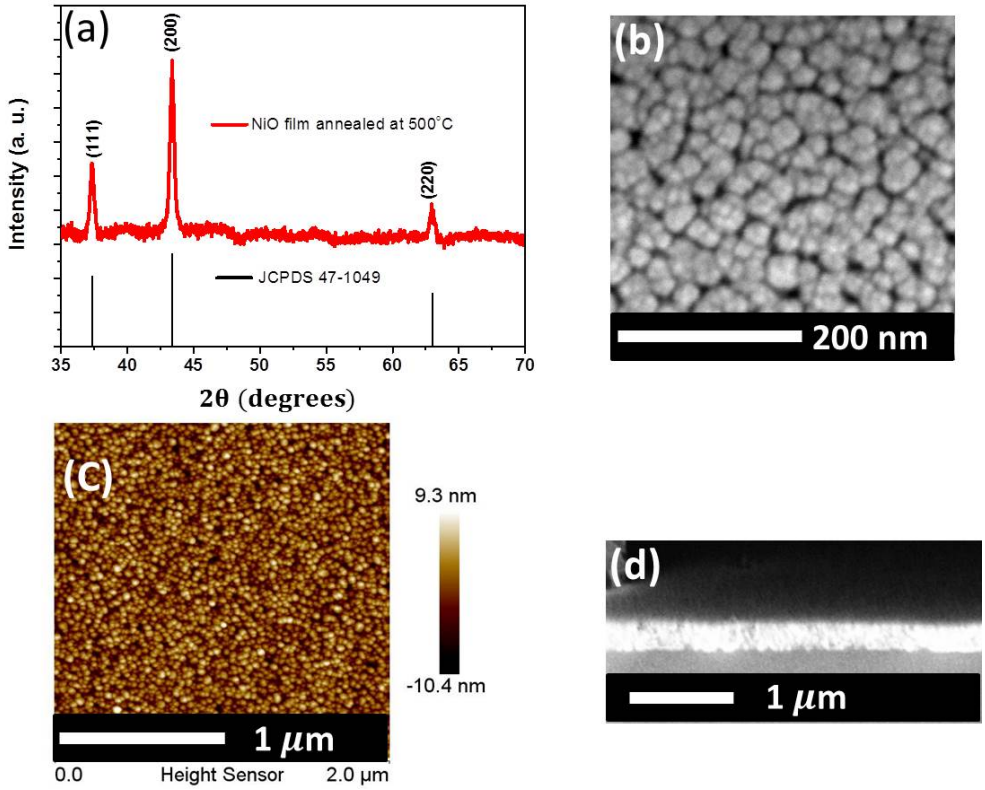

Figure 6.3: (a) XRD pattern of a NiO thin film deposited on glass, (b) FESEM image, (c) SPM image (2 μm $\times$ 2 μm), and (d) cross-sectional image of the film.

The current–voltage characteristics for forward and reverse bias of the Al/NiO diode on p-type silicon, as measured in the dark at a temperature of 300 K and plotted as a semilog graph is shown in Figure 6.4. The rectification ratio of the diode at 2.0 V was found to be 3×10^2.

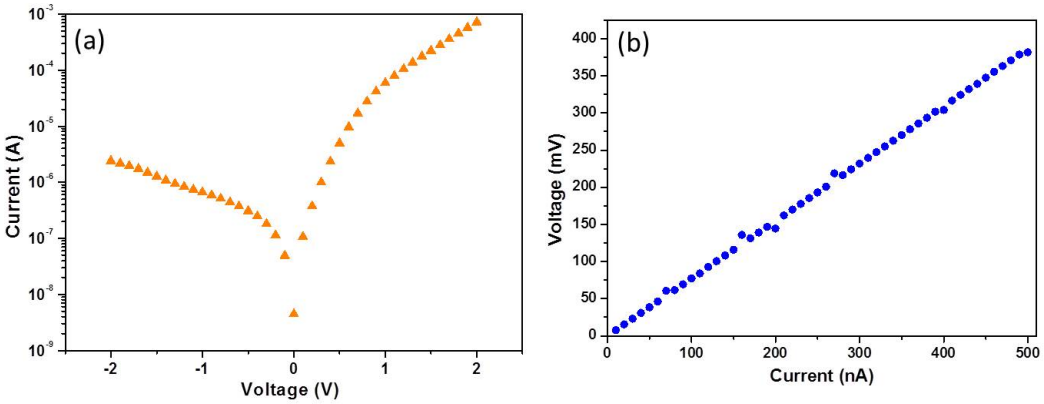

Figure 6.4: (a) I–V characteristics of the Al/NiO junction and (b) V–I plot from the resistivity measurement.

The net current through the diode, due to thermionic emission can be obtained from Equation 2.47. When the series resistance of the diode is taken into consideration, the voltage across the junction becomes: $V - IR_s$, where R_s is the series resistance.

Values of the ideality factor, n, the saturation current, I_s, and the series resistance were obtained from the semilog graph by fitting the curve above $\frac{3kT}{q}$. The zero-bias barrier height, Φ_B, was obtained from:

$$I_s = AA^*T^2e^{\frac{-q\Phi_B}{kT}} \tag{6.1}$$

Where A, is the effective diode area, A^*, is the effective Richardson constant which is 32 cm^2K^2 for Si [3].

The average values of these parameters obtained from the measurement are summarized in Table 6.2

Table 6.2: Table showing I_s, n, Φ_B, and r_s of the Al/NiO Schottky diodes on p-silicon.

Saturation current (I_s)	Ideality factor (n)	Schottky barrier height (Φ_B)	Series resistance (R_s)
1.28×10^{-8} A	3.8	0.7 eV	1.45 kΩ

The average value of n that was obtained for the diode was higher than what is expected of an ideal diode. This may be due to the presence of interface states between aluminium and NiO [4] or presence of high density of traps common in heterojunctions that are formed from materials with large lattice mismatch [5] or barrier inhomogeneities [6]. The series resistance of the Schottky diode was high, this may be due to the high resistivity of the NiO film.

The band structure of the aluminium-NiO contact according to Anderson model, is shown in Figure 6.5. The value of Schottky barrier height calculated from the band structure, $\Phi_B = 0.68$ eV, was close to the fitted value, $\Phi_B = 0.7$ eV.

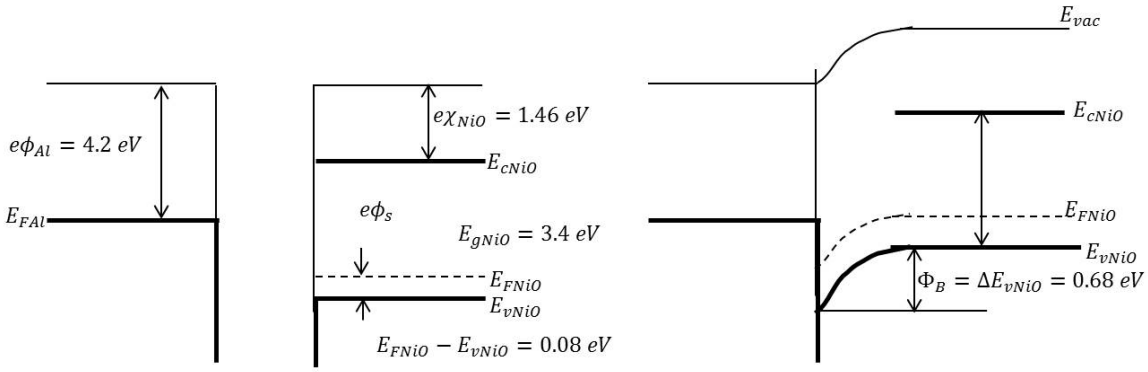

Figure 6.5: The band structure of Al/NiO junction based on the Anderson model [7].

6.5 Summary and conclusions

NiO thin films that were produced using the sol-gel spin coating method, from 0.1 M and 0.2 M precursor solutions were granular according to SEM images but the XRD results showed that they were amorphous. Thus the formation of NiO on the substrates could not be established. 0.75 M solution was found to produce polycrystalline films. The intensity of diffraction peaks were found to increase with the number of layers deposited on the substrates. The effects of processing temperature on the properties of the films shows that the crystallinity of the films increased with annealing temperature. Films that were dried at 160 °C showed less crystallinity when compared with other films that were dried at higher temperatures. Films that were annealed at 300 °C, irrespective of the drying temperatures also showed poor crystallinity. Morphology of the films revealed that they were made of grains of uniform size, the grain size increased from about 14 nm to 28 nm for films that were dried at 200 °C and 14 nm to 32 nm for films dried at 250 °C as the temperature of annealing was increased from 400 °C to 600 °C. There was no significant change in transmittance as a function of the drying temperature. Raman spectra of the films show that two prominent Raman peaks at 558 cm^{-1} and 1100 cm^{-1} for one-phonon first-order longitudinal-optical (1P) LO mode and two-phonon second-order longitudinal-optical mode (2P) 2LO respectively are found in all the films. For films that were annealed at 500 °C and 600 °C, and were dried at lower temperatures, enhancement of peak at

558 cm^{-1} ((1P) LO mode) over 1100 cm^{-1} ((2P) 2LO mode) was observed, indicating that these films are richer in defects than those dried at higher temperature. The electrical resistivity of the films as measured using the linear four-point probe system shows that the resistivity decreases with increasing drying temperature, the minimum resistivity was obtained in all the films after annealing at 500 °C. The resistivity of the films depends on both the grain size and the crystallinity of the films. Annealing above 500 °C reduces the concentration of defects in the films, and this resulted in an increase in the resistivity.

The I–V measurements for Al/p-NiO on silicon indicated a rectifying property, meaning a Schottky diode was formed between aluminium and NiO, the rectification ratio of the diode at 2.0 V was found to be 3×10^2. The saturation current, ideality factor, series resistance and Schottky barrier height of the Schottky diode were found to be 1.28×10^{-8} A, 3.8, 1.454 kΩ and 0.7 eV respectively.

References

[1] Masamichi Sato and Itsuo Fujii. Spin coating process, September 12 1978. US Patent 4,113,492.

[2] Theodor Schneller, Rainer Waser, Marija Kosec, and David Payne. *Chemical solution deposition of functional oxide thin films*. Springer, 2013.

[3] Simon M Sze and Kwok K Ng. *Physics of Semiconductor Devices*. John Wiley & Sons, 2006.

[4] Cevdet Coskun, Nebi Gedik, and Ercan Balcı. The effect of high-energy electron irradiation on ZnO-based ohmic and Schottky contacts. *Semiconductor Science and Technology*, 21(12):1656, 2006.

[5] Anisha Gokarna, NR Pavaskar, SD Sathaye, V Ganesan, and SV Bhoraskar. Electroluminescence from heterojunctions of nanocrystalline CdS and ZnS with porous silicon. *Journal of Applied Physics*, 92(4):2118–2124, 2002.

[6] Subhash Chand and Saroj Bala. Analysis of current–voltage characteristics of inhomogeneous Schottky diodes at low temperatures. *Applied Surface Science*, 252(2):358–363, 2005.

[7] Richard L Anderson. Experiments on Ge-GaAs heterojunctions. In *Electronic Structure of Semiconductor Heterojunctions*, pages 35–48. Springer, 1988.

Article under review

1. **Shadrach T. Akinkuade**, Walter E. Meyer, Jacqueline M. Nel, Characterization of aluminium Schottky diodes fabricated on nickel oxide thin film synthesized by the sol-gel method, *Thin solid Films*

Chapter 7

Results: Deposition of NiO thin films using spray pyrolysis

7.1 Introduction

A custom-built spray pyrolysis system was used to produce thin films of nickel oxide on glass substrates. The effects of concentration of the precursor, the number of spraying cycles, and annealing on the structural, optical and electrical properties of the films were studied. The conditions for fabricating NiO films were optimised for minimum sheet resistance. The films were doped with Li^{+} and the properties of the films were studied. The results of the studies are discussed in this chapter.

7.2 Properties of NiO thin films synthesized using a custom-built spray pyrolysis system

The films were deposited as discussed in section 4.2.5. The effects of concentration of precursor, number of spraying cycles and motion of the nozzle on the properties of the films are presented in this section.

7.2.1 Structural properties

The XRD patterns of the films are shown in Figures 7.1 and 7.2, the patterns were indexed to (JCPDS 47-1049). There are diffraction peaks at 37.24°, 43.23° and 62.88° which correspond to (111), (200), and (220) diffraction planes respectively. This pattern confirms the face centred cubic structure of nickel oxide. In all the patterns, the peak at $2\theta = 37.24°$ was the most prominent. This was in contrast to the XRD pattern of NiO thin films deposited through spin-coating method in which the highest diffraction peak was in the (200) crystallographic plane [1]. The intensities of the XRD peaks were found to increase with the number of spraying cycles for all the concentrations of the precursor. Figure 7.1(a) shows the trend in films that were prepared from 0.05 M solution for the different number of cycles and annealed at 500 °C . Similarly, Figure 7.1(b) shows that an increase in the concentration of the precursor solution enhanced the crystallinity of the films. Diffraction peaks in other planes can be seen in the XRD pattern at concentrations above 0.05 M. The influence of annealing and the mode of spraying on the structural properties of the films was shown in Figure 7.2(a) and (b) respectively. From these figures, it is clear that annealing improved the crystallinity of the films because the peaks were more intense and narrower compared to the peaks of the as-deposited films. The increase in the intensity of the peaks was as a result of continual formation of NiO during the annealing process. The increase in the intensity of the (111) peak can be ascribed to the increase in the number of crystallites diffracting the X-rays from the (111) plane. This also implies that there was preferred orientation of the particles in the thin film, which continued with additional layers.

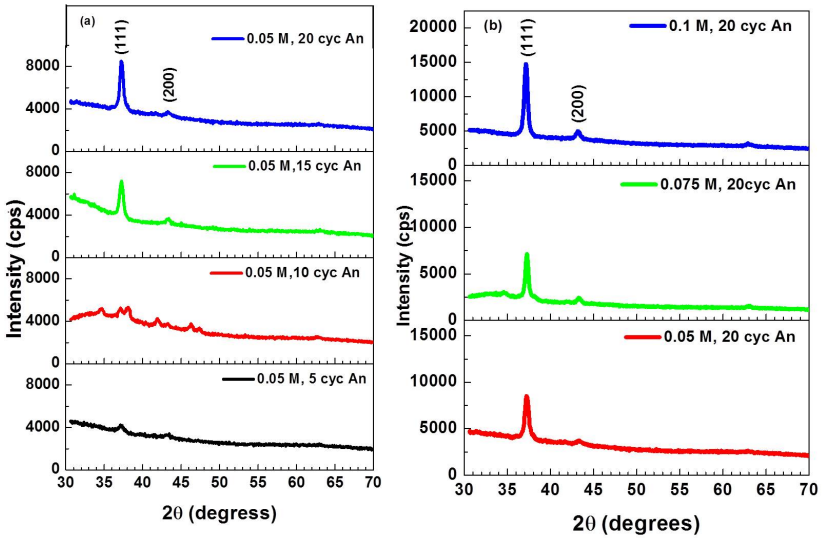

Figure 7.1: XRD pattern of NiO thin films (a) prepared from a 0.05 M solution using a different number of cycles, and (b) prepared from different concentrations at 20 cycles, after annealing at 500 °C.

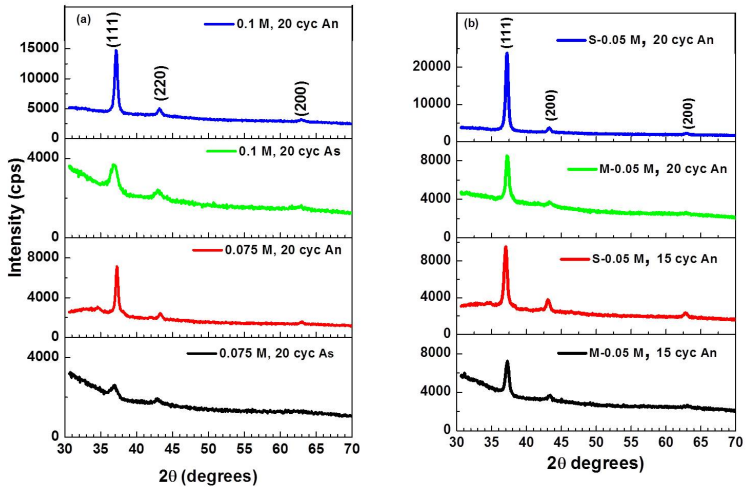

Figure 7.2: XRD pattern of (a) as-deposited (As) and annealed (An) films from 0.075 M and 0.1 M solutions and (b) films prepared from 0.05 M solution at 15 and 20 cycles for stationary (S) and moving (M) nozzle modes of spraying.

The interplanar spacing, lattice parameter, and crystallite size of NiO in the films that were deposited under different conditions were calculated using Equations 4.4, 4.5, and 4.6 respectively. The results are shown in Table 7.1.

Table 7.1: Table showing the d-spacing and lattice constants of the NiO thin films compared to JCPDS 65-2901

Conc. (M)	No. of cycles and conditions	$2\theta_{(111)}$ (°)	$d_{(111)}$ (nm)	$a_{(111)}$ (nm)	$D_{(111)}$ (nm)
0.05	15^{s}_{An}	37.07	0.2425	0.4200	18.67
0.05	15^{m}_{An}	37.26	0.2413	0.4179	15.65
0.05	20^{s}_{An}	37.20	0.2417	0.4186	19.47
0.05	20^{m}_{An}	37.28	0.2412	0.4177	16.23
0.075	20^{s}_{As}	37.00	0.2429	0.4208	8.42
0.075	20^{s}_{An}	37.29	0.2411	0.4176	22.47
0.1	20^{s}_{As}	36.96	0.2432	0.4202	8.26
0.1	20^{s}_{An}	37.18	0.2418	0.4188	19.05

^{s}stationary nozzle, ^{m}moving nozzle, $_{As}$ As-deposited, $_{An}$ Annealed

7.2.2 Morphological properties

Figures 7.3 shows the surface morphology of the annealed films. The films were obtained from spraying precursor solutions of different concentrations in 20 cycles. The grains of NiO thin films were found to increase in size as the concentration was increased. The films were more porous at low concentration of precursor and fewer spraying cycles. Figure 7.4 shows the morphology of films produced from 10 cycles of spraying from 0.075 M and 0.1 M solutions after annealing at 500 °C. An improvement in the

compactness can be noticed as the concentration of the precursor solution was increased. The reason for the observed improvement in compactness of the film might be that at low concentration, with few cycles of spraying, the surface of the substrate was not well covered by the NiO precursor. Increasing concentration enhances the agglomeration of the nanoparticles over the whole surface of the substrate. The movement of the nozzle across the film during spraying caused droplets of the solution to move relative to the stationary substrate. At the point of impact on the substrate, the spherical droplets were deformed and overlapped one another (Figure 7.3(a)). The morphology of the film produced from 0.05 M solution with a stationary nozzle, Figure 7.4(c), shows more distinct grains. This could be responsible for the enhancement of the intensity of the peaks in the XRD patterns in Figure 7.2(b).

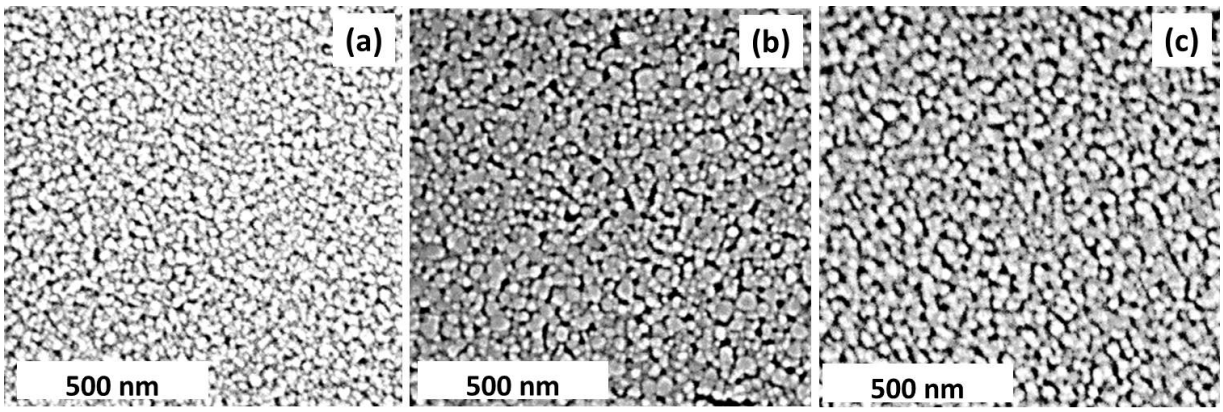

Figure 7.3: SEM images of films deposited with the nozzle moving from 20 cycles of (a) 0.05 M (b) 0.075 M and (c) 0.1 M solutions after annealing at 500 °C.

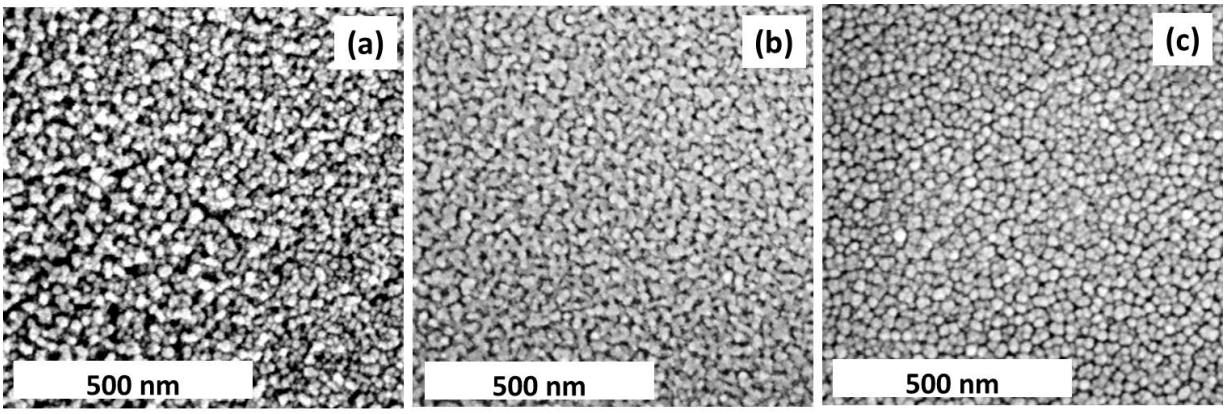

Figure 7.4: SEM images of films deposited from 10 cycles of (a) 0.075 M (b) 0.1 M, with the nozzle moving, and (c) 20 cycles of 0.05 M solution with stationary nozzle. All films were annealed at 500 °C

7.2.3 Optical properties

Transmittance spectra of the films are shown in Figure 7.5. The optical transmittance of films that were fabricated from 0.1 M solution decreased from 80% to about 50% at 650 nm as the concentration of solution was increased. The transmittance of the films at 300 nm were 26.9%, 23.4% and 12.3% for films that were made from 5, 10, and 15 cycles of spraying, respectively. This was an indication that the films were very thin and highly transparent. Generally, the transmittance of the films decreased with increase in the number of spraying cycles, meaning that the optical path length in the films was increasing with number of spraying cycles because more material was deposited on the substrate.

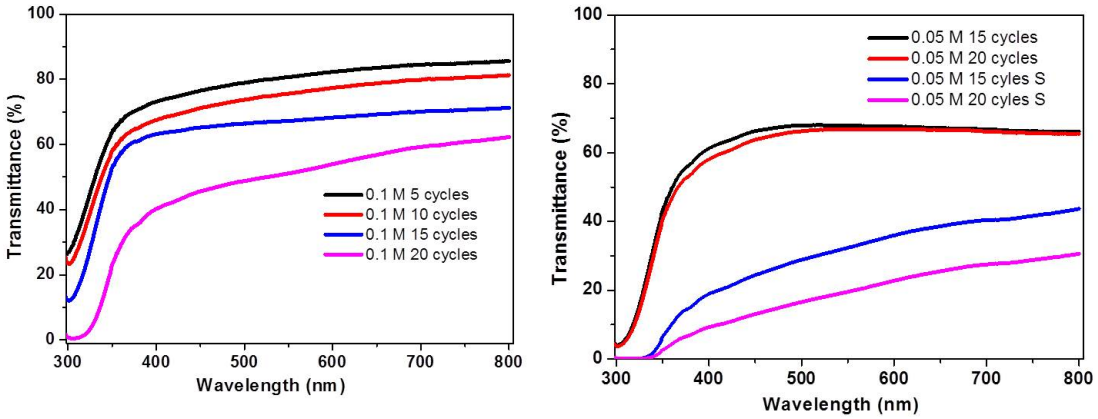

Figure 7.5: Transmittance spectra of NiO films deposited using (a) 0.1 M (b) 0.05 M solutions.

The Raman spectra of the films are shown in Figure 7.6. Two vibrational bands of NiO due to one-phonon and two-phonon vibrations were seen in the spectra. The peaks of the band centred at 501 cm^{-1} may be ascribed to the first-order one-phonon transverse- and longitudinal-optical (1P:TO and LO) modes. These result from symmetry-breaking imperfections such as nickel vacancies in the structure of NiO. A similar Raman peak was observed by Nel *et al.* [2]. The Raman peak at 1099 cm^{-1} is attributed to the two-phonon second-order longitudinal-optical (2P:2LO) mode. These Raman peaks are typical of NiO [3]. An increase in the intensity of the 1P (LO) peaks with increasing concentration of the solution indicates that the density of nickel vacancies increased with an increase in the concentration of the solution. The intensity of Raman peaks in the annealed films were higher when compared with the as-deposited films, meaning that annealing caused the transformation of the precursor to NiO since the intensity of Raman peaks depends on concentration [4]. Other Raman peaks in the spectra are at 798 cm^{-1} and 953 cm^{-1}, which are associated with (2P:2TO) and (2P:TO+LO) respectively [3].

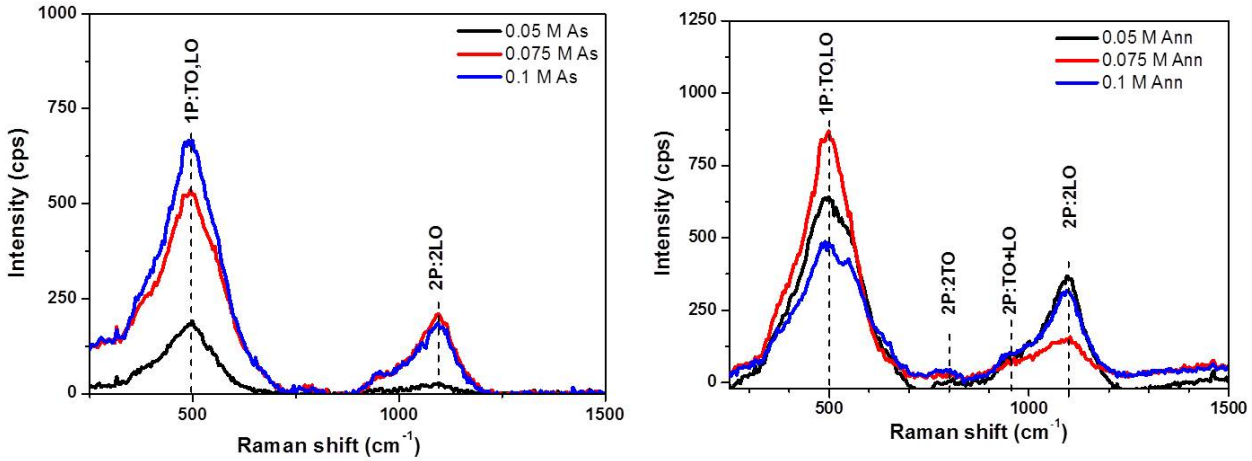

Figure 7.6: Raman spectra of (a) as-deposited and (b) annealed films.

7.2.4 Electrical properties

The voltage–current (V–I) plot that was obtained from a linear four-point probe is shown in Figure 7.7. The measurement was performed on the as-deposited and annealed films obtained from 20 cycles of spraying different concentrations of the precursor. The sheet resistance was calculated from: $R_s = \frac{\pi}{ln(2)}(\frac{V}{I})$ [5], where $\frac{V}{I}$ is the ratio of voltage measured between the inner probes to the current flowing in the outer probes. The average value of this ratio was obtained from the gradient of the V–I plot. Values of calculated sheet resistance of the films are shown in Table 7.2. The sheet resistance of the films was found to decrease with increasing concentration of the precursor. The film deposited from 0.1 M solution had the least sheet resistance- this was due to less scattering of carriers at the grain

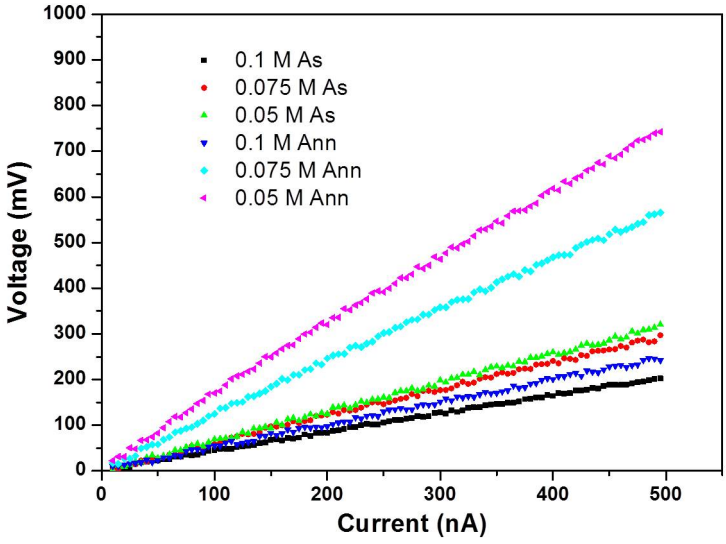

Figure 7.7: V–I plot measured by a linear four-point probe measurement.

boundaries because of larger grains as shown in Figure 7.3.

Table 7.2: Sheet resistance of the films.

Concentration	0.05 M		0.075 M		0.1 M	
Conditions	As-dep	Ann	As-dep	Ann	As-dep	Ann
Sheet resistance (MΩ/sq)	2.86	6.42	2.67	4.92	1.79	2.17

The sheet resistance of the films after annealing increased. John and Shirley [6] ascribed this to better stoichiometry of the films, which leads to a reduction in the number of defects within the lattice of the NiO thin films, a similar result had been reported for NiO thin films fabricated using pulse-laser-deposition method [7].

7.3 Properties of Li-doped NiO thin films synthesized by spray pyrolysis

7.3.1 Structural properties

The XRD patterns of the Li-doped and undoped NiO films are given in Figure 7.8(a). The XRD peaks of the doped NiO films in the figure were indexed to JCPDS file number 65-2901 of NiO. The peaks were centred at 37.12°, 43.13° and 62.64°, and they correspond to (111), (200) and (220) diffraction planes, respectively of face-centred cubic structure of NiO. There were no other diffraction peaks in the pattern, thus confirming that other phases such as lithium or its oxides were not formed to detectable amounts in the film. It also showed that the Li^+ ions are adequately substituted in Ni^{2+} positions in the lattice. The intensity of the (200) peak was found to increase with increase in concentration of lithium, this implies that there was an improvement in the crystalline quality of the films.

The interplanar spacing (d-spacing of) and lattice parameter, a, and the mean crystallite size, D_{mean}, of the NiO films were calculated from data obtained from diffraction along (111) and (200) planes using Equations 4.4, 4.5, and 4.6. The results are given in Table 7.3. There was no significant difference between the d-spacing and lattice parameter of the films when compared with the JCPDS file.

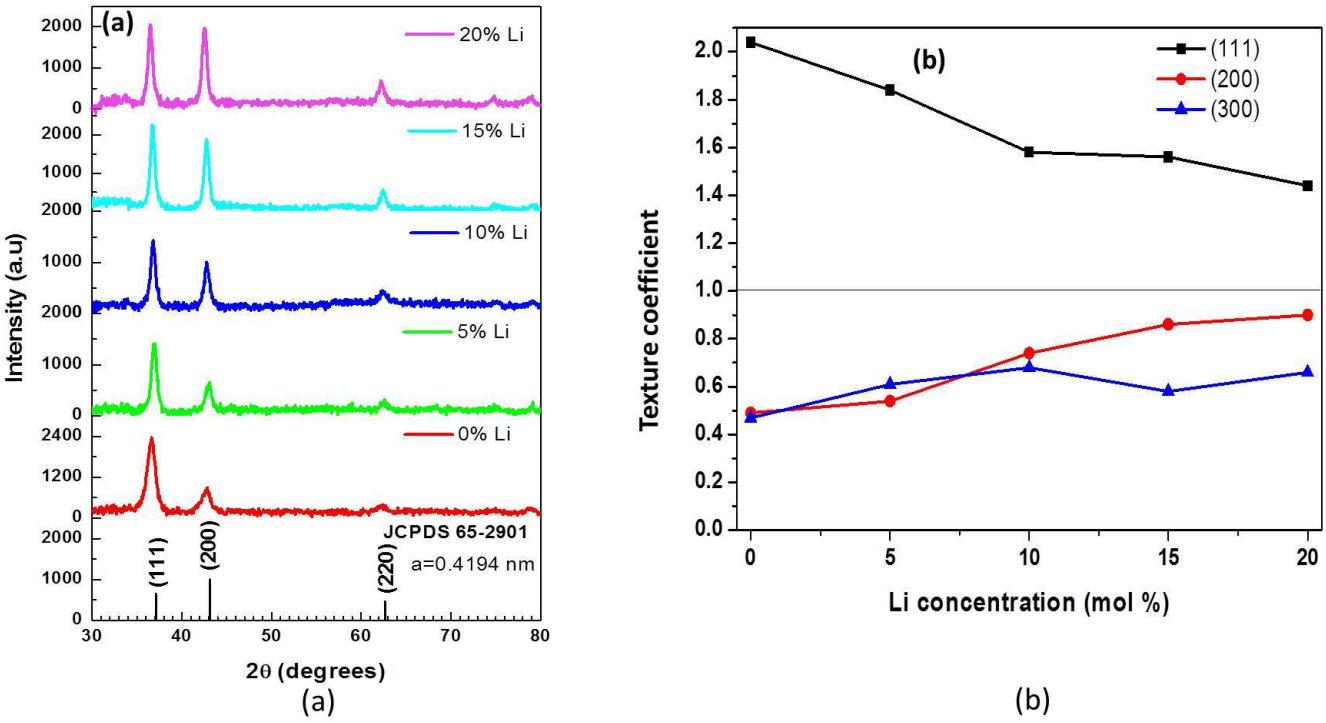

Figure 7.8: (a) XRD patterns of the undoped and Li-doped NiO thin films on glass substrates, (b) dependence of the texture coefficient on concentration of Li^+ ions after annealing at 500 °C.

Table 7.3: *d*-spacing and lattice constants of the NiO thin films compared with JCPDS 65-2901

Concentration of Li (mol%)	(hkl)	2θ (°)	d (nm)	a (nm)	D_{mean} (nm)
0	111	36.86	0.2451	0.4246	7.83
	200	42.88	0.2109	0.4218	
5	111	36.95	0.2432	0.4212	11.33
	200	43.18	0.2106	0.4211	
10	111	36.82	0.2441	0.4228	13.17
	200	42.88	0.2109	0.4218	
15	111	36.66	0.2451	0.4246	14.36
	200	42.88	0.2109	0.4218	
20	111	36.86	0.2451	0.4246	13.63
	200	42.66	0.2120	0.4239	
JCPDS 65-2901	111	37.12	0.2422	0.4194	–
	200	43.13	0.2097	0.4194	

There was no noticeable shift in the position of diffraction peaks, this is an indication that Li^+ ions are adequately substituted in Ni^{2+} positions in the lattice. This agrees with the result reported by Joseph *et al.* [8]. The (111) diffraction peaks were the most prominent in the XRD pattern of the undoped film. The intensity of this peak was found to decrease as the doping concentration was increased. Concurrently, there was a gradual increase in the intensity of the (200) peak. At 20% doping

concentration, the intensity of the (111) and (200) peaks were almost equal. The observed change in intensity of (111) and (200) peaks was in contrast to earlier reports on structural properties of lithium doped NiO films prepared through spray pyrolysis. Wu and Yang [9] reported that the intensity of the (111), (200), and (220) diffraction peaks increased with increasing lithium concentration from 0 at% to 10 at%. On the other hand Hassan *et al.* [10] observed that only the (111) diffraction peak increased as lithium concentration was increased, with the maximum amplitude at 50 at%.

Quantitative information concerning the preferential orientation of the crystallites in the films was obtained from the texture coefficient (T_c). The T_c is unity when there is no preferential orientation of the crystallites, the value is greater than unity when the crystals are oriented in a particular direction [11]. T_c of the films was calculated from the Equation 4.7: The texture coefficients of the films are presented in Table 7.4. The dependence of texture coefficient on the concentration of Li^+ is shown in Figure 7.8(b).

Table 7.4: Texture coefficients of the films in (111), (200) and (220) planes

Planes (*hkl*)	0 %Li	5 %Li	10 %Li	15 %Li	20 %Li
111	2.04	1.84	1.58	1.56	1.44
200	0.49	0.54	0.74	0.86	0.90
220	0.47	0.61	0.68	0.58	0.66

The preferred crystallographic orientation of the films was in (111) plane, there was a gradual increase in the texture coefficient of the films along (200) plane with increasing concentration of lithium. This finding is in contrast to some reports that have appeared in literature, where Li-doped thin films of NiO are usually (111) oriented with a change in preferred orientation with doping [8]. The formation of NiO depends on the repulsive forces between O^{2-} and electrostatic energy of Ni–O pairs [12]. In the films, O^{2-} are arranged in the densely packed (111) plane. This orientation reduces the surface free energy of crystals. In the (111) oriented films, O^{2-} and Ni^{2+} are arranged in alternate layers [13]. The doping of the films with Li can be said to have facilitated the arrangement of O^{2-} and Ni^{2+} simultaneously in the same plane, thereby encouraging growth on the (200) crystallographic plane.

7.3.2 Morphological properties

The scanning electron micrographs of 5 mol% to 20 mol% Li-doped NiO films are shown in Figure 7.9. The surface morphology reveals that the films have uniform growth on the substrates without

cracks and the substrates were well covered by particles of the films. The nanoparticles were found to be uniformly distributed in the 5% Li-doped film, while there was agglomeration of particles, at a nanoscale, on the films as the percentage of doping was increased. The agglomeration of particles resulted in grains. The size of the grains was found to increase with percentage of doping. This might be responsible for improvement in crystallinity of the films as seen in the XRD results.

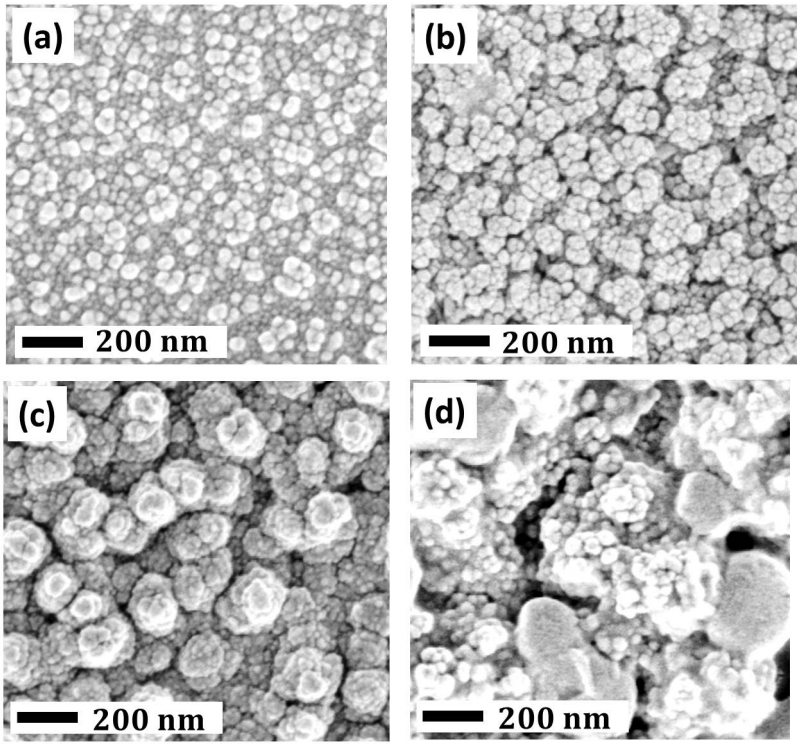

Figure 7.9: SEM images of (a) 5%, (b) 10%, (c) 15%, and (d) 20% Li-doped films.

The 3-D scanning probe micrographs (5 μm $\times$ 5 μm) of the films are shown in Figure 7.10. The root-mean-square roughness of the films were 12.5 nm, 21.3 nm, 22.4 nm, and 24.2 nm.

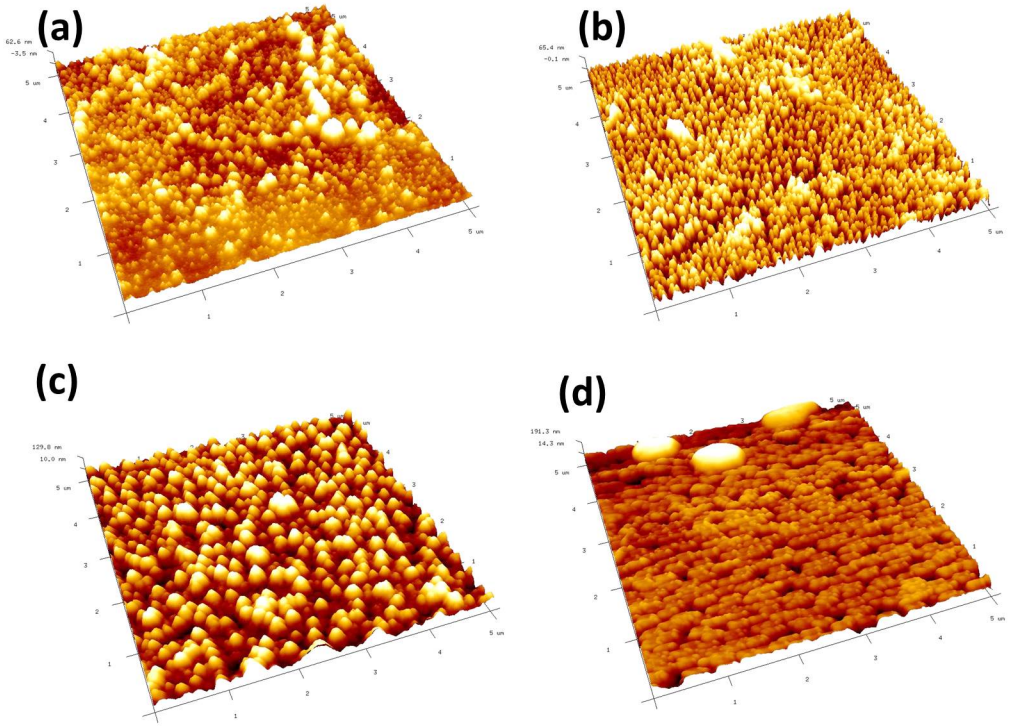

Figure 7.10: 3-D SPM images of (a) 5%, (b) 10%, (c) 15%, and (d) 20% Li-doped films.

7.3.3 Optical properties

The transmission spectra of the films are shown in Figure 7.11(a). The transmittance of the films was found to decrease with doping concentration. The 5% and 10% Li-doped films show higher transmittance compared to the 15% and 20% Li-doped films. The transmittance of the 5% and 10% Li-doped films varied from 72% to 49% in the visible range of the spectrum, but rapidly fell to zero at 310 nm. The transmittance of the 15% and 20% doped films decreased gradually from 48% and 37% respectively at 800 nm to zero at 330 nm.

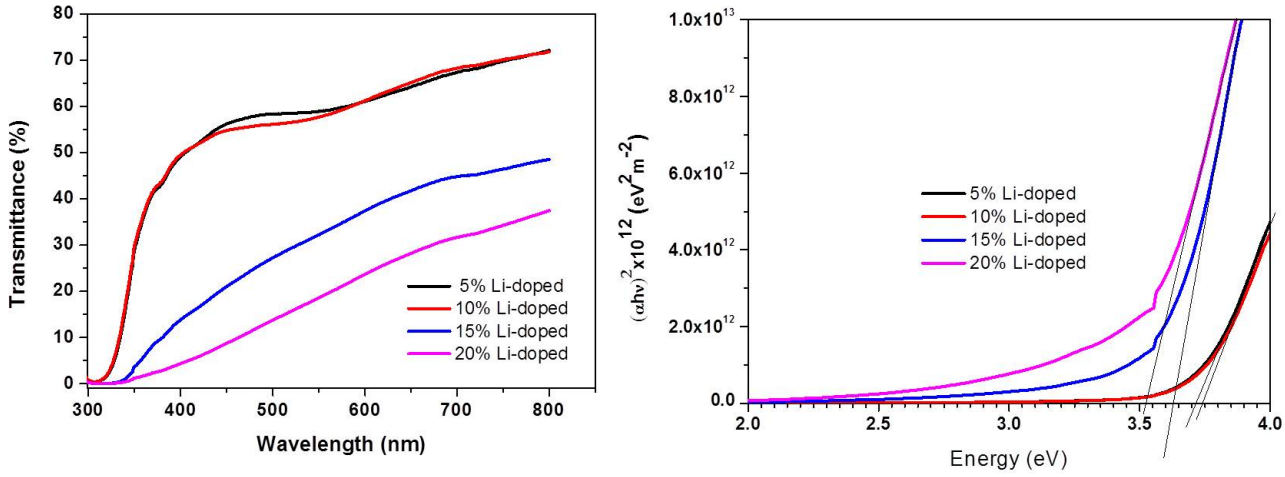

Figure 7.11: (a)Transmittance and (b) absorbance spectra of Li-doped NiO thin films.

The reduction in transmittance has been attributed to the increased presence of Ni^{3+} as the Li-dopant concentration increases [9]. The optical bandgaps of the films were estimated from the Tauc plot, shown in Figure 7.11(b). The optical bandgaps were found to be 3.74 eV, 3.71 eV, 3.63 eV, and 3.52 eV for 5 mol%, 10 mol%, 15 mol% and 20 mol% doped films respectively. The reduction in optical bandgap with increasing concentration of dopant was attributed to the presence of Li^{+} ions which act as the scattering centres.

The Raman spectra of the films are shown in Figure 7.12. The peaks of one-phonon first-order modes of vibration were seen at 487 cm^{-1} and 556 cm^{-1}, while the peaks of two-phonon second-order transverse and longitudinal modes of vibrations were found at 791 cm^{-1} and 1100 cm^{-1}, respectively. There was a broadening of the peaks of one-phonon first-order modes of vibration in the spectrum of the 5% Li-doped film. This is probably be due to the overlapping of the peaks of transverse optical order and longitudinal optical order. The peak intensity of the one-phonon mode increases with doping and was shifted to a lower wavenumber. The ratio of the intensity of the first-order one-phonon (1P:LO) vibration to the intensity of the second-order two-phonon 2P:2TO) was found to increase with concentration of lithium. This was an indication that the concentration of defects in the film was increasing as the doping percentage was increased, since the first-order LO phonon scattering in NiO was ascribed to nickel vacancy defects [14].

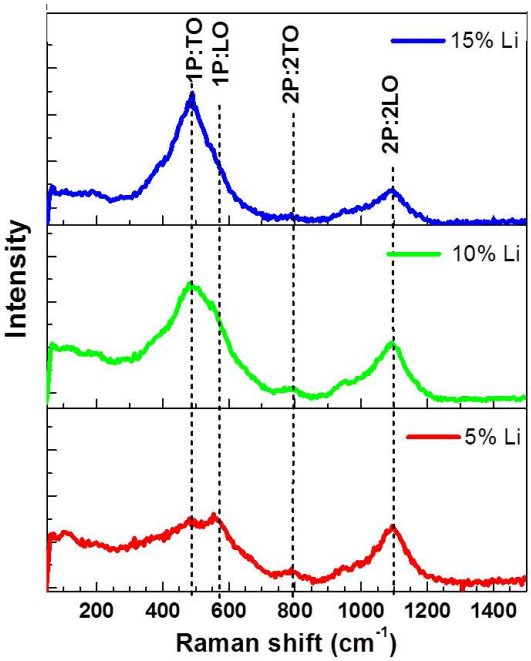

Figure 7.12: Raman spectra of Li-doped NiO thin films.

7.3.4 Electrical properties

The *V–I* plot from the linear four-point probe is shown in Figure 7.13(a). The figure shows that the voltage is proportional to current over the measurement range. The sheet resistance of the films were calculated using Equation 4.14 based on the slopes of the plots.

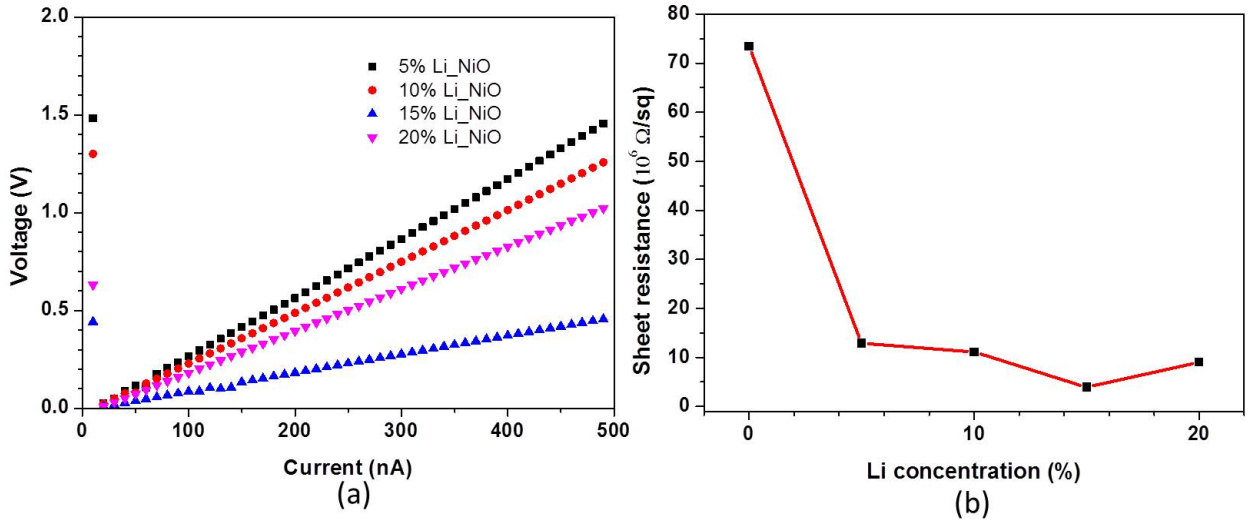

Figure 7.13: (a) The plots of voltage versus current obtained for the films, and (b) graph showing the dependence of sheet resistance on the concentration of Li.

The graph showing the variation of sheet resistance with concentration of lithium is shown in Figure

7.13(b). There was a significant change in the sheet resistance of the film due to doping. The sheet resistance changed from about 74 MΩ/sq to 18 MΩ/sq when the film was doped with 5 mol% of lithium. There was a further reduction to in sheet resistance to 4 MΩ/sq as the doping concentration increased to 15 mol%. At 20 mol% doping concentration, the sheet resistance increased to 9 MΩ/sq. Nickel vacancies are responsible for electrical conductivity in NiO, Joseph *et al.* reported that the addition of Li^+ leads to an increase in the concentration these defects in NiO thin films [8]. The sheet resistances in this study were less than those previously reported [8].

The observed trend in the sheet resistance of the films with doping concentration can be explained thus: initially Li^+ ions replace Ni^{2+} at the lattice points and Ni^{3+} ions are generated. This leads to an increase in the concentration of carriers and a reduction in the sheet resistance of the films, as the concentration of lithium is increased. However, at higher concentrations (above 15 mol% doping) interstitial Li^+ ions (which can not be detected by the XRD) might be found in the structure of the film. Such defects increase scattering of carriers or they could act as recombination centres or carrier traps in the films [15].

7.3.5 Figure of merit

Transparent conducting oxides (TCOs) are expected to have high optical transmittance in the visible range of electromagnetic spectrum and high electrical conductivity (low sheet resistance). These properties are usually inversely related [8] in TCOs. The figure of merit, the criterion or index, that summarizes the performance or quality of a TCO, was defined by Haake [16] as:

$$\phi = \frac{T_\lambda^q}{R_s} \tag{7.1}$$

where q is an exponent that determines which transmittance is required for a specific purpose, it has a value 10 for transmittance of 90% which is considered ideal for many applications, T_λ is the transmittance at a particular wavelength in the range 400 nm to 780 nm [17], and R_s is the sheet resistance of the film. The figure of merit was calculated at 550 nm for all the films, the variation of the figure of merit with the concentration of Li^+ is shown in Figure 7.14.

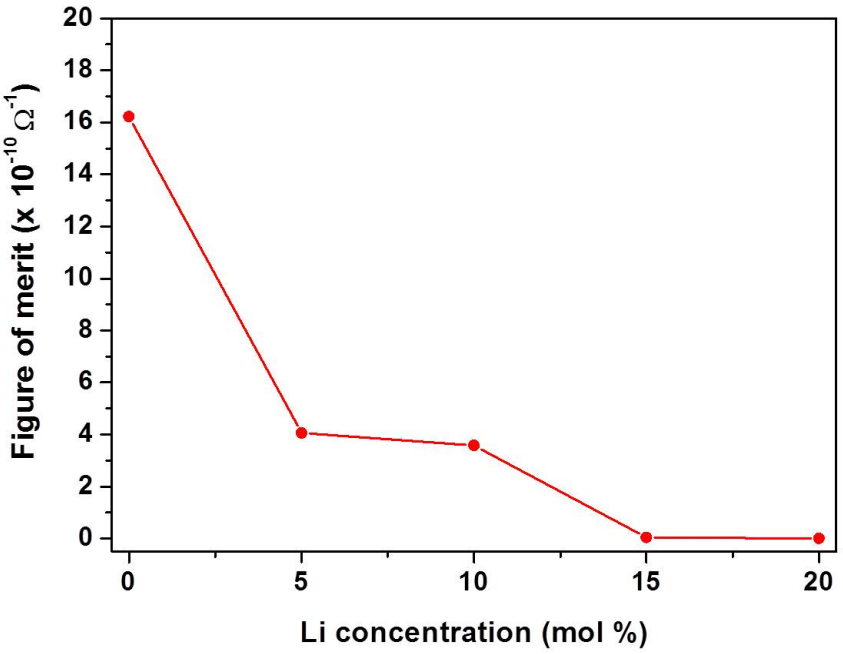

Figure 7.14: Relationship between the figure of merit of the films and the concentration of Li ions.

High optical transmission and low sheet resistance are expected of an ideal TCO. Contrary to this expectation, the figure of merit was found to decrease with an increase in the concentration of Li^+. Lu *et al.* was of the opinion that the presence of Ni^{3+} results in brown or black colouration in NiO thin films [18]. Therefore, the reduction in the transmittance of the Li-doped films might be associated with the formation of these ions as a result of doping. The sheet resistance of the Li-doped films was generally low compared to the undoped film, the transmittance was compromised as a result of doping. The undoped film had the highest figure of merit of 16 $\times$ 10^{-10} Ω^{-1} due to is higher transmittance while the figure of merits of the 5 mol% and 10 mol% Li-doped films were significantly lower but higher than the 15 mol% and 20 mol% Li-doped films. A similar figure of merit was reported for 5 mol% Li-doped film by Joseph *et al.* [8]. The optical and electrical properties of the undoped, 5 mol%, and 10 mol% Li-doped films, suggest that the material can be applied in smart windows and electromagnetic shielding applications that require high optical transmission and moderate electrical conduction.

7.4 Summary and conclusions

The crystallites in the films deposited using the spray pyrolysis as seen in the XRD results have preferred orientation in (111) crystallographic plane. Increasing the number of spraying cycles and concentrations of the precursor, and using a stationary nozzle and annealing results in an increase in the size of crystallites. This is evidenced by the increase in the amplitude of the (111) diffraction peak. The porosity of the films decreased as the number of spraying cycles and the concentrations of the precursor were increased. The movement of the nozzle across the substrate during spraying caused deformation of spherical shapes of droplets thereby causing grains to overlap as the film was formed. Two bands in the Raman spectra of the films were of vibrational origin, namely one-phonon (1P) and two-phonon (2P) vibrations. The sheet resistance of the films decreased with increasing precursor concentration and increased after annealing at 500 °C.

The lithium-doped NiO thin films fabricated using the spray pyrolysis method, using 5 mol%, 10 mol%, 15 mol%, and 20 mol% of Li^{2+} ions, exhibited less preferred orientation with a decrease in intensity of the (111) diffraction peak and an increase in the (200) peak as the doping concentration was increased. Optical studies revealed that the 5 mol% and 10 mol% Li-doped films were more transparent than films that were doped to a higher molar percentage, an indication that the films can be used as a transparent conductor. The sheet resistance of the films decreased when the concentration of dopant increased from 5% to 15%. There was an increase in the sheet resistance at 20% doping concentration. Raman spectra of the films indicated that NiO was formed on the substrates and that the concentration of nickel vacancies increased with doping.

References

[1] AA Al-Ghamdi, Waleed E Mahmoud, SJ Yaghmour, and FM Al-Marzouki. Structure and optical properties of nanocrystalline NiO thin film synthesized by sol–gel spin-coating method. *Journal of Alloys and Compounds*, 486(1-2):9–13, 2009.

[2] JM Nel, FD Auret, L Wu, MJ Legodi, WE Meyer, and M Hayes. Fabrication and characterisation of NiO/ZnO structures. *Sensors and Actuators B: Chemical*, 100(1-2):270–276, 2004.

[3] N Mironova-Ulmane, A Kuzmin, I Steins, J Grabis, I Sildos, and M Pärs. Raman scattering in nanosized nickel oxide NiO. *Journal of Physics: Conference Series*, 93(012039):1–5, 2007.

[4] John R Ferraro. *Introductory Raman Spectroscopy*. Elsevier, 2003.

[5] Dieter K Schroder. *Semiconductor material and device characterization*. John Wiley & Sons, 2006.

[6] John B Mooney and Shirley B Radding. Spray pyrolysis processing. *Annual Review of Materials Science*, 12(1):81–101, 1982.

[7] R Karsthof, P Räcke, H Von Wenckstern, and M Grundmann. Semi-transparent NiO/ZnO UV photovoltaic cells. *Phys. Status Solidi (a)*, 213(1):30–37, 2016.

[8] M Joseph, D Pauland Saravanan, B Muthuraaman, P Renugambal, S sambasivam, S Philip Raja, P Maruthamuthu, and C Venkateswaran. Spray deposition and characterization of nanostructured Li doped NiO thin films for application in dye-sensitized solar cells. *Nanotechnology*, 19(48):485707, 2008.

[9] Wu Chia-Ching and Yang Cheng-Fu. Investigation of the properties of nanostructured Li-doped NiO films using the modified spray pyrolysis method. *Nanoscale Research Letters*, 8(1):33, 2013.

[10] Hasan Azimi Juybari, Mohammad-Mehdi Bagheri-Mohagheghi, and Mehrdad Shokooh-Saremi. Nickel–lithium oxide alloy transparent conducting films deposited by spray pyrolysis technique. *Journal of Alloys and Compounds*, 509(6):2770–2775, 2011.

[11] GG Valle, Peter Hammer, Sandra Helena Pulcinelli, and Celso Valentim Santilli. Transparent and conductive ZnO: Al thin films prepared by sol-gel dip-coating. *Journal of the European Ceramic Society*, 24(6):1009–1013, 2004.

[12] CA Ventrice Jr, Th Bertrams, H Hannemann, A Brodde, and H Neddermeyer. Stable reconstruction of the polar (111) surface of NiO on Au. *Physical Review B*, 49(8):5773, 1994.

[13] Eiji Fujii, Atsushi Tomozawa, Hideo Torii, and Ryoichi Takayama. Preferred orientations of NiO films prepared by plasma-enhanced metalorganic chemical vapor deposition. *Japanese Journal of Applied Physics*, 35(3A):L328, 1996.

[14] V Gowthami, P Perumal, R Sivakumar, and C Sanjeeviraja. Structural and optical studies on nickel oxide thin film prepared by nebulizer spray technique. *Physica B: Condensed Matter*, 452:1–6, 2014.

[15] Wen Guo, KN Hui, and Kwan San Hui. High conductivity nickel oxide thin films by a facile sol–gel method. *Materials Letters*, 92:291–295, 2013.

[16] G Haacke. New figure of merit for transparent conductors. *Journal of Applied Physics*, 47(9):4086–4089, 1976.

[17] AA Solov'ev, NS Sochugov, KV Oskomov, and NA Zaharov. Properties of multilayer ZnO: Ga/Ag/ZnO: Ga coatings applied by magnetron sputtering. *Protection of Metals and Physical Chemistry of Surfaces*, 46(4):438–443, 2010.

[18] YM Lu, Weng-Sing Hwang, and JS Yang. Effects of substrate temperature on the resistivity of non-stoichiometric sputtered niox films. *Surface and Coatings Technology*, 155(2-3):231–235, 2002.

Chapter 8

Applications of the synthesised NiO films

8.1 Introduction

The spray pyrolysis method was used to fabricate a heterojunction between nickel oxide (NiO) and zinc oxide (ZnO) thin films. The crystals of zinc oxide show preferred orientation along the (101) plane while nickel oxide thin film shows preferential growth in (111) plane. Surface morphologies of the films revealed uniform covering of the surface by ZnO initially and subsequent layer of NiO. The device was transparent in the visible part of the spectrum, it has an absorption edge at 370 nm. The current–voltage characteristics of the heterojunction indicated a rectifying property. The ideality factor of the junction was found to be 3.9 and the series resistance was 254 Ω.

8.2 Properties of the p-NiO/n-ZnO heterojunction

The heterojunction between NiO and ZnO was fabricated as explained in section 4.2.6. Circular gold contacts were deposited as discussed in section 4.2.8. The device was characterised and the electrical parameters of the junction were determined.

8.2.1 Structural properties

Figure 8.1 shows the XRD patterns of ZnO/ITO and NiO/ZnO/ITO heterostructure. Three major diffraction peaks of ZnO were found at 31.5°, 34.1°, and 36.0°. These correspond to (100), (002), and (101) diffraction planes respectively. The peaks were indexed to JCPDS file number (36-1451) [1]. Diffraction peaks of ITO were indexed to JCPDS file number (06-0416) [2]. Two diffraction peaks of NiO found at 37.2° and 43.2° correspond to (111) and (200) diffraction planes respectively [3], the peaks were indexed to JCPDS (04-0835). The peaks in the XRD pattern showed that the device was composed of NiO and ZnO. No impurities were detected in the the sample by the XRD.

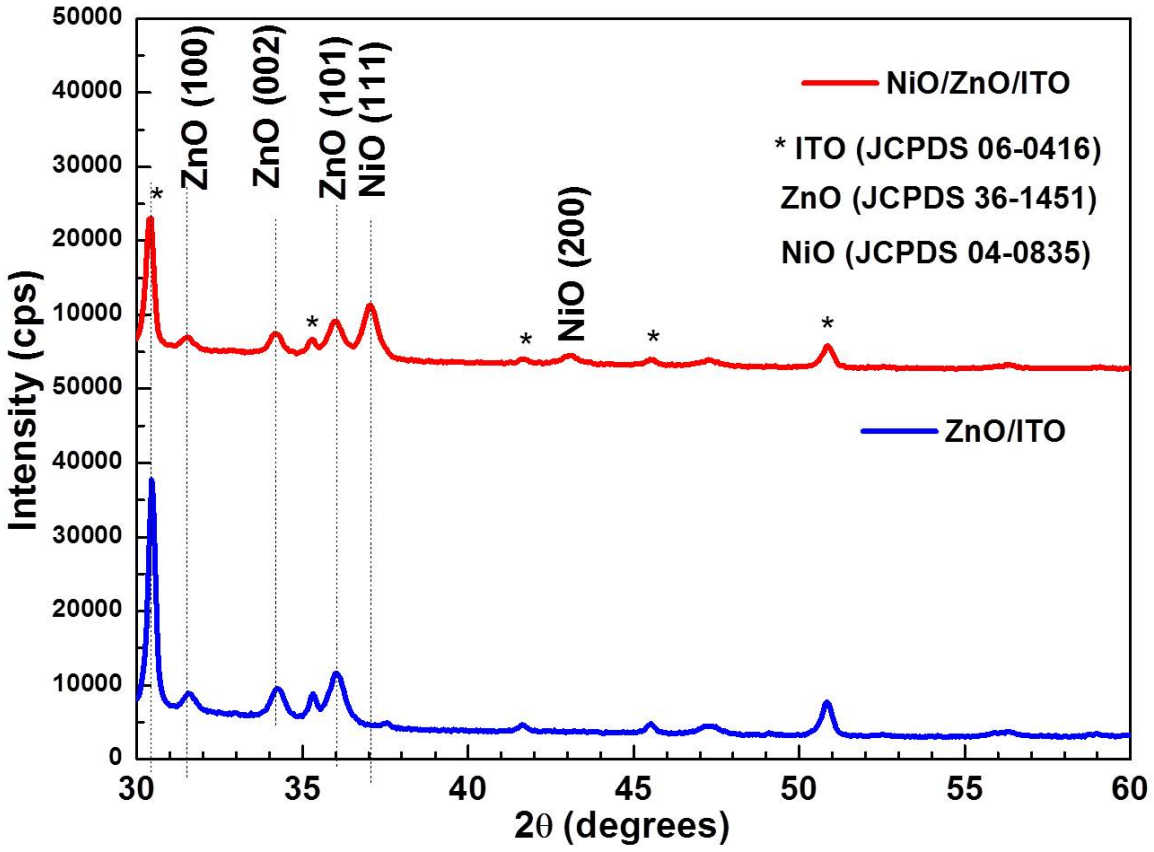

Figure 8.1: XRD pattern of ZnO thin film deposited on ITO glass and NiO/ZnO heterostructure on ITO.

8.2.2 Morphological properties

Figure 8.2(a) is the SEM image of a ZnO thin film on ITO coated glass, showing many elongated ZnO grains lying parallel to the substrate. This might have been the reason for the increased amplitude of the peak due to the (101) plane in the XRD pattern. According to the figure, the surface of the ZnO

film was not smooth. The SEM image of NiO thin film on ZnO is shown in Figure 8.2(b). The figure revealed a smooth surface made of spherical grains. The grains were densely packed and smaller than those of ZnO.

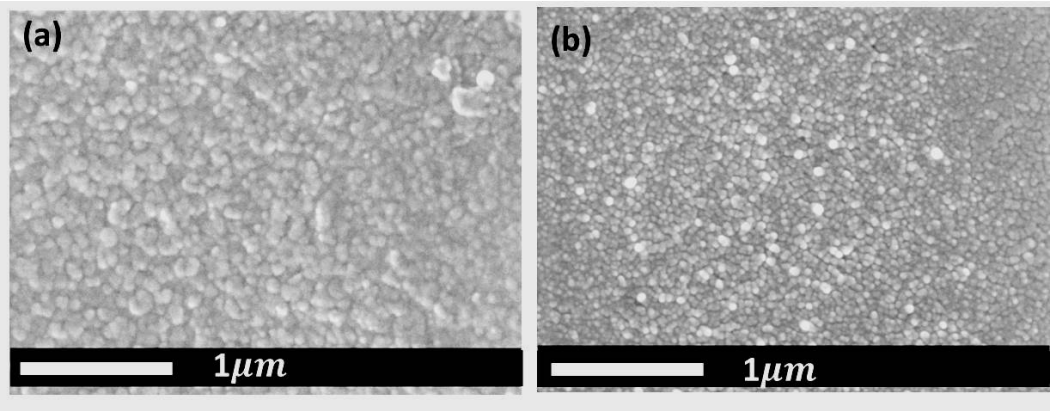

Figure 8.2: SEM images of (a) ZnO thin film on ITO, (b) NiO thin film on ZnO.

8.2.3 Optical properties

The transmittance spectrum of the p-NiO/n-ZnO heterostructure is shown in Figure 8.3. The transmittance at 800 nm was 51.6%, and fell to about 39% at 555 nm. At 400 nm, the transmittance began to fall rapidly from about 23% to zero at 370 nm. This corresponds to an optical bandgap of 3.35 eV, of ZnO. The device was transparent to visible light while the absorption edge of was in the ultraviolet region of the electromagnetic spectrum.

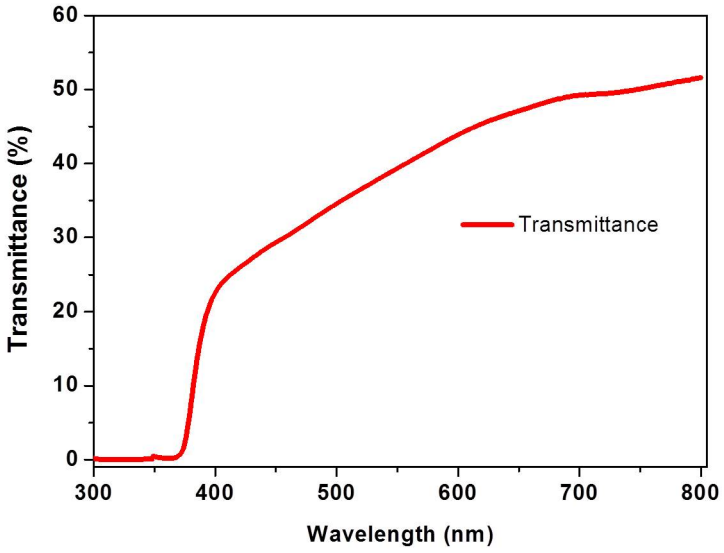

Figure 8.3: The transmittance spectrum of the NiO/ZnO heterostructure.

8.2.4 Electrical properties

Firstly, the I–V characteristics between two Au contacts to the NiO were investigated. The I–V relationship shown in Figure 8.4(a) is linear, therefore it may be concluded that Au forms an ohmic contact to the NiO. The resistance of the NiO layer is 376 Ω as calculated from the slope of graph.

The semilog current–voltage (I–V) characteristics as measured over the heterojunction in the dark (Figure 8.4(b)), shows rectification. Since the Au contacts were ohmic, this rectification is attributed to the heterojunction. The rectification ratio of the junction at 2 V was 260. Ideality factor and series resistance were found by fitting the I–V characteristics. These parameters were also determined using the method proposed by Cheung [4]. The plots of $H(I)$ and $dV/d(\ln I)$ versus I, Figure 8.5(a), were obtained and values of the parameters of the junction were obtained. These values were summarised in Table 8.1.

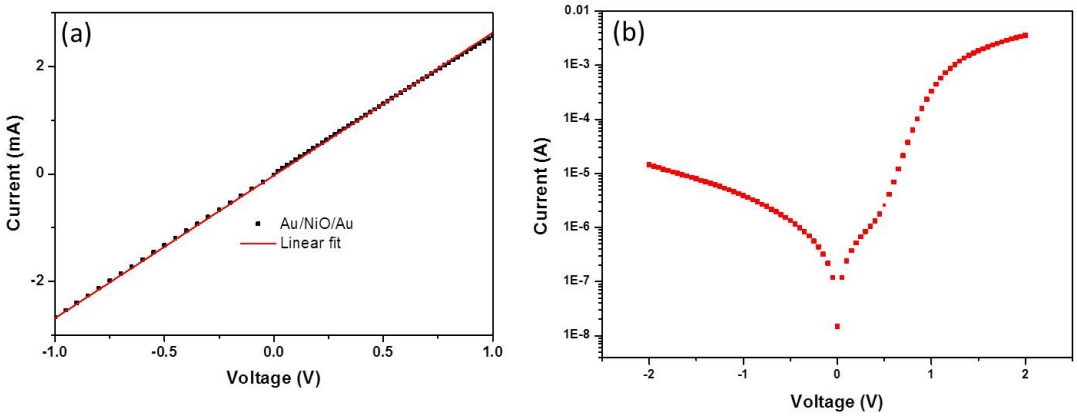

Figure 8.4: (a) I–V relationship between two Au contacts on the NiO film and (b) dark current–voltage characteristics of the heterojunction

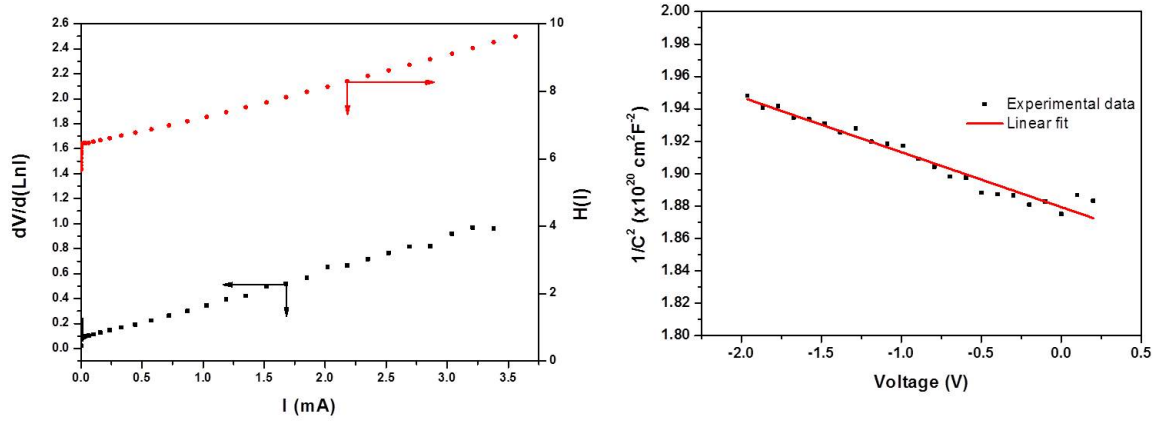

Figure 8.5: (a) Plot of $dV/d(\ln I)$ and $H(I)$ vs I and (b) dark $1/C^2$–V characteristics of the heterojunction.

Table 8.1: Table showing the values of the ideality factor, zero bias barrier height, series resistance and saturation current of the NiO/ZnO heterojunction.

Parameters	$[dV/d(\ln I)]$ vs I	$H(I)$ vs I	$\log I$ vs V
n	4.3		3.9
ϕ (eV)		0.5	0.5
R_s (Ω)	255	260	273
I_s (A)			2.3×10^{-8}

The theoretical band alignment of p-NiO and n-ZnO is shown in Figure 8.6. The barrier heights for both electrons and holes are high, therefore significant conduction in the device under forward and reverse bias was not expected at the voltages at which the investigation was conducted. The transport mechanism across a similar junction, as explained by Ohta *et al.* is due to carrier recombination in the depletion region [5].

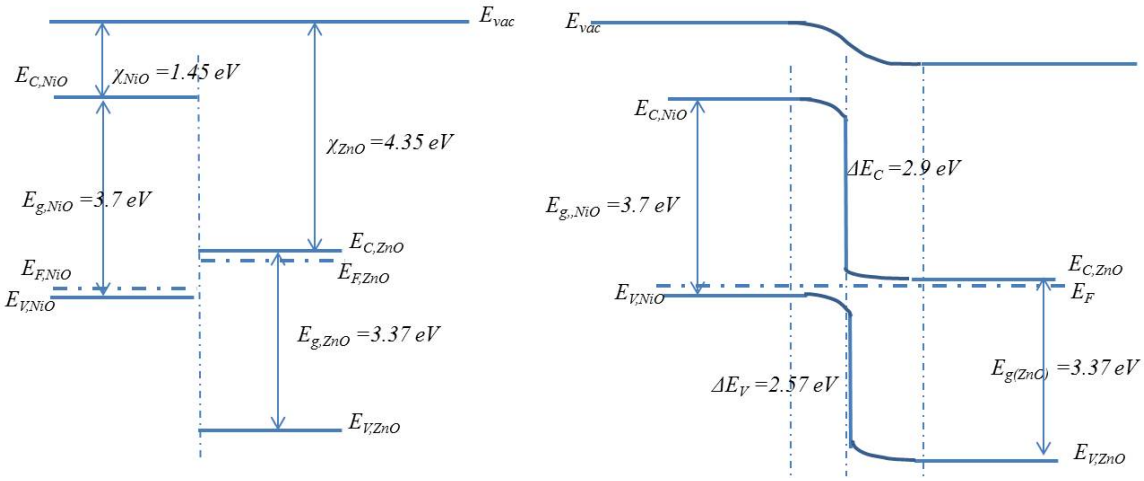

Figure 8.6: Band alignment of p-NiO/n-ZnO (a) before and (b) after the formation of the heterojunction.

It should be kept in mind that the two films were polycrystalline and highly non-uniform. Therefore the band diagram of an ideal heterojunction as shown in Figure 8.6 is not applicable, and many inhomogeneities the barrier are expected. Since I–V measurements very sensitive to regions of lower barrier height, it is believed that these regions of lower barrier height are responsible for the good conduction. The large number of defects in the materials may also play a role. Further indication that the junction is not a simple abrupt junction is obtained from the $1/C^2$–V characteristics of the junction as shown in Figure 8.5(b). Here it can be seen that the capacitance of the junction was much lower than would be expected of an abrupt junction and did not change appreciably with forward bias. Furthermore, the barrier height as calculated from from the intercept with the V-axis was 44 eV, which is unphysically large. However, C–V depth profiling found a net carrier density of approximately 1 $\times$

10^{18}. This is an indication that the depletion region was much wider than expected of an ideal abrupt junction which might be due to interdiffusion of materials around the junction which could result in an intrinsic region between the NiO and ZnO.

8.3 Application of the p-NiO/n-Si heterojunction in light sensing

The XRD pattern of the film deposited on silicon shown in Figure 8.7, confirmed the presence of NiO on the silicon (111) substrate. Diffraction peaks at 32.4 ° and 68.9 ° are from (100) and (400) crystal planes of silicon (JCPDS No. 27-1402) [7]. The other peaks at 37.2 ° and 43.2 ° are from (111) and (200) diffraction planes of NiO respectively.

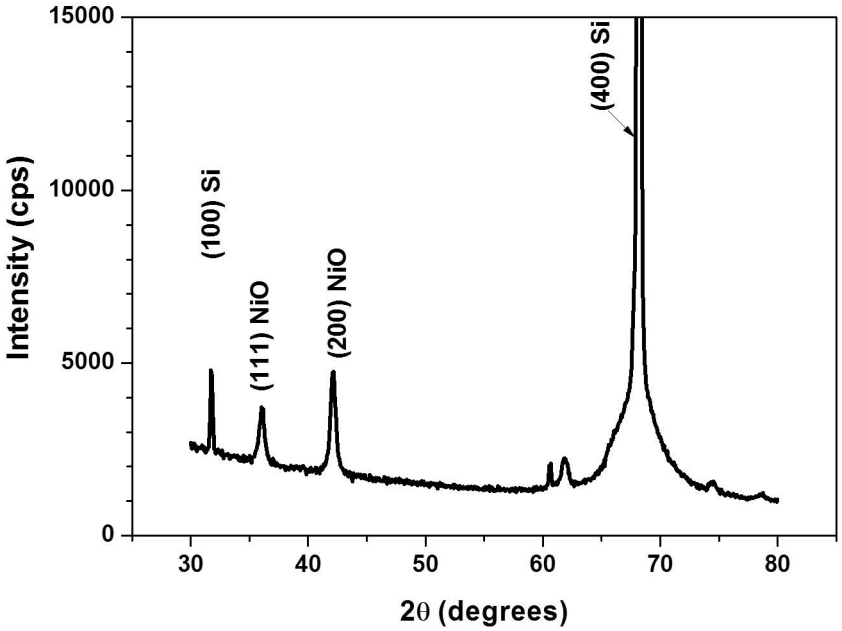

Figure 8.7: XRD pattern of NiO film deposited on silicon substrate.

The current–voltage characteristics of the p-NiO/n-Si, both in the dark and light, is shown in Figure 8.8. The figure shows that rectification took place in the device, the rectification ratio at ±2V was about 70. As previously, the contacts to the NiO were ohmic, therefore rectification occured at the p-NiO/n-Si interface. Under reverse bias, no change due to illumination was observed in the I–V characteristics of the device, but when forward biased, there was a small difference in the forward characteristics.

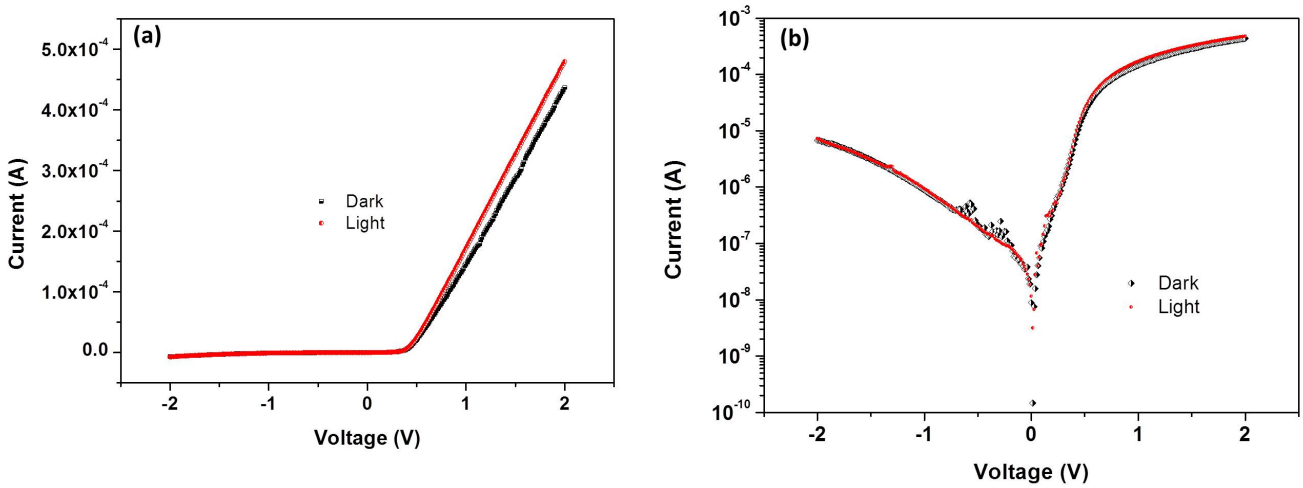

Figure 8.8: Dark and light I–V characteristics of p-NiO/n-Si (a) linear scale and (b) semilog scale.

The band alignment between p-NiO and n-Si before and after the heterojunction is formed is shown in Figure 8.9. The barrier height for electrons is high (around 2.6 eV). Therefore, electrons cannot move, under a forward bias that is less than about 2.6 V, from the conduction band of the n-Si to the p-NiO. However, the barrier height for holes is small. Under forward bias, holes migrate from the valence band of NiO into the n-Si where they recombine with electrons. The hole current constitutes the forward current across the junction under forward bias.

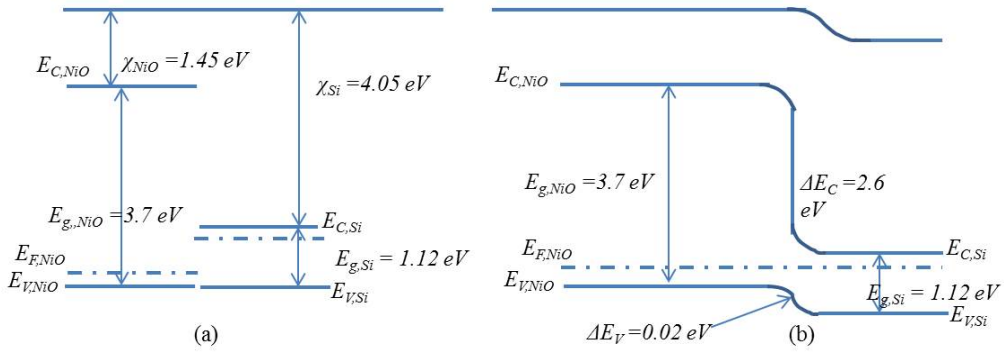

Figure 8.9: Band alignment of p-NiO/n-Si (a) before and (b) after the formation of a heterojunction.

The observed increase in the forward current due to the illumination in the device was in the series resistance region of the semilog I–V characteristics, while there was no change in the reverse or exponential region of the forward conduction, Figure 8.8(b). This suggests that it is due to an increase in the conductivity of one of the semiconductors involved. It was suggested that this could be attributed to the n-Si that, although doped to $10^{16}/\text{cm}^3$, may show an increase in its conductivity due to additional photogenerated carriers.

Summary and conclusions

Thin films of n-ZnO and p-NiO were deposited sequentially on ITO to form a p-n junction. Structural studies confirmed the presence of NiO and ZnO as the only phases in the device. The device was transparent to visible radiation, with an absorption edge at 370 nm. The surface morphologies of the films revealed that ZnO was made up of bigger, elongated grains compared to NiO. The junction between p-NiO and n-ZnO showed rectification up to 2 orders of magnitude at ±2 V. The ideality factor of the device was 4.0 as obtained from the I–V characteristics at low voltage and the series resistance was 254 Ω. C–V measurements found a carrier density of around 10^{18} /cm^3 and indicated that there existed a transition region of about 300 nm between the two semiconductors. A thin film of p-NiO was deposited on an n-type silicon wafer using spray pyrolysis. The XRD pattern of the film confirmed the presence of NiO on silicon. Gold and gold-antimony alloy were used as contacts to NiO and silicon respectively. The I–V characteristics of the device both in the dark and light showed that rectification occurred in the device and that it was slightly sensitive to the light from the solar simulator. Future work will be targeted at the investigation of the electrical properties of the p-NiO/n-Si and p-NiO/n-ZnO heterojunctions under illumination at different wavelengths of ultraviolet radiation.

References

[1] U Srinivasa Rao, G Srinivas, and T Prasada Rao. Influence of precursors on morphology and spectroscopic properties of ZnO Nanoparticles. *Procedia Materials Science*, 10:90–96, 2015.

[2] Davood Raoufi and Taha Raoufi. The effect of heat treatment on the physical properties of sol–gel derived ZnO thin films. *Applied Surface Science*, 255(11):5812–5817, 2009.

[3] Genqiang Zhang, Le Yu, Harry E Hoster, and Xiong Wen David Lou. Synthesis of one-dimensional hierarchical NiO hollow nanostructures with enhanced supercapacitive performance. *Nanoscale*, 5(3):877–881, 2013.

[4] SK Cheung and NW Cheung. Extraction of Schottky diode parameters from forward current-voltage characteristics. *Applied Physics Letters*, 49(2):85–87, 1986.

[5] Hiromichi Ohta, Masao Kamiya, Toshio Kamiya, Masahiro Hirano, and Hideo Hosono. UV-detector based on pn-heterojunction diode composed of transparent oxide semiconductors, p-NiO/n-ZnO. *Thin Solid Films*, 445(2):317–321, 2003.

[6] Cheng-Xin Wang, Guo-Wei Yang, Hong-Wu Liu, Yong-Hao Han, Ji-Feng Luo, Chun-Xiao Gao, and Guang-Tian Zou. Experimental analysis and theoretical model for anomalously high ideality factors in ZnO/diamond pn junction diode. *Applied Physics Letters*, 84(13):2427–2429, 2004.

[7] Bhaskar Parida, Seongjun Kim, Munsik Oh, Seonghoon Jung, Minkyung Baek, Jae-Hyun Ryou, and Hyunsoo Kim. Nanostructured-NiO/Si heterojunction photodetector. *Materials Science in Semiconductor Processing*, 71:29–34, 2017.

Chapter 9

Conclusions and recommendation

9.1 Introduction

In this study, NiO thin films were synthesised using chemical solution methods. The films were characterized to determine their structural, microstructural, optical and electrical properties. The discussion of results of the films produced using each method are given in Chapter 5 to Chapter 7. Chapter 8 highlights the properties of the heterojunction p-n device that was made from NiO thin film and other materials. In this chapter, the major highlights of the study and recommendations for future work are presented.

9.1.1 Conclusions

Using the CBD method, films that were deposited with ammonia as the complexing agent did not adhere to glass substrates due to the rate of dissociation of the Ni^{2+}-ammonia complex. Monoethanolamine was found to be a more stable complexing agent and it provided the required alkaline medium for deposition of NiO thin films. The complex formed with Ni^{2+} ions does not dissociate rapidly, thus providing more adherent films. The as-deposited film in CBD was a hydrated nickel hydroxide which was transformed to nickel oxide during annealing at temperatures above 350 ℃. The annealed films were polycrystalline with an average lattice constant of 0.4169 nm. The films were porous, having honeycomb-like structure. The optical band gap was 3.8 eV. The properties of the films revealed that they were not suitable for transparent conducting oxides applications but might

be useful in biochemical and gas sensing applications due to the large surface area.

Properties of the films produced using spin-coating depended on the conditions of fabrication. The films that were produced from four layers of 0.1 M and 0.2 M precursor solutions and annealed at 400 ℃, were amorphous. Polycrystalline films were obtained at a precursor concentration of 0.7 M, with an average lattice constant of 0.4180 nm. Drying at a temperature of 200 ℃ and above, and annealing at 400 ℃ and above were found to be suitable for producing crystalline films. The crystallinity of the films increased with temperature of drying and annealing. The films were granular and the grain size increased as the annealing temperature was increased. The optical band gaps of the films increased with drying temperature and decreased with annealing temperature. There was a reduction in the resistivity of the films as the annealing temperature increased from 400 °C to 500 °C. The resistivity increased when higher annealing temperatures were used. The Al/p-NiO Schottky diode on silicon had a rectification ratio of 3×10^2 at 2.0 V, saturation current of 1.28×10^{-8} A, ideality factor of 3.8, series resistance of 1.454 kΩ, and Schottky barrier height of 0.7 eV.

The spray pyrolysis was carried out with a custom-built system, deposition of the films was done at a temperature between 275 °C and 300 °C. The films were annealed at 500 °C to complete the transformation of the precursor to NiO. The most prominent XRD peak in the NiO thin films deposited through spray pyrolysis was along the (111) crystallographic plane. The crystallinity increased with the number of spraying cycles and the concentration of the precursor. The films were granular and the grain size increased as the concentration of the precursor was increased. The shape and size of the grains of the films were affected by the motion of the nozzle. The films had uniform growth on the substrates and without cracks. The spray pyrolysis method proved to be the best for producing NiO thin films for light sensing. The optical and electrical properties the films were better when compared with films that were produced from spin coating. The films were granular and more compact than CBD films, consequently, electrical contacts could be deposited on them easily.

The heterojunction between NiO and ZnO thin films was transparent to visible light, the absorption edge of the junction was in the ultraviolet region of the electromagnetic spectrum at 370 nm. The junction between p-NiO and n-ZnO showed rectification up to 2 orders of magnitude at ±2 V. The ideality factor of the device was 4 as obtained from the I–V characteristics measured in the dark, and the series resistance of the junction was 254 Ω. Similarly, the heterojunction made from p-NiO and n-Si demonstrated rectification with a rectification ratio of about 70 at ±2 V. The I–V characteristics of the device both in the dark and light showed that rectification occurred at the heterojunction and

showed a small response to light from the solar simulator. The fact that NiO can be fabricated from a chemical solution method and that a p-n junction can be fabricated using the method is an indication that the material can be used in printed electronics.

9.1.2 Recommendations for future work

The following are recommended for future work:

• Investigation of the effects of concentration of precursor solution on the microstructural and electrical properties of NiO thin films produced by CBD and application of the films in gas sensing.

• Application of Al/p-NiO Schottky diode in hydrogen gas sensing.

• Development of a spray pyrolysis system for efficient synthesis of thin films.

• Synthesis of noble metal-doped NiO thin films using spray pyrolysis for electronics and gas sensing applications.

• Synthesis and application of NiO thin films and nanoparticles for biomedical applications and ultraviolet light sensing.